Specific depletion of the motor protein KIF5B leads to deficits in dendritic transport, synaptic plasticity and memory

Junjun Zhao[1#], Albert Hiu Ka Fok[1#], Ruolin Fan[1], Pui-Yi Kwan[1], Hei-Lok Chan[1], Louisa Hoi-Ying Lo[1], Ying-Shing Chan[1, 2], Wing-Ho Yung[3], Jiandong Huang[1, 2, 4], Cora Sau Wan Lai[1, 2, 5] and Kwok-On Lai[1, 2, 5]

[1]School of Biomedical Sciences,
[2]State Key Laboratory of Brain and Cognitive Sciences,
The University of Hong Kong
[3]School of Biomedical Sciences, Chinese University of Hong Kong
[4]Institute of Synthetic Biology, Shenzhen Institutes of Advanced Technology,
Chinese Academy of Sciences, Shenzhen 518055, P.R. China

[#]Equal contribution to the study
[5]To whom correspondence should be addressed:
Dr. Cora Sau Wan Lai and Dr. Kwok-On Lai

School of Biomedical Sciences, Faculty of Medicine, the University of Hong Kong
21 Sassoon Road, Pokfulam, Hong Kong, China.
Phone: 852-3917-9521
Fax: 852-2855-9730
E-mail: coraswl@hku.hk, laiko@hku.hk

Running title: KIF5B regulates dendritic spine morphogenesis and memory formation

Keywords: Dendritic spine; synapse; intracellular transport; post-translational modification; learning and memory

ABSTRACT

The kinesin I family of motor proteins are crucial for axonal transport, but their roles in dendritic transport and postsynaptic function are not well-defined. Gene duplication and subsequent diversification give rise to three homologous kinesin I proteins (KIF5A, KIF5B and KIF5C) in vertebrates, but it is not clear whether and how they exhibit functional specificity. Here we show that knockdown of KIF5A or KIF5B differentially affects excitatory synapses and dendritic transport in hippocampal neurons. The functional specificities of the two kinesins are determined by their diverse carboxyl-termini, where arginine methylation occurs in KIF5B and regulates its function. KIF5B conditional knockout mice exhibit deficits in dendritic spine morphogenesis, synaptic plasticity and memory formation. Our findings provide insights into how expansion of the kinesin I family during evolution leads to diversification and specialization of motor proteins in regulating postsynaptic function.

INTRODUCTION

Synapse maturation and remodeling are crucial for brain functions including learning and memory. The postsynaptic sites of excitatory synapses are located on the dendritic spines, which undergo dynamic structural changes that are essential for experience-driven wiring of the neuronal network (Trachtenberg et al., 2002). More than 1,000 proteins with diverse structures and functions have been identified in the postsynaptic density (Bayes et al., 2011), and a tight regulation of their abundance and localization is essential for proper synapse development and plasticity. Many of the postsynaptic proteins are locally translated in dendrites, which allows spatial and temporal regulation of molecular composition of individual synapses in response to local extracellular stimuli (Holt and Schuman, 2013). To achieve protein synthesis in dendrites, mRNAs synthesized in the soma need to be assembled in ribonucleoproteins (RNPs) and transported over long distances by molecular motors along microtubule (Doyle and Kiebler, 2011).

Kinesin and dynein superfamilies of proteins are microtubule-dependent molecular motors that mediate long-distance transport of materials in neuron. The kinesin superfamily is very diverse and contains 45 members in mammal. It is sub-divided into 14 different families based on structural similarity (Hirokawa et al.,

2010). The kinesin I family (encoded by the *Kif5* genes) contains the founding kinesin protein KHC (Brady, 1985; Vale et al., 1985). While only one single KIF5 is present in invertebrates such as *Drosophila*, *C. elegans* and *Aplysia*, gene duplication events give rise to three homologous KIF5 genes (*Kif5a*, *Kif5b* and *Kif5c*) in vertebrates (Miki et al., 2001). Unlike KIF5B which is ubiquitously expressed, KIF5A and KIF5C are mostly expressed in neuron (Kanai et al., 2000). Functional redundancy has been demonstrated among the three KIF5s, as exogenous expression of KIF5A or KIF5C can rescue the impaired mitochondrial transport in cells lacking KIF5B (Kanai et al., 2000). In contrast, specific function of individual KIF5 has been reported in zebrafish, in which axonal transport of mitochondria depends only on KIF5A but not the other two KIF5s (Campbell et al., 2014). Furthermore, only KIF5A dysfunction leads to seizure and the neuromuscular disorder Hereditary Spastic Paraplegia (Fink, 2013; Nakajima et al., 2012). It is therefore plausible that the expansion of the *Kif5* gene family during evolution enables functional specificity of individual KIF5 in the vertebrate brain, although the molecular basis of the specificity has not been identified. The three KIF5s contain motor, stalk, and tail domains (Friedman and Vale, 1999), and they all bind to kinesin light chain (KLC) which mediates interaction with some of the cargoes (Kamal et al., 2000; Morfini et al., 2016). Despite the overall structural similarity, the carboxyl-termini (starting from around amino acid 934 until the last

amino acid) of the three KIF5s are very different, which may confer the individual KIF5 distinctive functions in neurons.

Previous studies have mostly focused on KIF5 function in axonal transport because the motor domain of KIF5 preferentially moves out of dendrites into axons, and KIF5 function is negatively regulated by the dendritic protein MAP2 (Gumy et al., 2017; Huang and Banker, 2012; Kapitein et al., 2010; Tas et al., 2017). However, all three KIF5s are co-purified with RNPs, and dominant-negative KIF5 disrupts the dendritic localization of RNA-binding proteins (Kanai et al., 2004). Additional dendritic cargoes for KIF5, including the AMPA receptor/GRIP1 complex and $GABA_A$ receptor, have also been identified (Heisler et al., 2014; Nakajima et al., 2012; Setou et al., 2002; Twelvetrees et al., 2010). KIF5s therefore likely participate in both axonal and dendritic transport. Despite previous studies on its importance on AMPA receptor trafficking (Kim and Lisman 2001; Setou et al., 2002; Hoerndli et al., 2013; Heisler et al. 2014), the role of KIF5 on dendritic spine morphogenesis and synaptic plasticity has not been comprehensively examined. In this study, we aim to investigate whether the three KIF5s have specific roles in the development and function of excitatory synapses on the postsynaptic neuron, and what might underlie the functional specificity.

Here we report that KIF5B but not KIF5A is specifically involved in the development of excitatory synapses of postsynaptic neurons and dendritic transport of the RNA-binding protein fragile X mental retardation protein (FMRP). The diverse carboxyl-termini of KIF5A and KIF5B determine their functional specificity, and we further identified arginine methylation of KIF5B as a novel post-translational modification (PTM) in regulating cargo binding. Because of the embryonic lethality of KIF5B knockout mice that precludes their use to study the synaptic and cognitive functions of adult brain *in vivo*, we generate mice with KIF5B conditional knockout in CaMKIIα-expressing neurons. The KIF5B conditional knockout mice exhibit altered dendritic spine structural plasticity *in vivo*, as well as deficits in synaptic plasticity and memory formation. Our study strongly suggests that homologous motor proteins of the kinesin I family have non-redundant functions in regulating the development and function of excitatory synapses that is crucial for learning and memory.

RESULTS

Expression and subcellular localization of KIF5s in hippocampus

To compare the synaptic functions of different KIF5s, we mainly focus on

86 neurons from the hippocampus, a brain region that is important for learning and
87 memory and where the development of excitatory synapses is well-studied. We first
88 determined the expression of different KIF5s in the hippocampus along development.
89 Although KIF5C was previous reported to be expressed exclusively in medulla and
90 spinal cord (Kanai et al., 2000), *Kif5c* mRNA is detected in the developing
91 hippocampus in Allen Brain Atlas. Expression data for *Kif5a* and *Kif5b* transcripts in
92 the developing brain is not available, but transcripts encoding the three KIF5s are
93 detected in the adult mouse hippocampus in the atlas. Previous study has reported that
94 *Kif5* mRNAs expression is unchanged in cultured hippocampal neurons along
95 maturation *in vitro* (Silverman et al., 2010). On the other hand, we found that all three
96 KIF5 proteins showed similar developmental expression profiles in the hippocampus,
97 with the expression more prominent at early postnatal stages and significantly reduced
98 at later postnatal and adult stages (Figure 1A). Next, we examined the distribution of
99 KIF5 protein in the brain by fractionation. All three KIF5s were detected in the
100 synaptic plasma membrane fraction (Figure 1B), which is consistent with the
101 proteomic study reporting the presence of three KIF5s in the postsynaptic density
102 (Bayes et al. 2012).

KIF5A and KIF5B have distinct functions in excitatory synapse development and function

Many functional studies on KIF5s employ over-expression of dominant-negative constructs, which contain cargo-binding domains of the kinesin but lacking motor domains, thereby disrupting cargo movement through competitive binding. Here we attempt to address the role of individual KIF5 by specifically depleting each KIF5 homolog in neurons using RNA-interference. Three short hairpin RNAs (shRNAs) were created that specifically targeted KIF5A, KIF5B, and KIF5C. The knockdown efficiency and specificity of each shRNA in neuron were confirmed by Western blot and immunofluorescence staining (Figure 1-figure supplement 1). To examine the effect on excitatory synaptic transmission, whole-cell patch recording was performed in hippocampal neurons transfected with shRNAs targeting different KIF5s together with GFP construct. We found that knockdown of individual KIF5 differentially affected excitatory synaptic transmission. Compared to control shRNA, knockdown of KIF5B resulted in the most profound and significant reduction in the frequency of miniature excitatory synaptic current (mEPSC), while knockdown of KIF5C did not affect mEPSC frequency or amplitude. Notably, introduction of KIF5A-shRNA did not change the mEPSC frequency but instead significantly increased the mEPSC

121 amplitude (Figure 1C).

122 Since the shRNA and GFP constructs were introduced to the neurons using
123 calcium phosphate precipitation which has very low transfection efficiency, the
124 reduction of mEPSC frequency in the GFP-positive neuron was likely due to
125 cell-autonomous decrease in synapse number on the postsynaptic neuron instead of
126 change in presynaptic release. To test this hypothesis, the density of different types of
127 dendritic spines was examined. Although knockdown of either KIF5B or KIF5C
128 caused a significant reduction in the density of mushroom spines, only the
129 introduction of KIF5B-shRNA increased the density of filopodia. On the other hand,
130 knockdown of KIF5A did not cause any change in the density of mushroom spines or
131 filopodia when compared to control neurons (Figure 1D). The differential effect of
132 KIF5A and KIF5B knockdown on spine morphogenesis and synaptic transmission is
133 not attributed to differences in knockdown efficiency, as either shRNA reduced the
134 target KIF5 expression by similar levels (Figure 1-figure supplement 1). Taken
135 together, knockdown of KIF5B in hippocampal neurons leads to more profound
136 change in mEPSC and dendritic spine morphogenesis than knockdown of KIF5C,
137 while knockdown of KIF5A has no effect on dendritic spines.

138 To confirm that KIF5A and KIF5B indeed differentially regulate dendritic spine

morphogenesis and to exclude potential off-target effect of the KIF5B-shRNA, rescue experiments using different KIF5s were performed. We focus on mushroom spines instead of the other three spine types in subsequent experiments because mushroom spines are regarded as mature spines that are more stable and possess the excitatory postsynaptic density (Bourne and Harris, 2007; Berry and Nedivi, 2017). Moreover, among the different spine types only mushroom spines were reduced after KIF5B knockdown, and the fewer mushroom spines correlated well with the decrease in mEPSC frequency. As expected, co-expression of KIF5B reversed the loss of mushroom spines induced by the KIF5B-shRNA. However, co-expression of KIF5A with the KIF5B-shRNA failed to rescue the loss of mushroom spines (Figure 2A). In contrast, co-expression of KIF5C fully reversed the mushroom spine defects induced by the KIF5B-shRNA (Figure 2B), suggesting that KIF5B and KIF5C share similar function on excitatory synapse development. Both endogenous and exogenously expressed KIF5A and KIF5B were present in dendrites and dendritic spines, and the percentage of dendritic spines containing endogenous KIF5A was even higher than that of KIF5B (Figure 2-figure supplement 1). These findings indicate that KIF5A and KIF5B have intrinsically distinct functions on excitatory synapses, although both KIF5A and KIF5B can be found in dendritic spines.

157 *Differential functions of KIF5A and KIF5B in dendritic transport of FMRP*

158 KIF5 protein structure is divided into three domains: a motor domain, two
159 coiled-coil domains which together form the stalk, and the tail domain (Friedman and
160 Vale, 1999). Since the carboxyl termini, the most diverse regions between the KIF5s,
161 represent part of the cargo-binding tail domain (Morfini et al., 2016; Nakajima et al.,
162 2012) (Figure 3A), we next ask whether the three KIF5s might bind to cargoes
163 differentially. We examine several different dendritic cargoes including the
164 RNA-binding proteins (RBPs) FMRP and Ras GTPase-activating protein-binding
165 protein (G3BP1 and G3BP2), which have been shown to regulate dendritic spine
166 maturation (Dictenberg et al., 2008), as well as the AMPA receptor subunit GluA2.
167 Pull-down assay using carboxyl-terminal fragments of individual KIF5s revealed that
168 FMRP was preferentially pulled down by KIF5B and KIF5C but not KIF5A, while all
169 three KIF5s could pull down G3BPs and GluA2 (Figure 3B).

170 Next, we examined whether knockdown of KIF5A and KIF5B differentially
171 affects the dendritic localization and transport of FMRP. Neurons were co-transfected
172 with GFP-FMRP and tdTomato, which labels the dendritic arbors and spines, together
173 with the control shRNA, KIF5A-shRNA, or KIF5B-shRNA, followed by spinning
174 disk confocal live imaging. Consistent with previous study on the trafficking of RBPs

(Mitsumori et al., 2017), most FMRP granules were either stationary or exhibiting oscillatory movement, while a small proportion showing unidirectional or bidirectional movement. Compared to control shRNA, knockdown of KIF5B significantly reduced the density of FMRP granules on dendrites. Interestingly, KIF5B shRNA only significantly decreased the density of stationary but not motile granules. In contrast, knockdown of KIF5A caused a general increase in the density of motile granules while decreasing the stationary granules, resulting in no net change in the density of total granules (Figure 3C-D). There was no effect on the motility of the unidirectional and bidirectional granules after knocking down either KIF5A or KIF5B (Figure 3 figure supplement 1). To further characterize the effect on FMRP function in dendrite, the localization of two FMRP-cargoes, CaMKIIα and Grin2b mRNAs, was examined using fluorescent *in situ* hybridization (FISH) upon knockdown of KIF5A or KIF5B, and the distribution of mRNA puncta along individual dendrites was analyzed. Consistent with the reduced density of GFP-FMRP granules, knockdown of KIF5B also significantly reduced the density of both CaMKIIα and Grin2b mRNA puncta on dendrites (Fig. 3E). In contrast, knockdown of KIF5A did not affect CaMKIIα and Grin2b mRNA density on dendrite. Together these findings indicate that KIF5A and KIF5B differentially regulate the dendritic transport of FMRP and its mRNA cargoes.

Carboxyl termini of KIF5A and KIF5B determine their functional specificity in neuron

What is the molecular basis of the functional specialization of KIF5A and KIF5B? The presence of a longer carboxyl-terminus in KIF5A which is very diverse from the corresponding regions of KIF5B and KIF5C (Figure 3A) prompt us to explore if it represents an inhibitory constraint for cargo binding. Towards this end, we created a truncated KIF5A construct with the carboxyl-terminal lacking the last 88 amino acids, as well as a chimeric KIF5A in which the last 88 amino acids were substituted by the shorter carboxyl-terminus of KIF5B. Either one of these constructs but not the wild-type KIF5A was able to pull down FMRP from the synaptoneurosome, suggesting that the carboxyl-terminus of KIF5A indeed inhibits binding of specific cargoes (Figure 4A). Remarkably, when shRNA targeting KIF5B was introduced into hippocampal neurons to induce loss of mushroom spines, co-expression of the chimeric KIF5A that contained the carboxyl-terminus of KIF5B was able to reverse the spine phenotype (Figure 4B). These findings indicate that the last 88 amino acids of KIF5A prevent the motor protein to promote dendritic spine maturation, while its substitution by the shorter carboxyl terminus of KIF5B is sufficient to regain its

synaptic function.

Arginine methylation near the carboxyl- terminus of KIF5B is required for its synaptic function

Amino acid sequence alignment of the carboxyl termini of different KIF5s revealed the presence of two arginine residues (Arg-941 and Arg-956) followed by glycine residues (the RGG motif) in KIF5B that are conserved across different vertebrates. KIF5C contains only the Arg-941 but not Arg-956, while these two RGG motifs are absent in the KIF5A carboxyl-terminus (Figure 5A). The RGG motifs often undergo arginine methylation, which involves the addition of methyl group to the guanidine nitrogen atom of arginine and is catalyzed by the protein arginine methyltransferases (PRMT) (Najbauer et al., 1993). Hundreds of arginine-methylated proteins in the adult mouse brain have recently been identified by mass spectrometry (Guo et al., 2014), and our data mining results indicated that KIF5B was one of the methylated proteins. Although arginine methylation is a well-established mechanism in the regulation of gene transcription and splicing in the nucleus (Bedford and Clarke, 2009), emerging studies have indicated their function outside the nucleus, in particular their importance in synaptic functions (Penney et al., 2017). We therefore

investigate whether arginine methylation represents a novel post-translational mechanism in regulating kinesin functions. We first confirmed the arginine methylation of KIF5B and KIF5C but not KIF5A when heterogeneously expressed in 293T cells (Figure 5B). Using reciprocal immunoprecipitation with antibodies that recognize the mono-arginine methylation within glycine-rich region or KIF5B, we confirmed that KIF5B was methylated in the synaptoneurosome (Figure 5C). To determine whether the two conserved RGG sequences within the carboxyl-terminus of KIF5B are indeed the major methylation sites, we substituted the two arginine residues to histidine by site-directed mutagenesis, which retained the positive charges of the residues but could not undergo PRMT-mediated methylation. The KIF5B R941H or R956H mutant showed reduced methylation, whereas arginine methylation was absent in the double mutant (R941/956H) in which both arginine residues were substituted by histidine (Figure 5D). These results indicate that R-941 and R-956 are the two major methylation sites of KIF5B.

To ask whether and how arginine methylation affects KIF5B function, pull-down experiments were performed using the wild-type or methylation-deficient mutant (R941/956H) of KIF5B. The amount of FMRP and G3BP1 pulled down by the methylation-deficient mutant was significantly reduced when compared to wild-type

KIF5B (Figure 5E). To address whether arginine methylation is required for the synaptic function of KIF5B, we first compared the activity of wild-type and methylation-deficient mutant in the formation of mushroom spines using the KIF5B-shRNA rescue experiments. Co-expression of wild-type KIF5B reversed the loss of mushroom spines induced by the knockdown of KIF5B, while the methylation-deficient KIF5B failed to rescue the mushroom spine loss (Figure 5F). Moreover, co-expression of wild-type but not the methylation-deficient KIF5B with the KIF5B-shRNA significantly increased the mEPSC frequency, (Figure 5G). These results are consistent with the hypothesis that arginine methylation at the carboxyl-terminus is essential for KIF5B function on dendritic spine development and synaptic transmission, and suggesting a mechanism through regulating cargo-binding.

Generation of KIF5B conditional knockout mice

Since KIF5B homozygous knockout is embryonic lethal (Tanaka et al., 1998), we generated a KIF5B conditional knockout (*Kif5b*$^{-/-}$) mice using the Cre/loxP gene-targeting strategy to study the function of KIF5B *in vivo*. CaMKIIα promoter-driven Cre transgenic line (*CaMKIIα-Cre*) (Tsien et al., 1996) and *Kif5b*$^{fl/fl}$ mice (Cui et al., 2011) were used to generate heterozygous (*CaMKIIα-Cre;Kif5b*$^{fl/+}$,

Hetero) and homozygous (*CaMKIIα-Cre;Kif5b*$^{fl/fl}$, Homo) conditional knockout mice in CaMKIIα-expressing neurons, which started the expression of Cre-recombinase after birth (Dragatsis and Zeitlin, 2000; Tsien et al., 1996) (Figure 6A). Both homozygous and heterozygous mice were viable, and the homozygous mice did not differ in the general appearance or brain size from the wild-type (Figure 6-figure supplement 1). Analysis of whole-brain lysate showed a significant reduction of KIF5B protein level in homozygous knockout mice when compared to wild-type, and importantly there were no significant changes in the expression of KIF5A and KIF5C (Figure 6B), or the dendritic kinesin KIF17 which is crucial for synaptic plasticity and memory formation (Song et al., 2009; Yin et al., 2011; Franker et al., 2016) (Figure 6-figure supplement 2). We also examined the levels of KIF5B expression by immunohistochemistry in excitatory neurons using neurogranin (NRGN) as a marker in the neocortex. We found that homozygous mice showed a significant reduction of cells that were positive for both KIF5B and NRGN in the frontal association cortex (FrA) when compared to wild-type mice, without significant change in the number of neurons in this region (Figure 6C, Figure 6-figure supplement 1).

KIF5B regulates dendritic spine density and plasticity in vivo

To determine the effect of KIF5B knockout on dendritic spines in adult neurons, the conditional knockout mice were crossbred with *Thy1*-YFP H line mice to enable sparse neuronal labeling for isolated dendrite imaging, followed by three-dimensional reconstruction for the analysis of spine number (Figure 7A). Conditional knockout of KIF5B at postnatal stages resulted in a significant reduction of dendritic spines in CA1 hippocampal neurons of homozygous mice (Figure 7B). However, the effect of KIF5B on spine density is region-specific, since the dendritic spine number was not significantly different between control and knockout mice in neurons of the FrA (Figure 7C). To examine the excitatory synaptic transmission of CA1 hippocampal neurons, whole-cell patch recording was conducted on hippocampal slices from the wild-type and KIF5B conditional knockout mice. CA1 hippocampal neurons of the KIF5B conditional knockout mice showed a significant reduction in both the frequency and amplitude of mEPSC as compared with wild-type neurons (Figure 7D). Therefore, the KIF5B conditional knockout mice showed a reduction of dendritic spine density that is associated with deficient excitatory synaptic transmission in hippocampal neurons.

Although there was no significant difference in terms of dendritic spine density in FrA in homozygous conditional knockout, this region was chosen to examine

dendritic spine plasticity based on its involvement in associative learning and accessibility for *in vivo* transcranial imaging (Lai et al., 2012; Nakayama et al., 2015). Using two-photon microscopy, we monitored the baseline dendritic spine plasticity of adolescent mice (P31 ±1) over 7 days. Imaging sessions were performed on Day 0, 2, and 7 (Figure 7E-F). We found that both heterozygous and homozygous mice showed a significant increase in dendritic spine elimination compared to wild-type mice over 2 days (Figure 7G). However, when we examined the spine plasticity in the next time window from Day 2- Day 7 over 5 days, both heterozygous and homozygous mice showed an increase in dendritic spine formation (Figure 7H). Overall, both heterozygous and homozygous KIF5B conditional knockout mice showed an increase of dendritic spine turnover rate when compared to wild-type, but only that in homozygous was statistically significant (Figure 7I). Although we did not observe significant difference in the survival rate of newly formed spines (Figure 7-figure supplement 1), we found that the increase in spine formation during the second time window was caused by the significant increase in re-formation of spines in close proximity to eliminated spines from first time window (Figure 7J). These data suggest that KIF5B knockout in excitatory pyramidal neurons alters normal dendritic spine plasticity with an increase of synaptic instability in the neural circuitry.

316

317 *KIF5B conditional knockout mice exhibited deficits in synaptic plasticity, learning*
318 *and memory*

319 Based on the role of KIF5B on dendritic spine density and plasticity, we next
320 investigated the impact of KIF5B conditional knockout on animal behavior. A series
321 of behavioral tests were performed, including open field test, elevated plus maze,
322 marble burying test, 3-chamber social interaction test, novel object recognition test,
323 auditory-cued fear conditioning, and Barnes maze. We found that there was no
324 significant difference in open field test, elevated plus maze, and marble burying test in
325 heterozygous and homozygous mice when compared to wild-type, indicating that
326 conditional knockout of KIF5B did not lead to hyperactivity, anxiety-like or repetitive
327 behaviors (Figure 8-figure supplement 1). On the other hand, homozygous mice
328 exhibited memory deficits in a variety of learning-related behaviors. In 3-chamber
329 social interaction test, homozygous mice showed a significant reduction of social
330 memory index (Figure 8A), but no significant difference in total interaction time from
331 wild-type (Figure 8-figure supplement 2A-B). These data showed that KIF5B
332 homozygous conditional knockout leads to deficits in social memory. In novel object
333 recognition test, mice were presented with a novel object 14-16 hours after the mouse

was exposed to the familiar objects for testing short-term object recognition memory. Homozygous mice showed a significantly reduced preference to the novel object (Figure 8B), suggesting a deficit in short-term memory recall. Next, we used auditory-cued fear conditioning to test fear associative memory. The freezing response of KIF5B conditional knockout mice was similar to wild-type in the acquisition phase (Figure 8-figure supplement 2C), but homozygous mice showed a significant decrease of freezing response to the conditioned stimulus (CS, auditory cue) during the recall test 48 hours after fear acquisition (Figure 8C). Since there was no significant difference in the trend of fear acquisition, this data indicates that homozygous mice show deficit in fear memory recall. The absence of significant deficits in heterozygous mice in these memory tests suggests the dose-dependent role of KIF5B in memory formation and retrieval. We next investigated the effect of KIF5B conditional knockout in spatial memory without using heterozygous conditional knockout mice. In Barnes maze test, mice were trained to locate the escape chamber among the 20 holes in the maze during the acquisition phase based on contextual cues. Wild-type mice showed a learning progress during the acquisition phase as indicated by a decreasing trend of primary errors they made during training, but such learning progress was not observed in homozygous mice. Homozygous mice also tended to stay in the wrong target hole instead of exploring the environment which in turn

353 showing fewer primary errors when compared to wild-type (Figure 8-figure
354 supplement 2D). Nonetheless, homozygous mice showed a significantly higher
355 primary latency to locate the escape hole when compared to wild-type during the
356 recall test five days after the training (Figure 8D).

357 Since the results of the behavioral tests strongly suggest deficits in
358 hippocampal-dependent functions, we examined the expression of long-term
359 potentiation (LTP) at the Schaffer collateral (SC)-CA1 synapses from acutely
360 prepared hippocampal slices of the control and KIF5B homozygous conditional
361 knockout mice. While LTP could be induced in both control and homozygous
362 hippocampal slices, the LTP decayed faster at the homozygous SC–CA1 synapses,
363 and the field EPSP amplitude during the last 10 min recording was significantly
364 reduced at the homozygous SC–CA1 synapses when compared to wild-type (Figure
365 8E). There was no significant difference in input/output relationship between
366 wild-type and homozygous mice, indicating the baseline synaptic response was not
367 changed (Figure 8F). To test whether presynaptic function was altered, the pair-pulse
368 ratios were measured with several different inter-pulse durations. We found no
369 significant difference in pair-pulse ratio between wild-type and homozygous mice,
370 indicating similar presynaptic responses (Figure 8G). Taken together, these findings

suggest that conditional knockout of *Kif5b* causes memory recall deficits in social memory, object recognition memory, fear associative memory, and spatial memory, showing the important role of KIF5B in memory formation and retrieval. These memory deficits are associated with impaired long-term synaptic plasticity in the hippocampus. Moreover, the synaptic and memory deficits in the KIF5B conditional knockout mice cannot be compensated by the presence of the other two homologous KIF5s.

DISCUSSIONS

Many studies have examined the functional significance of individual kinesin through exogenous expression of dominant-negative construct, which usually contains the tail domain of the kinesin of interest without the motor domain and hence does not move along microtubule. This approach is useful to demonstrate the effect of competitive binding between the dominant negative protein and endogenous motors for the cargoes. Using an alternative approach to delineate the function of individual KIF by RNAi or gene knockout, we demonstrate the important roles of KIF5B in regulating dendritic spine development and maintenance both in dissociated neurons *in vitro* and in the animal *in vivo*. Through the generation of conditional knockout

388 mice in which the *Kif5b* gene is ablated only after birth in order to avoid lethality, we
389 are able to demonstrate the physiological significance of KIF5B in regulating
390 excitatory synaptic plasticity as well as learning and memory. Our findings provide
391 compelling evidences that the function of KIF5B in neuron cannot be compensated by
392 the other two neuron-specific KIF5s.

393 Since only one KIF5 is expressed in invertebrates, it appears that the
394 neuronal-specific KIF5A and KIF5C evolve specifically for higher brain function in
395 vertebrates. We found that knock down of either KIF5B or KIF5C, but not KIF5A,
396 reduced mushroom spines. On the other hand, co-expression of KIF5C but not KIF5A
397 can rescue the loss of mushroom spines caused by KIF5B-shRNA. These finding
398 indicates that KIF5B and KIF5C share functional similarity in dendritic spine
399 morphogenesis and their roles cannot be replaced by the functionally distinct KIF5A.
400 However, in the KIF5B conditional knockout mice in which KIF5C expression
401 remains unaffected, reduction in both spine density and mEPSC is observed in
402 hippocampal neurons. Therefore, the impaired synaptic function due to KIF5B
403 deficiency cannot be compensated by KIF5C in the postnatal brain. One possible
404 explanation is that KIF5B is the more prominently expressed kinesin compared to
405 KIF5C in the adult hippocampus as shown by quantitative immunoblot (Kanai et al.

406 2000). The presence of KIF5C in the conditional knockout mice may not be sufficient
407 to compensate for the shortage of motor proteins after ~50% reduction of KIF5B
408 expression.

409 The carboxyl termini of the three KIF5s share little amino acid sequence
410 similarity. The carboxyl terminus may not bind to cargo directly since GST-KIF5B
411 constructs without this region (a.a. 936-963 of KIF5B) still pull down various cargoes
412 (Setou et al. 2002; Cho et al. 2007; Xu et al. 2010; Barry et al. 2014; Lin et al. 2019).
413 Our present findings also suggest that the carboxyl-terminus is not directly involved
414 in FMRP binding because removing it (amino acid residues 939-1027) from KIF5A
415 increases, rather than decreases, the pull-down of FMRP. Furthermore, although
416 replacement of the KIF5A carboxyl-terminus by the KIF5B counterpart increases the
417 binding to FMRP and G3BP1, given that the input of the KIF5B is much less than the
418 chimeric KIF5A (Fig. 4A), it is likely that equal amount of KIF5B would pull down
419 much more FMRP and G3BP1. This again points to the involvement of KIF5
420 sequence besides the carboxyl-terminus in cargo-binding. Nonetheless, the rescue
421 experiments with chimeric KIF5A have unraveled a new function of the
422 carboxyl-terminus in determining functional specificity of KIF5s. Substituting the
423 carboxyl terminus of KIF5A by that of KIF5B is sufficient to transform KIF5A into a

kinesin motor that enhances spine maturation. In this regard, it is noteworthy that the longer carboxyl-terminus of KIF5A binds directly to $GABA_A$ receptor-associated protein for the development of inhibitory synapses (Nakajima et al., 2012). Our findings together raise the interesting possibility that there is a division of labor among the two KIF5s in regulating excitatory and inhibitory synapses, and the evolution of their diverse carboxyl-termini confer them functional specificities.

Many axonal cargos, such as syntabulin, SNAP25 and amyloid precursor protein (APP) have been identified for KIF5s (Hirokawa and Tanaka, 2015; Kamal et al., 2000). KIF5 motor domain also predominately recognizes axonal rather than dendritic microtubules, which highlight its functional significance in axon (Kapitein et al., 2010). However, KIF5 is also implicated in the transport of cargoes such as $GABA_A$ receptor (Twelvetrees et al., 2010; Nakajima et al., 2012), AMPA receptor (Heisler et al., 2014; Setou et al., 2002) and RNPs (Kanai et al., 2004), which are believed to be mainly carried to the dendrites of mature neurons. We found that KIF5B is localized not only in the axons, but is also present in the dendrites and dendritic spines of dissociated hippocampal neurons, supporting the role of dendritic KIF5B in the development of excitatory postsynaptic sites. Although it was originally thought that microtubule is not present in dendritic spines, emerging study has revealed the

invasion of microtubule and kinesin to the spine heads from dendritic shaft, which are crucial for dendritic spine plasticity (Jaworski et al., 2009; McVicker et al., 2016). Our findings suggest that KIF5B might represent one of the kinesin motors that deliver synaptic proteins to the dendritic spines.

Dendritic spines exist as heterogeneous morphologies, which are usually classified into short stubby spines with no apparent spine neck, thin spines with elongated necks and small heads, mushroom-shaped spines with large bulbous heads, and filopodia which are long and thin and do not possess a PSD (Ziv and Smith, 1996; Bourne and Harris, 2007; Lai and Ip, 2013; Berry and Nedivi, 2017). Stubby and filopodia are regarded as immature dendritic protrusions because they are relatively scarce in the mature brain (Harris et al., 1992). The distinct morphologies are critical to determine the properties and functions of dendritic spines. These include signal compartmentalization, calcium dynamics, capacity of local translation, and turnover (McKinney, 2010). Mushroom spines possess larger PSD which are correlated with greater synaptic strength and stability for information storage; while the dynamic thin spines are transient, but they may become persistent in response to a learning paradigm and contribute to the remodeling of neural circuits (Bourne and Harris, 2007; Berry and Nedivi, 2017). It is interesting that knockdown of KIF5B specifically

460 decreases mushroom spines in cultured hippocampal neurons while increasing the
461 abundance of the other three types of spines. Emerging studies have demonstrated that
462 different spine types can be regulated differentially and independently (Sanders et al.,
463 2012; Spiga et al., 2014). At the molecular level, we have also identified the
464 postsynaptic scaffolding protein STRN4, which is encoded by a dendritic mRNA and
465 its expression depends on NMDA receptor activity, is involved specifically in the
466 maintenance of mushroom spines (Lin et al., 2017). It is tempting to speculate that a
467 subset of proteins and/or mRNAs may depend on KIF5B for the delivery to
468 mushroom spines that confer their selective maintenance.

469 Since KIF5s can pull down RNPs from the brain (Kanai et al., 2004), one
470 possible mechanism by which KIF5B promotes the maintenance of mushroom spines
471 is through the dendritic transport of mRNAs and RNA-binding proteins. We have
472 found that knockdown of KIF5B reduced the dendritic localization of FMRP and two
473 associated RNA transcripts as compared to knockdown of KIF5A, indicating their
474 differential functions in dendritic transport of mRNAs. This may explain the altered
475 spine morphology after knockdown of KIF5B, since the depletion of FMRP in mouse
476 brain also resulted in an increase of dendritic filopodia (Comery et al., 1997). The
477 local translation of CaMKIIα and Grin2b mRNAs is critical to synaptic plasticity

478 (Kuklin et al., 2017; Williams et al., 2007), which may contribute to the disrupted LTP
479 in mouse hippocampus upon KIF5B depletion. FMRP and associated mRNA transport
480 involves interaction with KLC (Dictenberg et al., 2008). Since both KIF5A and
481 KIF5B contain the conserved KLC binding domain, there could be additional
482 mechanism that underlies the specific role of KIF5B in FMRP transport, which may
483 involve the preferential interaction between FMRP and the KIF5B tail domain as
484 revealed by the pull-down assay. It is also intriguing that KIF5B-shRNA only leads to
485 fewer stationary granules on dendrites without affecting the motile oscillatory,
486 unidirectional and bidirectional granules. Since other kinesins besides KIF5 can also
487 bind to FMRP (Charalambous et al., 2013; Davidovic et al., 2007), we speculate that
488 different pools of FMRP granules are carried by different KIFs, with KIF5B mainly
489 responsible for the less motile granules while other KIFs transport the more motile
490 pools of FMRP. It was recently reported that different KIFs transport cargoes with
491 different velocities and MAP2 inhibits KIF5B activity in dendrites by interacting with
492 the coiled-coil region and blocking microtubule binding (Gumy et al., 2017). This
493 study therefore suggests that KIF5B-mediated transport in dendrites is ineffective as
494 compared to other kinesins. Alternatively, since microtubule and dynein are required
495 for mRNA anchoring in *Drosophila* embryos (Delanoue and Davis, 2005), it is also
496 possible that besides a conventional transport function, KIF5s may help anchoring the

497 dendritically localized FMRP and mRNAs near synapses for local translation in
498 response to extracellular stimuli such as BDNF or synaptic activity (Schratt et al.,
499 2004).

500 The function of kinesin is regulated by post-translational modification. Previous
501 studies on the Kinesin-2 motor protein KIF17 revealed a novel mechanism of cargo
502 release through calmodulin-dependent protein kinase (CaMKII)-mediated
503 phosphorylation, which disrupts the interaction with the adaptor protein LIN10 and
504 unloads the NMDA receptor subunit 2B (GluN2B) containing vesicles (Guillaud et al.,
505 2008). On the other hand, the association between synaptotagmin-containing vesicles
506 and the motor adaptor UNC76 of KIF5 in *Drosophila* is strengthened by
507 phosphorylation (Toda et al., 2008). In the present study, we have characterized the
508 methylation of two RGG motifs within the carboxyl-terminus of KIF5B involving
509 Arg-941 and Arg-956. Invertebrates such as *C. elegans* have shorter
510 carboxyl-terminus of KIF5 that lacks the RGG motif, while *Drosophila* has one RGG
511 motif containing Arg-956, same as the mammalian KIF5C. The two RGG motifs in
512 KIF5B are conserved across many vertebrates, indicating the importance of arginine
513 methylation. Here we show that the methylation in KIF5B regulates interaction of the
514 motor protein with FMRP and it is essential for the formation of mushroom spines,

515 therefore unraveling a previously unidentified PTM in regulating kinesin function.
516 There are extensive cross-talks between arginine methylation and other PTMs, such as
517 phosphorylation, ubiquitination, and acetylation (Basso et al., 2015; Yang et al., 2018).
518 Future studies are needed to investigate how arginine methylation of KIF5B may
519 interact with other forms of PTM in regulating cargo-binding of the motor protein.

520 Does KIF5B play any specific role in learning and memory? To answer this
521 question, we generated the KIF5B conditional knockout mouse line in
522 CaMKIIα-expressing neurons. Since the expression of CaMKIIα is developmentally
523 regulated and is restricted to the forebrain with high levels in the pyramidal neurons
524 of the neocortex and hippocampus (Dragatsis and Zeitlin, 2000; Tsien et al., 1996), we
525 can specifically knockout KIF5B postnatally without affecting early
526 neurodevelopment. Here we demonstrated that specific knockout of *Kif5b* in
527 CaMKIIα-expressing neurons leads to deficits in memory recall in social memory,
528 novel object recognition, auditory-cued fear conditioning, and spatial memory tests,
529 with no significant deficit during initial memory acquisition phase. Furthermore, the
530 KIF5B conditional knockout mice show deficits in the maintenance of LTP in CA1
531 hippocampal neurons and the loss of dendritic spines. Although there is no significant
532 decrease of dendritic spine density in the frontal association cortex of conditional

knockout mice, the rates of dendritic spine formation and elimination are significantly higher at different time points in two-photon *in vivo* imaging, suggesting the increase of dendritic spine instability in this region. Increase in dendritic spine instability has been commonly found in various disease models, such as Fragile X syndrome (Nagaoka et al., 2016; Pan et al., 2010), schizophrenia (Fenelon et al., 2013), spinocerebellar ataxia type 1 (Hatanaka et al., 2015) and Huntington disease (Murmu et al., 2013). It has been found that a small fraction of the population of transient spines grows after experience or behavioral training over days can be stabilized over the animal's lifetime, contributing to long-lasting circuit remodeling associated with new experience (Yang et al., 2009). The enhanced dendritic spine instability in KIF5B conditional knockout mice could contribute to brain dysfunction and deficits in learning and memory. Since the frontal cortex maturation happens at later developmental stage (Caballero et al., 2016; Gogtay et al., 2004; Zuo et al., 2005), the lack of dendritic spine density difference in the frontal association cortex between wild-type and KIF5B conditional knockout mice could be due to the delay of frontal cortex maturation and pruning in the conditional knockout mutant. Nonetheless, the impairments in memory recall, LTP maintenance, and dendritic spine deficits in KIF5B conditional knockout demonstrate the crucial role of KIF5B in learning and memory that cannot be compensated by KIF5A and KIF5C *in vivo*. The process of

552 memory storage is not a random event. The synaptic tagging and capture hypothesis
553 proposes that the synapses activated during LTP induction become “tagged”
554 (Rogerson et al., 2014). These tagged synapses become a target for subsequent
555 plasticity-related product (PRP) trafficking. The capture of these PRPs by specific
556 synapses is essential for their structural modification, as well as the maintenance of
557 LTP and long-term memory formation. The deficits that we observed in KIF5B
558 conditional knockout mice could be stemmed from the impairment of PRP trafficking
559 specifically delivered by KIF5B in dendrites in response to activity-dependent
560 plasticity.

561 Taken together, our findings have revealed the significance of KIF5B in
562 regulating excitatory synapse development and function of neuron both *in vitro* and *in*
563 *vivo*, and support the notion that the three homologous KIF5s have non-redundant
564 functions in the brain. It is plausible that homologous members of the other kinesin
565 families also exhibit functional specificity in the brain, an interesting research area
566 which warrants further study in the future.

567 **Materials and Methods**

568

569 **Key resources table**

Reagent type (species) or resource	Designation	Source or reference	Identifiers	Additional information
strain, strain background (M. musculus)	C57/6J	The University of Hong Kong Laboratory Animal Unit		
genetic reagent (M. musculus)	Thy1-YFP-H	Jackson Laboratory.	003782 |thy1-YFP-H	
genetic reagent (M. musculus)	CaMKIIα-Cre	Jackson Laboratory.	005359 |T29-1	
genetic reagent (M. musculus)	Kif5bfl/fl	Jiandong Huang	PMID: 20870970	
genetic reagent (M. musculus)	CaMKIIα-Cre;Kif5bfl/fl	This paper		generated from breeding of CaMKIIα-Cre and Kif5bfl/fl mice
transfected construct (M. musculus)	FLAG-677-1027 KIF5A	This paper		aa 677-1027 of mouse KIF5A with a N-terminal FLAG tag was inserted into pcDNA3
transfected construct (M. musculus)	FLAG-677-939 KIF5A	This paper		aa 677-939 of mouse KIF5A with a N-terminal FLAG tag was

				inserted into pcDNA3
transfected construct (M. musculus)	FLAG-677-938 KIF5A+941-963 KIF5B	This paper		aa 677-938 of mouse KIF5A and aa 941-963 of mouse KIF5B with a N-terminal FLAG tag was inserted into pcDNA3
transfected construct (M. musculus)	FLAG-680-963 KIF5B	This paper		aa 680-963 of mouse KIF5B with a N-terminal FLAG tag was inserted into pcDNA3
transfected construct (R. norvegicus)	KIF5A shRNA	This paper		5’-TGGAAACGC CACAGATATC-3 ’
transfected construct (M. musculus)	KIF5B shRNA	This paper		5’-GGACAGATG AAGTATAAAT-3’
transfected construct (R. norvegicus)	KIF5C shRNA	This paper		5’-GACCCTGGC AGATGTGAAT-3 ’
transfected construct (R. norvegicus)	control shRNA	Lin et al., 2017	PMID: 28442576	5’-GGCTACCTC CATTTAGTGT-3’
transfected construct (M. musculus)	pKin1A	Anthony Brown	RRID:Addgene_31607	
transfected	pcDNA3-KIF5B	Jiandong Huang	PMID:	

construct (M. musculus)			23293293	
transfected construct (M. musculus)	pGFP-Kif5c	Michelle Peckham	RRID:Addgene_71853	
biological sample (R. norvegicus)	Primary hippocampal neuron; primary cortical neuron	Lin et al., 2017	PMID: 28442576	Procedures of preparing primary neurons were described in Lin et al., 2017
biological sample (M. musculus)	Synaptoneurosome	Scheetz et al., 2000	PMID: 10700251	Procedures of preparing synaptoneurosome were described by Scheetz et al., 2000
biological sample (M. musculus)	Synatpic plasma membrane	Bermejo et al., 2014	PMID: 25226023	Procedures of preparing synaptic plasma mebrane were described by Bermejo et al., 2014
antibody	KIF5B	Jiandong Huang	PMID: 20870970	
antibody	KIF5A	Abcam	RRID:AB_2132218	
antibody	KIF5C	Abcam	RRID:AB_304999	
antibody	FMRP	Abcam	RRID:AB_2278530	
antibody	KIF17	Sigma	RRID:AB_477148	
antibody	FLAG	Sigma	RRID:AB_	

			262044	
antibody	G3BP1	Bethyl	RRID:AB_1576539	
antibody	G3BP2	Bethyl	RRID:AB_1576545	
antibody	GluA2	Millipore	RRID:AB_2113875	
antibody	RNMT	Millipore	RRID:AB_11215450	
antibody	NRGN	Millipore	Cat#AB5620	
antibody	NeuN	Millipore	Cat#AB377	
antibody	PSD-95	NeuroMab	RRID:AB_2292909	
antibody	methylated mono-arginine R*GG	Cell Signaling	RRID:AB_10896849	
antibody	Mouse IgG2a anti-GFP	Invitrogen	RRID:AB_221568	
antibody	Rabbit anti-RFP	Rockland	RRID:AB_2209751	
antibody	Alexa 488 anti mouse IgG2a	Invitrogen	RRID:AB_2535771	
antibody	Alexa 546 anti rabbit IgG	Invitrogen	RRID:AB_2534077	
antibody	horseradish peroxidase-conjugated goat anti-rabbit IgG	Cell Signaling	RRID:AB_2099233	
antibody	horseradish peroxidase-conjugated goat anti-mouse IgG	Cell Signaling	RRID:AB_330924	
recombinant DNA	pFRT-TODestFLAGHAhFMRPiso	Thomas Tuschl	RRID:Addgene_4869	

reagent	1		0	
recombinant DNA reagent	tdTomato	Michael Davidson	RRID:Addgene_54653	
recombinant DNA reagent	GST-fused KIF5A	This paper		aa 677-1027 of mouse KIF5A was inserted into pGEX-6P-2
recombinant DNA reagent	GST-fused KIF5B	This paper		aa 680-963 of mouse KIF5B was inserted into pGEX-6P-2
recombinant DNA reagent	GST-fused KIF5C	This paper		aa 681-956 of mouse KIF5C was inserted into pGEX-6P-2
recombinant DNA reagent	pEGFP-N1-KIF5A	This paper		Constructed by inserting PCR-amplified mouse KIF5A coding sequences into the pEGFP-N1 plasmid using KpnI and BamHI
recombinant DNA reagent	pEGFP-N1-KIF5B	This paper		Constructed by inserting PCR-amplified mouse KIF5B coding sequences into the pEGFP-N1 plasmid using KpnI and BamHI
sequenced-based reagent	Grin2b transcript probe (NM_012574.1,	ThermoFisher	Cat#VC1-16464	

	type 1)			
sequenced-based reagent	Type 1 sense probe	ThermoFisher	Cat#VC1-20903	
sequenced-based reagent	CaMKIIa transcript probe (NM_012920.1, type 6)	ThermoFisher	Cat#VC6-11639	
sequenced-based reagent	Type 6 sense probe	ThermoFisher	Cat#VC6-16372	
chemical compound, drug	FLAG beads	Sigma	RRID:AB_10063035	
chemical compound, drug	glutathione sepharose 4 fast flow beads	GE Healthcare	Cat#17-5132-01	
chemical compound, drug	Protein A-Sepharose beads	GE Healthcare	Cat#17-5280-01	
commercial assay or kit	Lipofectamine LTX with Plus Reagent	ThermoFisher Scientific	Cat#15338100	
commercial assay or kit	SilverQuest™ Silver Staining Kit	Life technologies	Cat#LC6070	
commercial assay or kit	ViewRNA™ ISH Cell Assay Kit	ThermoFisher	Cat#QVC0001	
commercial assay or kit	Neon transfection system	ThermoFisher Scientific		Model MPK5000
software, algorithm	Volocity	Quorum Technologies	RRID:SCR_002668	
software, algorithm	Zen digital imaging software	Zeiss	RRID:SCR_013672	
software,	Actimetrics	Coulbourn Instruments	RRID:SCR	Version 2.2

algorithm	FreezeFrame software		_014429	
software, algorithm	ANY-maze software	ANY-maze	RRID:SCR_014289	
software, algorithm	MetaMorph software	Molecular Devices	SCR_002368	
software, algorithm	GraphPad Prism	GraphPad Prism (https://graphpad.com)	RRID:SCR_015807	Version 6
software, algorithm	FIJI	FIJI (https://imagej.net/Fiji)	RRID:SCR_002285	
software, algorithm	KymoResliceWide	Eugene Katrukha (https://github.com/ekatrukha/KymoResliceWide)		
software, algorithm	Straighten	Eva Kocsis (https://imagej.nih.gov/ij/plugins/straighten.html)	PMID: 1817611	
software, algorithm	Mini Analysis Program	Synaptosoft	RRID:SCR_002184	
software, algorithm	CLC Main Workbench	Qiagen (https://www.qiagenbioinformatics.com/products/clc-main-workbench/)	RRID:SCR_000354	

570

571 *Antibodies, chemicals and DNA constructs*

572 Antibody against KIF5B was previously described (Cui et al., 2011), while
573 others were purchased commercially, including antibodies against KIF5A, KIF5C,
574 FMRP (Abcam), KIF17, FLAG (Sigma), G3BP1, G3BP2 (Bethyl), GluA2, RNMT,
575 NRGN and NeuN (Millipore), PSD-95 (NeuroMab), methylated mono-arginine
576 R*GG (Cell Signaling), GFP (Invitrogen), and RFP (Rockland). Alexa-conjugated

secondary antibodies (Invitrogen) were used for immunofluorescence and horseradish peroxidase-conjugated goat anti-rabbit IgG or anti-mouse IgG (Cell Signaling) were used for western blot analysis.

For the specific knockdown of KIF5A, KIF5B, and KIF5C, a 19-nucleotide (KIF5A: 5’-TGGAAACGCCACAGATATC-3’, KIF5B: 5’-GGACAGATGAAGTATAAAT-3’, KIF5C: 5’-GACCCTGGCAGATGTGAAT-3’) sequence derived from the rat KIF5A mRNA, mouse KIF5B mRNA at the 3’-UTR and rat KIF5C mRNA were used to create the shRNA constructs after subcloning into the pSUPER vector (Oligoengine). The sequence of control shRNA is 5’-GGCTACCTCCATTTAGTGT-3’. Full-length mouse KIF5A and KIF5C constructs were obtained from Quan Hao (The University of Hong Kong), and the coding sequence was amplified and subcloned into pcDNA3 backbone. Full-length mouse KIF5B was amplified by PCR using the plasmid pcDNA3-FLAG-KIF5B as template, which contains the insert of full-length mouse KIF5B coding region. Methylation-deficient R941H, R956H and R941/956H constructs were created by site-directed mutagenesis and the PCR products were digested by DpnI (NEB) at 37°C water bath for 3 hours before transformation into E. coli competent cells. The nucleotide sequence was verified by Sanger sequencing. For GFP-FMRP construct,

the human FMRP coding sequence was amplified from the plasmid pFRT-TODestFLAGHAhFMRPiso1 that was from Thomas Tuschl (Addgene #48690) and cloned into the pEGFP-C1 backbone using SacI and EcoRI. KIF5A-GFP and KIF5B-GFP were constructed by inserting PCR-amplified mouse KIF5A and KIF5B coding sequences into the pEGFP-N1 plasmid using KpnI and BamHI. All PCR in this study was performed using high-fidelity Pfu DNA polymerase (Agilent Technologies, Inc.).

Animals

Mice were group housed under a 12-hour light/dark cycle, with food and water available ad libitum. C57BL/6 mice expressing CaMKIIα-Cre and yellow fluorescent protein (YFP) in layer V pyramidal neurons (*Thy1*-YFP-H) and CaMKIIα promoter-driven Cre transgenic mice were purchased from the Jackson Laboratory. *Kif5b*$^{fl/fl}$ mice were described previously (Cui et al., 2011). CaMKIIα promoter-driven Cre transgenic mice were used to conditionally delete exons flanked by loxP. Mice were then further crossed with *Thy1*-YFP-H line to allow imaging of layer V pyramidal neurons. Sample size was decided based on experiments in previous studies (Lai et al., 2012; Yang et al., 2014). For animal behavioral tests and *in vivo* imaging experiments, results from at least two independent experiments were pooled together

for analysis. Mice were group housed in The Laboratory Animal Unit, The University of Hong Kong, accredited by Association for Assessment and Accreditation of Laboratory Animal Care International. Four to five weeks old mice were used in this study unless stated otherwise. All experiments were approved and performed in accordance with University of Hong Kong Committee on the Use of Live Animals in Teaching and Research guidelines.

Electrophysiology

Whole-cell recordings were obtained by the MultiClamp 700B amplifier (Molecular Devices). For cultured hippocampal neurons, which were recorded at DIV 16-17, the pipettes with a resistance of 3-5 MΩ were filled with the internal solution consisting of 115 mM CsCl, 10 mM HEPES, 2 mM $MgCl_2$, 4 mM NaATP, 0.4 mM NaGTP, 0.5 mM EGTA, and pH was adjusted to 7.2-7.4 by CsOH. The neurons were perfused with the external solution of the following composition: 110 mM NaCl, 5 mM KCl, 2 mM $CaCl_2$, 0.8 mM $MgCl_2$, 10 mM HEPES, 10 mM Glucose, and pH was adjusted to 7.2-7.4 by NaOH. For miniature excitatory postsynaptic currents (mEPSCs) recording, tetrodotoxin (1 μM) and bicuculline (20 μM) were added into the external solution to block action potentials and the inhibitory current from GABA receptor, respectively. The signals were filtered at 2 kHz and sampled at 20 kHz using

631 the Digidata 1440A (Molecular Devices). The holding potential is at -70 mV, and the
632 recording lasts for 5 to 10 min. The data were analyzed by the commercial software
633 MiniAnalysis (Synaptosoft).

634 For recording mEPSCs in dorsal hippocampal CA1 brain slices, postnatal day (P)
635 45±3 wild-type and KIF5B conditional knockout mice were perfused by ice-cold
636 dissection buffer (92 mM NMDG, 2.5 mM KCl, 1.25 mM NaH_2PO4, 30 mM
637 $NaHCO_3$, 25 mM glucose, 20 mM HEPES, 5 mM Na-ascorbate, 3 mM Na-pyruvate,
638 2 mM thiourea, 10 mM $MgSO_4$ and 0.5 mM $CaCl_2$ pH=7.1-7.3) after euthanized. The
639 brains were taken out immediately and submerged in ice-cold dissection buffer.
640 Coronal brain slices containing CA1 were sectioned in 250 μm by vibratome. Slices
641 were recovered in warm artificial cerebral spinal fluid (ACSF) at 32℃ for 15 minutes,
642 followed by room temperature incubation. The recordings were performed in ACSF at
643 room temperature. The ACSF consisted of the following (in mM): 119 NaCl, 2.5 KCl,
644 1 $MgCl_2$, 2 $CaCl_2$, 26 $NaHCO_3$, 1.23 NaH_2PO4 and 10 glucose. All solutions were
645 oxygenated by 95% O_2/5% CO_2. Internal solution consisted of the following (in mM)
646 131 Cs-methanesulfonate, 20 CsCl, 8 NaCl, 10 HEPES, 2 EGTA, 2 NaATP and 0.3
647 NaGTP, pH7.3, osmolarity 290 mOsm. The glass micropipette was filled with internal
648 solution (resistance 4-6 MΩ) and connected to the electrode for recording. The

mEPSCs were recorded with the presence of 1μM tetrodotoxin, 10μM bicuculline and 1μM strychnine.

For recording LTP, hippocampal slices from the wild-type and the KIF5B conditional knockout mice (3 months old) were prepared. A planar multi-electrode recording setup (MED64 system, Alpha Med Sciences Co., Ltd, Japan) was employed to record the field excitatory postsynaptic potential (fEPSP), and to study LTP. Briefly, hippocampal slices were placed on special probes that were fabricated with 8x8 electrode arrays and pre-coated with polyethylenimine (PEI, Sigma). The P210A probes (Alpha Med Sciences) with an inter-electrode distance of 100 μm were routinely used. Correct placement of the electrodes at the CA3–CA1 region was done manually, monitored by a microscope (MIC-D, Olympus Ltd., Japan). To increase the efficiency of the experiments and to minimize the variation in the results arising from differences in incubation times, a maximum of 4 slices were studied simultaneously. Each slice was superfused by oxygenated ACSF. fEPSPs were recorded from the dendritic layer of CA1 neurons by choosing an electrode in the Schaffer collateral pathway as the stimulating electrode. Based on the stimulus–response curve, we chose a stimulation intensity that evoked the fEPSP with a magnitude of 30–40% of the maximum response. After allowing a stable baseline of 30 min, an induction protocol

consisting of 1 train of 100 Hz stimulus that lasted for 1 s was applied, and the field potential response for 1 h after the tetanus was recorded. The magnitude of the LTP was quantified as % change in the average amplitude of the fEPSP taken from 50 to 60 min interval after induction. To assess basal synaptic transmission, the input-output relationship was generated by delivering 10–100-μA electrical stimuli, and the amplitude of the peak fEPSPs was measured. To characterize the paired-pulse ratio, twin stimuli that were separated by a variable time interval (50, 100, 150, 200 or 400 ms) were delivered to the CA3-CA1 pathway ten times each, and the average ratio of the amplitude of the second evoked fEPSPs over the first one was determined. All the electrophysiology experiments were performed and analyzed blinded.

Primary cell culture and transfection

Primary hippocampal neurons and cortical neurons were prepared from embryonic day 18-19 embryos of Sprague Dawley rats according to our previous study (Lin et al., 2017). Hippocampal neurons were cultured on 18-mm coverslips or 35-mm MatTek dishes (with 14mm central glass, MatTek corp) dishes coated with poly-D-lysine (1 mg/ml, Sigma P0899) at high density (1.4 x 10^5 cells per coverslip for dendritic spine analysis; 2 x 10^5 per cover glass on MatTek dish for live cell imaging of GFP-FMRP) or low density (0.4 x 10^5 cells per coverslip for FISH and

685 immunofluorescence staining) in Neurobasal medium supplemented with 2% B27 and
686 0.5% L-glutamate. Hippocampal neurons were transfected with different plasmids
687 using calcium phosphate precipitation as previously described (Lai et al., 2008).
688 Cortical neurons were transfected by electroporation using the Neon transfection
689 system (ThermoFisher Scientific), in which a total of 1 x 10^6 cells in suspension were
690 electroporated in each reaction with the parameter of 1500V pulse voltage and 20 ms
691 pulse width. After electroporation, cells were plated on 35mm dishes and cultured for
692 5 days before Western blot analysis.

693 *Live cell imaging and image analysis*

694 Images were taken using Perkin Elmer UltraView Vox Spinning Disk Confocal
695 Microscope 60x oil-immersion objective (NA 1.40) at a resolution of 512 x 512 pixels,
696 1 frame per second for 100 seconds. Images were exported using Volocity software
697 and processed using FIJI software. Kymographs of selected dendrites were generated
698 in FIJI software using the "KymoResliceWide" plugin. The kymographs were
699 randomized and reviewed blindly, and images with low signal-to-noise ratio were
700 excluded due to the difficulty in quantification. The movement of individual granules
701 in selected kymographs was then traced manually by drawing polygonal lines as
702 overlays on the image and the traces were reviewed by an experimenter blind to the

703 conditions. Minimum and maximum values of the kymographs were constantly
704 adjusted during manual tracing due to uneven intensity on different segments of the
705 dendrite but were limited to a range that was considered appropriate for that batch of
706 images. The traces were then exported with information of the x and y coordinates of
707 each point on the polygonal lines. To classify the type of movement exhibited by each
708 granule, the net displacement (ND) and lateral maximal displacement (LMD) were
709 measured. ND is defined as the difference in x coordinates of the first point and the
710 last point of the trace. Lateral maximal displacement (LMD) is defined as the absolute
711 value of maximal difference in x coordinates of all the points on the trace (the
712 difference between the most proximal point and the most distal point). Granules with
713 ND ≧2 μm are defined as unidirectional, within which the granules with ND > 0 are
714 defined as anterograde (from soma towards distal dendrite) and granules with ND < 0
715 are defined as retrograde (from distal dendrite to soma). For granules with ND < 2 μm,
716 granules with LMD < 1μm are defined as stationary; granules with 1μm≦LMD < 2μm
717 are defined as oscillatory; while granules with LMD ≧ 2μm are defined as
718 bidirectional. The motility of each granule in unidirectional or bidirectional
719 movements was further quantified in terms of travel distance, maximal run length and
720 maximal velocity. Travel distance is defined as the total length of the granule
721 trajectory within 100 seconds. The maximal run length is defined as the largest x-axis

distance of a period of movement with constant velocity. The maximal velocity is defined as the maximum of all velocity values of a granule, which is calculated by dividing the x-axis distance of each segment of the trajectory by the y-axis distance (the time covered by this segment).

Fractionation of synaptic plasma membrane (SPM) and Western blot analysis

SPM fraction was prepared using sucrose gradient method as described (Bermejo et al., 2014). Briefly, mouse brains (~P20) were homogenized in 0.32M HEPES-buffered sucrose solution. The homogenate was either centrifuged at 13000 rpm for 10 minutes (min) yielding the supernatant (Homo) for western blot analysis, or subjected to fractionation. The homogenate was centrifuged at 900 x g for 10 minutes (min) to remove nuclear fraction and the crude synaptosomal fraction (P2) was enriched from the supernatant using two times of centrifugation at 10000 x g for 15 min. The P2 pellet was later subjected to hypo-osmotic shock and centrifugation at 25,000 x g for 20 min to yield the Synaptosomal Membrane Fraction (P3). The obtained pellet was then resuspended and loaded to a 0.8M/1.0M/1.2M HEPES-buffered sucrose gradient and centrifuged at 150,000 x g for 2 hours, separating fractions in different layers. The SPM fraction was collected at the 1.0M/1.2M interface, further centrifuged at 160,000 x g for 30 min, and resuspended

in 50 mM HEPES / 2 mM EDTA solution. For Western blot analysis, homogenate and SPM samples were diluted with RIPA buffer or 50 mM HEPES / 2 mM EDTA and denatured in sample buffer (5x sample buffer: 300 mM Tris-HCl buffer pH 6.8 10% (w/v) DSD, 25% (v/v) beta-mercaptoethanol, 50% (v/v) SDS, 25% (v/v) glycerol, 0.05% (w/v) bromophenol blue).

Synaptoneurosome (SNS) preparation, immunoprecipitation and Western blot analysis

The preparation of SNS was performed as previously described with modification (Scheetz et al., 2000). In brief, P15 mice were decapitated, and cerebellum together with the superficial, retinorecipient layers of the superior colliculus were removed. The rest of the brain tissues were homogenized in ice-cold homogenized buffer (5M NaCl, 1M KCl, 1M $MgSO_4$, 0.5M $CaCl_2$, 1M KH_2PO_4, 212.7 mM glucose, pH 7.4) supplemented with protease inhibitor cocktail (Roche). All subsequent steps were carried out at 4 °C. Samples were passed through a series of nylon filters of descending pore size. The final pass was through Millipore filter with a 10 μm pore size. Samples were then centrifuged for 15 minutes at 1,000 x g at 4°C. The supernatant was discarded, and the pellet was resuspended in 100 μl homogenization buffer for immunoprecipitation.

To test whether KIF5B was methylated in SNS, equal amount of SNS fraction

lysate (800 µg) was incubated with KIF5B or mono-methyl-arginine (Cell Signaling) antibody at 4°C with rocking overnight. Immunoprecipitate was obtained with RIPA buffer after incubation with Protein A-Sepharose beads (GE Healthcare) for 1 hour in cold room with rocking. Beads were washed four times with RIPA buffer containing various protease and phosphatase inhibitors (10 µg/ml soybean trypsin inhibitor, 10 µg/ml leupeptin, 10 µg/ml aprotinin, 2 µg/ml antipain, 30 nM okadaic acid, 5 mM benzamidine, 1 mM sodium orthovanadate, 1 mM PMSF, 1 mM sodium fluoride, 100 mM beta-glycerophosphate). Proteins were eluted by boiling in sample buffer for 6 min. The eluate was collected by centrifugation at 13000 rpm for 1 min at 4 °C and then subjected to SDS-PAGE and Western blot analysis. The protein extract was boiled in sample buffer for 5 minutes, separated by SDS-PAGE, and transferred onto PVDF membranes, followed by blocking with 5% skim milk in TBS with 0.1% Tween 20 (TBST) for 1 hour at room temperature (RT). The membrane was incubated at 4°C with primary antibody diluted in TBST containing 5% BSA overnight. After washing 3 times with TBST, membranes were incubated for 1 hour at RT with HRP-conjugated secondary antibody diluted in 5% skim milk in TBST. The HRP signal was detected by ECL (Thermo Scientific) and quantified by densitometry using Photoshop software.

776 To map the methylation sites of KIF5B, HEK-293T cells cultured in 100 mm
777 dishes with 80% confluence were transfected with various KIF5B plasmids using
778 Lipofectamine (ThermoFisher Scientific). Twenty-four hours after transfection, the
779 cells were washed by ice-cold D-PBS and lysed by RIPA containing various protease
780 and phosphatase inhibitors. Lysate was incubated at 4°C for 45 min and the cell debris
781 was cleared by centrifugation at 13000 rpm for 10 min at 4°C. Equal amount of lysate
782 (1 mg) was incubated with FLAG beads (Sigma) in cold room for 1 hour with rocking.
783 The FLAG-beads were centrifuged at 3000 x g for 1 min at 4°C and washed for three
784 times with RIPA buffer containing various protease and phosphatase inhibitors, and
785 proteins were eluted by boiling in sample buffer for 6 min. The eluate was collected
786 by centrifugation at 13000 rpm for 1 min at 4°C and then subjected to SDS-PAGE &
787 Western blot analysis.

788 For pull-down experiments, different FLAG-tagged segments from KIF5s were
789 transfected into HKE293T cells using Lipofectamine (ThermoFisher Scientific). After
790 24 hours' transfection, cell lysate was collected by RIPA buffer with various protease
791 and phosphatase inhibitors as described above. Equal amount of lysate (1 mg) was
792 incubated with FLAG beads (Sigma) for immunoprecipitation. SNS pellet was
793 collected and lysed with Tris buffer (20 mM Tris, 150 mM NaCl, 1 mM EDTA, 1 mM

794 EGTA, 5 mM NaF, 0.5% NP40). Equal amount of SNS fraction (1 mg) was incubated
795 with the immunoprecipitation from FLAG beads at 4°C with rocking overnight.
796 FLAG beads were centrifuged at 3000 x g for 1 min at 4°C and washed for three
797 times with Tris buffer containing various protease and phosphatase inhibitors. Protein
798 were eluted by boiling in sample buffer for 6 min and then subjected to SDS-PAGE &
799 Western blot analysis.

800 To validate KIFs expression in the KIF5B conditional knockout mice, brain
801 lysate was obtained from mice (P44). Protein levels were determined by blotting with
802 anti-KIF5A, anti-KIF5B, anti-KIF5C, anti-KIF17 (all 1: 1000) and anti-β-actin
803 (1:3000) antibodies.

804 *GST pull-down assay*

805 The recombinant GST-fused proteins were expressed by E.coli BL21 (DE3)
806 grown in LB culture medium. Isopropyl β-D-1-thiogalactopyranoside (0.1 mM) was
807 used to induce expression of GST-fused KIF5A (a.a.677-1027) at 28 °C for 5 h, while
808 0.5 mM isopropyl β-D-1-thiogalactopyranoside was used to express all other
809 GST-fused proteins at 37 °C for 3 h. Mice (~6-week old) were sacrificed and
810 forebrains were homogenized and lysed with Tris buffer. The brain lysate was
811 pre-cleared by glutathione sepharose 4 fast flow beads (GE health) and GST proteins

with rocking at 4°C for 1 h. Equal amount of pre-cleared brain lysate and beads were incubated with equimolar GST-fused proteins at 4°C for 2 h with end-over-end mixing. Then, the beads were washed with Tris buffer for three times. Proteins were eluted by boiling in sample buffer for 6 min and then subjected to Western blot or silver staining using SilverQuest™ Silver Staining Kit (Life technologies).

Fluorescence In Situ Hybridization (FISH)

FISH was performed using ViewRNA ISH Cell Assay Kit (ThermoFisher) following manufactural instructions. In brief, cells were fixed using 4% formaldehyde for 30 minutes and rinsed in 1 x PBS. Cells were then treated with detergent and incubated with custom designed probe sets against Grin2b transcript (NM_012574.1, type 1) and CaMKIIα transcript (NM_012920.1, type 6) for 3 – 4 hours, preamplifier mix for 30 minutes, amplifier mix for 30 minutes, and label probe sets for 30 minutes, all in 40 ℃. Coverslips were washed with wash buffer for 3 times in between. Anti-GFP antibody was subsequently used for immunostaining.

Immunofluorescence staining, image acquisition, and quantitative analysis

To stain GFP-transfected neurons for dendritic spine analysis, neurons were incubated with GFP antibody (1:2000) in GDB buffer at 4°C overnight. After washing

three times with phosphate washing buffer (20 mM phosphate buffer and 0.5M NaCl), neurons were incubated with Alexa488-conjugated anti-mouse IgG2a secondary antibody (1:2000 diluted in GDB buffer) at RT for 1 hour, followed by washing three times by the phosphate washing buffer before mounting. For other immunocytochemistry experiments, cells were fixed by 4% PFA/4% sucrose in D-PBS for 15 min at RT. After washing with D-PBS, cells were incubated with blocking buffer (0.4% Triton X-100 (vol/vol) and 1% BSA) for 45 min at RT, and incubated with primary antibodies in blocking buffer at 4°C overnight. Cells were washed 3 times with washing buffer (0.02% Triton X-100 and 1% BSA in PBS), incubated with anti-mouse IgG2a Alexa 488 conjugate and anti-rabbit IgG Alexa 546 conjugate at RT for 1 hour, followed by washing twice in washing buffer and once by D-PBS before mounting with Hydromount (National Diagnosis)..

Carl Zeiss LSM 700 confocal laser-scanning microscopes installed with Zen digital imaging software were used to acquire z-stack fluorescent images using a 63x oil-immersion objective (NA 1.40) with the following parameters: 1 AU or smaller pinhole, 0.5x optical zoom, scan speed 6-8, interval 0.35 μm with 16-bit dynamic range. The images from the same experiment were captured using identical acquisition settings, except for GFP or tdTomato (RFP) staining which served to

847 visualized dendritic arbors and spines. Images from 2-3 coverslips were acquired for
848 each experimental condition, and results from three independent experiments were
849 pooled together for analysis. Sample size was decided based on experiments in
850 previous studies (Lai et al., 2012; Lin et al., 2017).

851 For dendritic spine quantification in dissociated hippocampal neurons, images of
852 the whole neuron were captured by confocal microscope and assigned a random
853 number, and dendrites with length more than 50μm were selected by another blinded
854 experimenter for quantification. Dendritic spines were classified based on our
855 previous study (Lin et al., 2017). The length (L), head width (H) and neck width (N)
856 of each individual spine were measured manually using the MetaMorph software.
857 Mushroom spines were defined as those having H/N ≧1.5; stubby spines were
858 defined as those having H/N ≦1 and L/N ≦1; thin spines had the ratio of 1≦
859 H/N<1.5 and 1.5 ≦ L/N ≦3. Filopodia were defined as those with the ratio of H/N
860 <1.2 and L/N > 3. For each neuron, one to three dendrites were selected and
861 quantified, and the average spine density would be calculated. The “n” number is
862 defined as the number of neurons analyzed

863 For quantification of KIF5A-GFP and KIF5B-GFP puncta, images after maximal
864 projection of multiple z-layers were intensity-adjusted to the same minimum and

865 maximum values using FIJI software “Brightness/Contrast” function before manual
866 counting of puncta.

867 To quantify the localization of endogenous KIF5A and KIF5B by
868 immunostaining, images after maximal projection of z-layers were intensity-adjusted
869 to remove signals below the threshold, which is determined by the negative control
870 without primary antibody as reference). The spine density and percentage of
871 puncta-positive spines were quantified by manual counting.

872 For quantification of KIF5A and KIF5B knockdown efficiency by
873 immunofluorescence, areas of cell soma were outlined based on GFP signals on
874 images after maximal projection of multiple layers. The signal intensity of the target
875 protein within selected area was measured using FIJI software.

876 For quantification of FISH images, selected dendrites from maximal projected
877 images were straightened using “Straighten” (Kocsis et al., 1991) plug-in in FIJI. For
878 each channel of interest, a threshold was determined based on a negative control
879 image and the puncta information was extracted using “Analyze particle” function in
880 FIJI within the region of the dendrite (outlined based on GFP signals). For the
881 analysis of granule distribution along dendrites, the number of granules within each
882 bin (5μm) was determined for every dendrite, and the number in the first bin was

normalized as 1.

Immunohistochemistry, image acquisition, and quantitative analysis

For the analysis of dendritic spines in hippocampus *in vivo*, mouse brains were fixed at P44 and coronally sectioned at 50 μm on a vibratome (Leica). Confocal images of secondary dendrites from apical branches of CA1 hippocampal neurons and prefrontal cortex neurons were captured as described above. 3D reconstruction of individual dendrites was performed. The dendritic spine number was analyzed by Neuron Studio software.

For neuronal nuclei (NeuN), neurogranin (NRGN) and KIF5B staining, mouse brains were sacrificed at P44 and post-fixed with 4% paraformaldehyde. The samples were then sectioned to 50 μm per slice using vibratome. Brain sections were blocked with 1.5% normal goat serum (NGS) in PBST (0.3% Triton X-100) and incubated with a 1:1000 diluted primary antibody against KIF5B at 4°C overnight. Alexa 488-conjugated goat anti-rabbit IgG secondary antibody was used to probe the anti-KIF5B signals. Since both anti-KIF5B and anti-NRGN were from rabbit host, the sections were blocked again with 5% normal rabbit serum (NRS) in PBST(Wessel and McClay, 1986). Next, sections were incubated with 1:1000 anti-NRGN primary antibody overnight at 4°C. Another secondary antibody, goat anti-rabbit Alexa 546,

was used to probe anti-NRGN signals. For NeuN staining, brain sections were incubated with anti-NeuN antibody (1:1000) after blocking. Goat anti-mouse IgG Alexa 546 conjugate was used to probe the anti-NeuN signals. Imaging was carried out under LSM700 confocal microscope. Quantification of fluorescence images was performed using ImageJ software.

Behavioural tests

All behavioral tests were performed in the chronological order of open field test (OFT), elevated plus maze (EPM), marble burying test (MBT), 3-chamber social interaction (SI) and fear conditioning (FC). Barnes maze (BM), novel object recognition (NOR) and rotarod training were done in separate sets of animals.

Open field test (OFT). Mice were placed in the center of a square open field chamber (40 × 40 × 40 cm) surrounded by walls. Tracing was performed using ANY-maze software. The time of the mouse spent in the center area was measured over the course of 15 min (Shin Yim et al., 2017).

Elevated plus maze (EPM). Mice were placed in the center of a plus-shaped chamber that stands 38 cm above ground. Mice were then allowed to explore freely for 5 min. The duration of the mouse spent in either arm was recorded and tracked

using ANY-maze software (Walf and Frye, 2007).

Marble burying test (MBT). Mice were placed into testing arenas (arena size: 42.5 cm × 27.6 cm × 15.3 cm, bedding depth: 5 cm) each containing 20 glass marbles (laid out in four rows of five marbles equidistant from one another). At the end of the 30-min exploration period, mice were carefully removed from the testing cages and the number of marbles buried was recorded. The marble burying score was arbitrarily defined as the following: 4 for completely buried marbles, 3 for marbles covered >50% with bedding, 2 for marbles covered 50% with bedding, 1 for marbles covered <50% with bedding, or 0 for anything less. The final marble burying score for each mouse was the sum of the scores of the 20 marbles (Shin Yim et al., 2017).

Novel object recognition (NOR). Mice were placed into a training chamber (25cm x 25cm x 40cm) containing two identical objects. Mice were allowed to freely explore in the chamber for 10 min. In the recall session, mice were put back to the same chamber while one of the two identical objects were replaced with a novel object with different color and slightly different shape 14-16 hours after the training session. The movement of the mice was tracked with ANY-maze software for its interaction with both the familiar and novel objects. Discrimination index = interaction time with novel object / total interaction time with both objects (Leger et

al., 2013).

Three-chamber social interaction (SI). Two empty object-containment cages (shape of a cup with evenly spaced metallic bars) were each placed into the left and right chamber of a 3-chamber arena (20 cm × 42 cm × 26 cm). In the adaptation period, a mouse was shut within the center chamber for 5 min. In stage 1, a stranger mouse of same sex, similar age and size as the test mouse was put into the left cage. The test mouse in the center was released then to freely explore all of the 3 chambers for a 10 min period. After stage 1, the test mouse was shut within the center again when the experimenter put another stranger mouse to the right cage. At stage 2, the test mouse was allowed to explore all the 3 chambers again for 10 min. Approach behaviour within 2 cm with targets was defined as interaction time. Sessions were video-recorded. Approach behaviour and total distance travelled were analyzed using ANY-maze tracking system (Shin Yim et al., 2017).

Sociability index = (percentage time of interaction with stranger) - (percentage time of interaction with empty cage)/ percentage of interaction time with both objects

Social memory index = (percentage time of interaction with novel stranger) - (percentage time of interaction with familiar)/ percentage of interaction time with both strangers.

954 Auditory-cued fear conditioning (FC). FreezeFrame system (Coulbourn
955 Instruments) was used to train and test mice. For training, the chamber was equipped
956 with stainless-steel shocking grids, which were connecting to a precision feedback
957 current-regulated shocker. Each chamber was contained in a sound-attenuating
958 enclosure. Animal behaviour was recorded using low-light video cameras. Actimetrics
959 FreezeFrame software (version 2.2; Coulbourn Instruments) was used to control the
960 stimulus presentation by a preset program. All equipment was thoroughly cleaned
961 with water followed by ethanol between sessions to avoid residue of scents from
962 mouse feces and urine. Mice were habituated for 1 min on a shocking grid (cage
963 set-up A: shocking floor grids, ethanol scent). Fear conditioning was conducted with
964 three pairings of a 30-s, 4000-Hz, 80-dB auditory cue (CS) co-terminating with a 2-s,
965 0.5-mA scrambled footshock (US). The inter-trial interval was 20 s. One minute after
966 conditioning, mice were returned to their home cages. For the recall test, mice were
967 placed in a different context (cage set-up B: test floor grids, 1% lemon scent detergent)
968 for an initial 2-min (pre-tone) period and this was followed by tone presentation for
969 2 min (CS) (Lai et al., 2012).

970 Rotarod. An EZRod system (Omnitech Electronics, Inc.) was used as a motor
971 training model. Mice were placed on the motorized rod (30 mm in diameter) in the

chamber. The rotation speed gradually increased from 0 to 100 r.p.m. over the course of 3 min. Rotarod training was performed for 20 trials, each trial lasts until the subjects dropped and the system would automatically complete that trial (Deacon, 2013; Yang et al., 2014).

Barnes maze. Mice were placed on a white circular table (92 cm in diameter, 1m tall), which had a total of 20 holes (5 cm in diameter) separated evenly along the edge of the table. During the test, strong light with an intensity of 1500 lux and repetitive noise from metronome of 80 dB were given to serve as aversive stimuli to induce escape behaviour. On acquisition day, mice were first guided manually to the escape hole for adaptation purpose. Then, mice received 5 trials of training, with each separated from one another by 15 minutes. Each trial would last for 3 minutes. If mice were not able to find the target escape hole by the end of the each trial, mice will be guided to the target escape hole as a part of training. A 3-minute recall session was carried out 5 days after acquisition day. Mice were subjected to the same maze except the escape hole was also blocked. The number of errors and latency to reach the original escape hole were measured manually to confirm the result generated by ANY-maze. Heat maps were obtained by ANY-maze. (Sunyer et al., 2007).

In vivo transcranial two-photon imaging

Spine formation and elimination were examined in longitudinal studies by imaging the mouse cortex through a thinned-skull window as described previously (Lai et al., 2012; Yang et al., 2009). Briefly, one-month-old mice expressing YFP were anesthetized with ketamine/xylazine (i.p., 20 mg/ml, 3 mg/ml respectively in saline, 6 μl/g body weight). Thinned skull windows were made with high-speed microdrills in head-fixed mice. Skull thickness was reduced to about 20 μm. A two-photon microscope tuned to 920 nm (25x water immersion lens, N.A. 1.05) was used to acquire images. For re-imaging of the same region, thinned regions were identified based on the maps of the brain vasculature. Microsurgical blades were used to re-thin the region of interest until a clear image could be obtained. On the third imaging session, the skull above the imaging field was removed to allow clear image acquisition. The area of the imaging region is 216 μm × 216 μm. The center of imaging region is located at the frontal association cortex (+2.8 mm bregma, +1.0 mm midline). All data analysis was performed blind to treatment conditions. For imaging of dendritic spines, dendritic branches were randomly sampled within a 216 μm × 216 μm area imaged at 0-100 μm distance below the pia surface. The same dendritic segments were identified from three-dimensional image stacks taken at different time points with high image quality (ratio of signal to background noise > 4:1). The number and location of dendritic protrusions (protrusion lengths were more than

one-third of the dendritic shaft diameter) were identified. Filopodia were identified as long, thin structures (generally larger than twice the average spine length, ratio of head diameter to neck diameter < 1.2:1 and ratio of length to neck diameter > 3:1). The remaining protrusions were classified as spines (Ng et al, 2018; Lai et al, 2012). The percentage of spine formation and elimination represented the number of spines formed or eliminated between the first and second view divided by the total number of spines counted at the first view in each individual mouse. For dendrite image display, fluorescent structures near and out of the focal plane of the dendrites of interest were removed manually from image stacks using Adobe Photoshop. The modified image stacks were then projected to generate two-dimensional images and adjusted for contrast and brightness.

Statistical analysis

Data are represented as mean + SEM/SD in quantitative analysis. Statistical analysis was performed with Student's *t* test or One-way ANOVA followed by Tukey post-hoc test. If comparison was made across grouped data, Two-way ANOVA with Tukey post-hoc test was used. If dataset did not follow a normal distribution as detected by Shapiro-Wilk normality test, Mann-Whitney test or Kruskal-Wallis test with post-hoc Dunnett's multiple comparison test was used. Statistical significances

were defined as $p < 0.05$.

ACKNOWLEDGEMENTS

We are grateful to Quan Hao (University of Hong Kong) for the KIF5A and KIF5C expression constructs. We also thank Ka Ki Tam for the quantification of FMRP granule movement, the assistance of Kam Wing Kenny Ho (Chinese University of Hong Kong) on LTP recording of hippocampal slices, and the Imaging Core Facility from the Faculty of Medicine at the University of Hong Kong on image acquisition and analysis. This study was supported in part by the Research Grant Council of Hong Kong [General Research Fund (GRF) 16100814, 17135816, 17106018 and Early Career Scheme (ECS) 27119715] awarded to K.O.L; the Area of Excellence Scheme (Grant AoE/M-604/16) and Theme-based Research Scheme (Grant T13-605/18-W) of the University Grants Committee of Hong Kong awarded to K.O.L. and W.H.Y.; RGC/ECS 27103715 and RGC/GRF 17128816, National Natural Science Foundation of China (NSFC/General Program 31571031), and the Health and Medical Research Fund (HMRF) 03143096 awarded to C.S.W.L.; the Shenzhen Peacock Team Project (KQTD2015033117210153) and Shenzhen Science Technology Innovation Committee Basic Science Research Grant (JCYJ20170413154523577) awarded to J.H..

COMPETING INTERESTS

The authors declare that no competing interests exist.

REFERENCES:

Barry J, Gu Y, Jukkola P, O'Neill B, Gu H, Mohler PJ, Rajamani KT and Gu C. (2014). Ankyrin-G directly binds to kinesin-1 to transport voltage-gated Na+ channels into axons. Developmental cell *28*, 117-131.

Basso M, Pennuto M (2015). Serine phosphorylation and arginine methylation at the crossroads to neurodegeneration. Experimental neurology *271*, 77-83.

Bayes A, van de Lagemaat LN, Collins MO, Croning MD, Whittle IR, Choudhary JS, and Grant SG (2011). Characterization of the proteome, diseases and evolution of the human postsynaptic density. Nature Neuroscience *14*, 19-21.

Bedford MT, and Clarke SG (2009). Protein arginine methylation in mammals: who, what, and why. Molecular Cell *33*, 1-13.

Bermejo MK, Milenkovic M, Salahpour A, and Ramsey AJ (2014). Preparation of synaptic plasma membrane and postsynaptic density proteins using a discontinuous sucrose gradient. Journal of Visualized Experiments *91*, e51896.

Berry KP, and Nedivi E (2017). Spine dynamics: are they all the same?. Neuron *96*, 43-55.

Bourne JN, and Harris KM (2007). Do thin spines learn to be mushroom spines that remember? Current Opinion in Neurobiology *17*, 381-386.

Brady ST (1985). A novel brain ATPase with properties expected for the fast axonal transport motor. Nature *317*, 73-75.

Caballero A, Granberg R, and Tseng KY (2016). Mechanisms contributing to prefrontal cortex maturation during adolescence. Neurosci Biobehavior Review *70*, 4-12.

Campbell PD, Shen K, Sapio MR, Glenn TD, Talbot WS, and Marlow FL (2014). Unique function of Kinesin Kif5A in localization of mitochondria in axons. Journal of Neuroscience *34*, 14717-14732.

Charalambous DC, Pasciuto E, Mercaldo V, Pilo Boyl P, Munck S, Bagni C, and Santama N (2013). KIF1Bbeta transports dendritically localized mRNPs in neurons and is recruited to synapses in an activity-dependent manner. Cellular and Molecular Life Sciences *70*, 335-356.

Cho KI, Cai Y, Yi H, Yeh A, Aslanukov A, and Ferreira PA (2007). Association of the kinesin-binding domain of RanBP2 to KIF5B and KIF5C determines mitochondria localization and function. Traffic (Copenhagen, Denmark) 8, 1722-1735.

Comery TA, Harris JB, Willems PJ, Oostra BA, Irwin SA, Weiler IJ, and Greenough WT (1997). Abnormal dendritic spines in fragile X knockout mice: Maturation and

pruning deficits. Proceedings of the National Academy of Sciences *94*, 5401.
Cui J, Wang Z, Cheng Q, Lin R, Zhang XM, Leung PS, Copeland NG, Jenkins NA, Yao KM, and Huang JD (2011). Targeted inactivation of kinesin-1 in pancreatic beta-cells in vivo leads to insulin secretory deficiency. Diabetes *60*, 320-330.
Davidovic L, Jaglin XH, Lepagnol-Bestel AM, Tremblay S, Simonneau M, Bardoni B, and Khandjian EW (2007). The fragile X mental retardation protein is a molecular adaptor between the neurospecific KIF3C kinesin and dendritic RNA granules. Human Molecular Genetics *16*, 3047-3058.
Deacon RM (2013). Measuring motor coordination in mice. Journal of Visualized Experiments *75*, e2609.
Delanoue R, and Davis I (2005). Dynein Anchors Its mRNA Cargo after Apical Transport in the Drosophila Blastoderm Embryo. Cell *122*, 97-106.
Dictenberg JB, Swanger SA, Antar LN, Singer RH, and Bassell GJ (2008). A direct role for FMRP in activity-dependent dendritic mRNA transport links filopodial-spine morphogenesis to fragile X syndrome. Developmental Cell *14*, 926-939.
Doyle M, and Kiebler MA (2011). Mechanisms of dendritic mRNA transport and its role in synaptic tagging. The EMBO Journal *30*, 3540-3552.
Dragatsis I, and Zeitlin S (2000). CaMKIIalpha-Cre transgene expression and recombination patterns in the mouse brain. Genesis *26*, 133-135.
Fenelon K, Xu B, Lai CS, Mukai J, Markx S, Stark KL, Hsu PK, Gan WB, Fischbach GD, MacDermott AB, *et al.* (2013). The pattern of cortical dysfunction in a mouse model of a schizophrenia-related microdeletion. Journal of Neuroscience *33*, 14825-14839.
Fink JK (2013). Hereditary spastic paraplegia: clinico-pathologic features and emerging molecular mechanisms. Acta Neuropathologica *126*, 307-328.
Franker MA, Esteves da Silva M, Tas RP, Tortosa E, Cao Y, Frias CP, Janssen AFJ, Wulf PS, Kapitein LC, and Hoogenraad CC (2016). Three-Step Model for Polarized Sorting of KIF17 into Dendrites. Current Biology *26*, 1705-1712.
Friedman DS, and Vale RD (1999). Single-molecule analysis of kinesin motility reveals regulation by the cargo-binding tail domain. Nature Cell Biology *1*, 293-297.
Gogtay N, Giedd JN, Lusk L, Hayashi KM, Greenstein D, Vaituzis AC, Nugent TF, Nugent III, Herman DH, Clasen LS, Toga AW, *et al.* (2004). Dynamic mapping of human cortical development during childhood through early adulthood. Proceedings of the National Academy of Sciences *101*, 8174-8179.
Guillaud L, Wong R, and Hirokawa N (2008). Disruption of KIF17-Mint1 interaction

by CaMKII-dependent phosphorylation: a molecular model of kinesin-cargo release. Nature Cell Biology *10*, 19-29.

Gumy LF, Katrukha EA, Grigoriev I, Jaarsma D, Kapitein LC, Akhmanova A, and Hoogenraad CC (2017). MAP2 Defines a Pre-axonal Filtering Zone to Regulate KIF1- versus KIF5-Dependent Cargo Transport in Sensory Neurons. Neuron *94*, 347-362 e347.

Guo A, Gu H, Zhou J, Mulhern D, Wang Y, Lee KA, Yang V, Aguiar M, Kornhauser J, Jia X, *et al.* (2014). Immunoaffinity enrichment and mass spectrometry analysis of protein methylation. Molecular Cellular Proteomics *13*, 372-387.

Harris KM, Jensen FE, Tsao B (1992). Three-dimensional structure of dendritic spines and synapses in rat hippocampus (CA1) at postnatal day 15 and adult ages: implications for the maturation of synaptic physiology and long-term potentiation. The Jounral of Neuroscience *12*, 2685-2705.

Hatanaka Y, Watase K, Wada K, and Nagai Y (2015). Abnormalities in synaptic dynamics during development in a mouse model of spinocerebellar ataxia type 1. Scitific Report *5*, 16102.

Heisler FF, Lee HK, Gromova KV, Pechmann Y, Schurek B, Ruschkies L, Schroeder M, Schweizer M, and Kneussel M (2014). GRIP1 interlinks N-cadherin and AMPA receptors at vesicles to promote combined cargo transport into dendrites. Proceedings of the National Academy of Sciences *111*, 5030-5035.

Hirokawa N, Niwa S, and Tanaka Y (2010). Molecular motors in neurons: transport mechanisms and roles in brain function, development, and disease. Neuron *68*, 610-638.

Hirokawa N, and Tanaka Y (2015). Kinesin superfamily proteins (KIFs): Various functions and their relevance for important phenomena in life and diseases. Experimental Cell Research *334*, 16-25.

Hoerndli FJ, Maxfield DA, Brockie PJ, Mellem JE, Jensen E, Wang R, Madsen DM, and Maricq AV (2013). Kinesin-1 regulates synaptic strength by mediating the delivery, removal, and redistribution of AMPA receptors. Neuron 80, 1421-1437.

Holt CE, and Schuman EM (2013). The central dogma decentralized: new perspectives on RNA function and local translation in neurons. Neuron *80*, 648-657.

Huang CF, and Banker G (2012). The translocation selectivity of the kinesins that mediate neuronal organelle transport. Traffic *13*, 549-564.

Jaworski J, Kapitein LC, Gouveia SM, Dortland BR, Wulf, PS, Grigoriev I, Camera P, Spangler SA, Di Stefano P, Demmers J, et al. (2009). Dynamic microtubules regulate dendritic spine morphology and synaptic plasticity. Neuron 61, 85-100.

Kamal A, Stokin GB, Yang Z, Xia CH, and Goldstein LS (2000). Axonal transport of amyloid precursor protein is mediated by direct binding to the kinesin light chain subunit of kinesin-I. Neuron *28*, 449-459.

Kanai Y, Dohmae N, and Hirokawa N (2004). Kinesin transports RNA: isolation and characterization of an RNA-transporting granule. Neuron *43*, 513-525.

Kanai Y, Okada Y, Tanaka Y, Harada A, Terada S, and Hirokawa N (2000). KIF5C, a novel neuronal kinesin enriched in motor neurons. Journal of Neuroscience *20*, 6374-6384.

Kapitein LC, Schlager MA, van der Zwan WA, Wulf PS, Keijzer N, and Hoogenraad CC (2010). Probing intracellular motor protein activity using an inducible cargo trafficking assay. Biophysical Journal *99*, 2143-2152.

Kim CH, and Lisman JE (2001). A Labile Component of AMPA Receptor-Mediated Synaptic Transmission Is Dependent on Microtubule Motors, Actin, and N-Ethylmaleimide-Sensitive Factor. Journal of Neuroscience *21*, 4188.

Kocsis E, Trus BL, Steer CJ, Bisher ME, and Steven AC (1991). Image averaging of flexible fibrous macromolecules: the clathrin triskelion has an elastic proximal segment. Journal of Structural Biology *107*, 6-14.

Kuklin EA, Alkins S, Bakthavachalu B, Genco MC, Sudhakaran I, Raghavan KV, Ramaswami M, and Griffith LC (2017). The Long 3′UTR mRNA of CaMKII Is Essential for Translation-Dependent Plasticity of Spontaneous Release in Drosophila melanogaster. The Journal of Neuroscience *37*, 10554.

Lai CS, Franke TF, and Gan WB (2012). Opposite effects of fear conditioning and extinction on dendritic spine remodelling. Nature *483*, 87-91.

Lai KO, and Ip NY (2013). Structural plasticity of dendritic spines: the underlying mechanisms and its dysregulation in brain disorders. Biochimica et Biophysica Acta (BBA)-Molecular Basis of Disease *1832*, 2257-2263.

Lai KO, Zhao Y, Ch'ng TH, and Martin KC (2008). Importin-mediated retrograde transport of CREB2 from distal processes to the nucleus in neurons. Proceedings of the National Academy of Sciences *105*, 17175-17180.

Leger M, Quiedeville A, Bouet V, Haelewyn B, Boulouard M, Schumann-Bard P, and Freret T (2013). Object recognition test in mice. Nature Protocol *8*, 2531-2537.

Lin L, Lo LH, Lyu Q, and Lai KO (2017). Determination of dendritic spine morphology by the striatin scaffold protein STRN4 through interaction with the phosphatase PP2A. Journal of Biology Chemistry *292*, 9451-9464.

Lin R, Duan Z, Sun H, Fung ML, Chen H, Wang J, Lau CF, Yang D, Liu Y, Ni Y, et al. (2019). Kinesin-1 Regulates Extrasynaptic Targeting of NMDARs and Neuronal

Vulnerability Toward Excitotoxicity. iScience *13*, 82-97.
McKinney RA (2010). Excitatory amino acid involvement in dendritic spine formation, maintenance and remodelling. The Journal of Physiology *588*, 107-116.
McVicker DP, Awe AM, Richters KE, Wilson RL, Cowdrey DA, Hu X, Chapman ER, and Dent EW (2016). Transport of a kinesin-cargo pair along microtubules into dendritic spines undergoing synaptic plasticity. Nature Communication *7*, 12741.
Miki H, Setou M, Kaneshiro K, and Hirokawa N (2001). All kinesin superfamily protein, KIF, genes in mouse and human. Proceedings of the National Academy of Sciences *98*, 7004-7011.
Mitsumori K, Takei Y, and Hirokawa N (2017). Components of RNA granules affect their localization and dynamics in neuronal dendrites. Molecular Biology of the Cell *28*, 1412-1417.
Morfini G, Schmidt N, Weissmann C, Pigino G, and Kins S (2016). Conventional kinesin: Biochemical heterogeneity and functional implications in health and disease. Brain Research Bulletin *126*, 347-353.
Murmu RP, Li W, Holtmaat A, and Li JY (2013). Dendritic spine instability leads to progressive neocortical spine loss in a mouse model of Huntington's disease. Journal of Neuroscience *33*, 12997-13009.
Nagaoka A, Takehara H, Hayashi-Takagi A, Noguchi J, Ishii K, Shirai F, Yagishita S, Akagi T, Ichiki T, and Kasai H (2016). Abnormal intrinsic dynamics of dendritic spines in a fragile X syndrome mouse model in vivo. Scientific Report *6*, 26651.
Najbauer J, Johnson BA, Young AL, and Aswad DW (1993). Peptides with sequences similar to glycine, arginine-rich motifs in proteins interacting with RNA are efficiently recognized by methyltransferase(s) modifying arginine in numerous proteins. Journal of Biology Chemistry *268*, 10501-10509.
Nakajima K, Yin X, Takei Y, Seog DH, Homma N, and Hirokawa N (2012). Molecular motor KIF5A is essential for GABA(A) receptor transport, and KIF5A deletion causes epilepsy. Neuron *76*, 945-961.
Nakayama D, Baraki Z, Onoue K, Ikegaya Y, Matsuki N, and Nomura H (2015). Frontal association cortex is engaged in stimulus integration during associative learning. Current Biology *25*, 117-123.
Ng LHL, Huang Y, Han L, Chang RC, Chan YS, and Lai CSW (2018). Ketamine and selective activation of parvalbumin interneurons inhibit stress-induced dendritic spine elimination. Translational Psychiatry *8*, 272.
Pan F, Aldridge GM, Greenough WT, and Gan WB (2010). Dendritic spine instability and insensitivity to modulation by sensory experience in a mouse model of fragile X syndrome. Proceedings of the National Academy of Sciences *107*, 17768-17773.

Penney J, Seo J, Kritskiy O, Elmsaouri S, Gao F, Pao PC, Su SC, and Tsai LH (2017). Loss of Protein Arginine Methyltransferase 8 Alters Synapse Composition and Function, Resulting in Behavioral Defects. Journal of Neuroscience *37*, 8655-8666.

Rogerson T, Cai DJ, Frank A, Sano Y, Shobe J, Lopez-Aranda MF, and Silva AJ (2014). Synaptic tagging during memory allocation. Nature Review Neuroscience *15*, 157-169.

Sanders J, Cowansage K, Baumgärtel K, Mayford M (2012). Elimination of dendritic spines with long-term memory is specific to active circuits. Journal of Neurocience *32*, 12570-12578.

Scheetz AJ, Nairn AC, and Constantine-Paton M (2000). NMDA receptor-mediated control of protein synthesis at developing synapses. Nature Neuroscience *3*, 211-216.

Schratt GM, Nigh EA, Chen WG, Hu L, and Greenberg ME (2004). BDNF regulates the translation of a select group of mRNAs by a mammalian target of rapamycin-phosphatidylinositol 3-kinase-dependent pathway during neuronal development. Journal of Neuroscience *24*, 7366-7377.

Seiler S, Kirchner J, Horn C, Kallipolitou A, Woehlke G, and Schliwa M (2000). Cargo binding and regulatory sites in the tail of fungal conventional kinesin. Nature Cell Biology *2*, 333-338.

Setou M, Seog DH, Tanaka Y, Kanai Y, Takei Y, Kawagishi M, and Hirokawa N (2002). Glutamate-receptor-interacting protein GRIP1 directly steers kinesin to dendrites. Nature *417*, 83-87.

Shin Yim Y, Park A, Berrios J, Lafourcade M, Pascual LM, Soares N, Yeon Kim J, Kim S, Kim H, Waisman A, *et al.* (2017). Reversing behavioural abnormalities in mice exposed to maternal inflammation. Nature *549*, 482-487.

Silverman MA, Kaech S, Ramser EM, Lu X, Lasarev MR, Nagalla S, and Banker G (2010). Expression of kinesin superfamily genes in cultured hippocampal neurons. Cytoskeleton *67*, 784-795.

Song AH, Wang D, Chen G, Li Y, Luo J, Duan S, and Poo MM (2009). A selective filter for cytoplasmic transport at the axon initial segment. Cell *136*, 1148-1160.

Spiga S, Talani G, Mulas G, Licheri V, Fois GR, Muggironi G, Masala N, Cannizzaro C, Biggio G, Sanna E, Diana M (2014). Hampered long-term depression and thin spine loss in the nucleus accumbens of ethanol-dependent rats. Proceedings of the National Academy of Sciences *111*, E3745-3754.

Sunyer B, Patil S, Hoger H, and Gert L (2007). Barnes maze, a useful task to assess spatial reference memory in the mice. Protocol Exchange.

Tanaka Y, Kanai Y, Okada Y, Nonaka S, Takeda S, Harada A, and Hirokawa N (1998).

Targeted disruption of mouse conventional kinesin heavy chain, kif5B, results in abnormal perinuclear clustering of mitochondria. Cell *93*, 1147-1158.

Tas RP, Chazeau A, Cloin BMC, Lambers MLA, Hoogenraad CC, and Kapitein LC (2017). Differentiation between Oppositely Oriented Microtubules Controls Polarized Neuronal Transport. Neuron *96*, 1264-1271 e1265.

Toda H, Mochizuki H, Flores R 3rd, Josowitz R, Krasieva TB, Lamorte VJ, Suzuki E, Gindhart JG, Furukubo-Tokunaga K, and Tomoda T (2008). UNC-51/ATG1 kinase regulates axonal transport by mediating motor-cargo assembly. Genes&Development *22*, 3292-3307.

Trachtenberg JT, Chen BE, Knott GW, Feng G, Sanes JR, Welker E, and Svoboda K (2002). Long-term in vivo imaging of experience-dependent synaptic plasticity in adult cortex. Nature *420*, 788-794.

Tsien JZ, Chen DF, Gerber D, Tom C, Mercer EH, Anderson DJ, Mayford M, Kandel ER, and Tonegawa S (1996). Subregion- and cell type-restricted gene knockout in mouse brain. Cell *87*, 1317-1326.

Twelvetrees AE, Yuen EY, Arancibia-Carcamo IL, MacAskill AF, Rostaing P, Lumb MJ, Humbert S, Triller A, Saudou F, Yan Z, *et al.* (2010). Delivery of GABAARs to synapses is mediated by HAP1-KIF5 and disrupted by mutant huntingtin. Neuron *65*, 53-65.

Vale RD, Reese TS, and Sheetz MP (1985). Identification of a novel force-generating protein, kinesin, involved in microtubule-based motility. Cell *42*, 39-50.

Walf AA, and Frye CA (2007). The use of the elevated plus maze as an assay of anxiety-related behavior in rodents. Nature Protocol *2*, 322-328.

Wessel GM, and McClay DR (1986). Two embryonic, tissue-specific molecules identified by a double-label immunofluorescence technique for monoclonal antibodies. Journal of Histochemistry & Cytochemistry *34*, 703-706.

Williams JM, Guévremont D, Mason-Parker SE, Luxmanan C, Tate WP, and Abraham WC (2007). Differential Trafficking of AMPA and NMDA Receptors during Long-Term Potentiation in Awake Adult Animals. The Journal of Neuroscience *27*, 14171.

Xu M, Gu Y, Barry J, and Gu C (2010). Kinesin I transports tetramerized Kv3 channels through the axon initial segment via direct binding. Journal of Neuroscience 30, 15987-16001.

Yang CY, Chiu LL, Chang CC, Chuang HC, and Tan TH (2018). Induction of DUSP14 ubiquitination by PRMT5-mediated arginine methylation. The FASEB Journal *32*, 6760-6770.

Yang G, Lai CS, Cichon J, Ma L, Li W, and Gan WB (2014). Sleep promotes

branch-specific formation of dendritic spines after learning. Science *344*, 1173-1178.

Yang G, Pan F, and Gan WB (2009). Stably maintained dendritic spines are associated with lifelong memories. Nature *462*, 920-924.

Yin X, Takei Y, Kido MA, and Hirokawa N (2011). Molecular motor KIF17 is fundamental for memory and learning via differential support of synaptic NR2A/2B levels. Neuron *70*, 310-325.

Ziv NE and Smith SJ (1996). Evidence for a role of dendritic filopodia in synaptogenesis and spine formation. Neuron *17*, 91-102.

Zuo Y, Lin A, Chang P, and Gan WB (2005). Development of long-term dendritic spine stability in diverse regions of cerebral cortex. Neuron *46*, 181-189.

FIGURE LEGEND

Figure 1. Different roles of KIF5s on dendritic spine morphogenesis and synaptic function.

(A) Western blot showing the developmental expression of different Kinesin I motors in the mouse hippocampus. The expression of all three KIF5s significantly decreased at later postnatal stages as compared to postnatal day 1 (P1); three independent experiments, mean + SEM; *p < 0.05; **p < 0.01; Two way ANOVA with Dunnett's multiple comparisons test. (B) Presence of all three KIF5s in the synaptic plasma membrane (SPM). Postsynaptic density-95 (PSD-95) served as the positive control for the SPM fraction. (C) Whole-cell patch recording was performed on hippocampal neuron upon individually knocking down KIF5A, KIF5B or KIF5C with short hairpin RNAs (shRNAs). Representative traces of miniature excitatory postsynaptic currents (mEPSCs) were shown. KIF5B knockdown led to significant decrease in mEPSC frequency compared to control. KIF5A knock-down significantly increased mEPSC amplitude compared to control (n = 10-13 neurons for each condition from five independent experiments; mean + SEM; *p < 0.05; **p < 0.01; Kruskal-Wallis test). (D) Representative images of dissociated rat hippocampal neurons co-transfected with GFP and the shRNA targeting individual KIF5 or a control shRNA. Neurons were

transfected at days *in vitro* (DIV) 13, and fixed and stained by GFP antibody at DIV 16. Knockdown of KIF5B significantly reduced the density of mushroom spines and led to a significant increase in the number of filopodia, thin and stubby spines. Knockdown of KIF5C significantly decreased the number of mushroom and thin spines (42-55 neurons of each group from three independent experiments were quantified; mean + SEM; * $p < 0.05$, ** $p < 0.01$, *** $p < 0.001$, **** $p < 0.0001$; Kruskal-Wallis test).

The following figure supplement is available for figure 1:

Figure 1-figure supplement 1. Validation of the knockdown efficiency and specificity of different shRNAs targeting KIF5.

(A) For western blot analysis, cortical neurons were transfected with the different shRNAs by nucleofection. At DIV 5, lysate was collected for Western blotting with antibody that specifically recognized each KIF5 homolog (three independent experiments; mean + SEM; multiple t-test with the Holm-Sidak method, alpha: 0.05). (B) For immunofluorescent staining analysis, different shRNAs were transfected into hippocampal neurons at 11DIV for 6 days and the soma intensity for the corresponding KIF5 homolog was analyzed. 9 or 11 neurons of each group were quantified. Data are presented in mean + SEM; * $p < 0.05$; Student's t-test.

Figure 2. Non-redundant roles of KIF5A and KIF5B on dendritic spine morphogenesis.

(A) Representative images of dissociated rat hippocampal neurons co-transfected with GFP and KIF5B-shRNA with/ without KIF5B or KIF5A construct. Co-expression of KIF5B rescued the loss of mushroom spines induced by KIF5B-shRNA, while KIF5A expression failed to reverse the spine phenotypes (42-51 neurons of each group from three independent experiments were quantified; mean + SEM; *** $p < 0.001$, **** $p < 0.0001$; Kruskal-Wallis test). (B) Representative images of dissociated rat hippocampal neurons co-transfected with GFP and KIF5B-shRNA with/ without KIF5B or KIF5C construct. Co-expression of KIF5C rescued the loss of mushroom spines induced by KIF5B-shRNA (34-46 neurons of each group from four independent experiments were quantified; mean + SEM; ** $p < 0.01$, **** $p < 0.0001$; Kruskal-Wallis test).

The following figure supplement is available for figure 2:

Figure 2-figure supplement 1. Subcellular localization of KIF5A and KIF5B in hippocampal neurons.

(A) Dissociated hippocampal neurons were transfected with tdTomato and equal amounts of either KIF5A-GFP or KIF5B-GFP. Greyscale images for individual channels, 2-channel merged images (blue for tdTomato and yellow for KIF5-GFP), as well as “royal” (ImageJ) colormap display of KIF5-GFP channel were shown for representative cells and dendrites. Both KIF5A and KIF5B puncta were present in the heads of dendritic spines (arrowheads). (B) Dissociated hippocampal neurons labeled with GFP were immunostained with specific antibodies against KIF5A or KIF5B. Images were displayed in a similar manner, except that GFP was displayed in blue and KIF5 signals were displayed in yellow in merge-channel images. KIF5A and KIF5B puncta were detected in the heads of dendritic spines (arrowheads). (C) Quatification for (A). The densities of spine and the percentage of spines with detected puncta were quantified by manual counting. 27 neurons were quantified for each group. Data are presented in mean + SEM, Student’s t-test. (D) Quatification for (B).The densities of spine and the percentage of spines with detected puncta were quantified by manual counting. 33 neurons were analyzed for KIF5A and 29 neurons were analyzed for KIF5B. Data are presented in mean + SEM; *** $p < 0.001$, **** $p< 0.0001$, Mann-Whitney test.

Figure 3. KIF5A and KIF5B differentially regulate the dendritic transport of FMRP and mRNA cargoes.

(A) Schematic diagram of the motor, stalk and tail domains of KIF5A, KIF5B and KIF5C, with the corresponding amino-acid positions indicated. The diverse carboxyl-termini within the tail domains were colored. (B) Pull-down of proteins from brain homogenate by GST-tagged KIF5s. FMRP was preferentially pull-downed from the brain lysate by KIF5B and KIF5C, but not KIF5A. (C) Representative dendrites and kymographs of GFP-FMRP granules from each group of neurons transfected with control shRNA, KIF5A-shRNA or KIF5B-shRNA. Different types of movements were traced manually and displayed in different colors (Stat: stationary; Osc: oscillatory; Bi: bidirectional; Antero: anterograde; Retro: retrograde.). Live imaging was conducted at 1 frame per second for 100 seconds. (D) Quantification of the densities of granules showing each category of movement. 17–19 neurons were quantified for each experimental condition. Results were pooled from three independent experiments; mean + SEM; *p < 0.05, **p < 0.01, ***p < 0.001, ****p < 0.0001, one-way ANOVA, Tukey's multiple comparisons test for total, stationary, oscillatory and anterograde granules; Kruskal-Wallis, Dunn's multiple comparisons test for bidirectional and retrograde granules. (E) Left: representative FISH images of

CaMKIIα and Grin2b mRNA puncta along dendrites. Hybridization with the sense probe served as negative control for the *in situ* hybridization. Middle: distribution of puncta number along dendrites (1 bin = 5μm) from cell body. 12-18 neurons were quantified for Grin2b mRNA and 11-20 neurons were quantified for CaMKIIα mRNA; mean + SEM; *p < 0.05, two-way ANOVA, Tukey's multiple comparisons test. Right: quantification of granule density. 12-22 neurons were quantified for CaMKIIα mRNA analysis; mean + SEM; **p < 0.01, one-way ANOVA, Tukey's multiple comparisons test. 13-20 neurons were quantified for Grin2b mRNA; mean + SEM; *p < 0.05, one-way ANOVA, Kruskal-Wallis test. Results were pooled from three independent experiments.

Figure 3-figure supplement 1. Quantification of GFP-FMRP granule motility and percentage of movements after knockdown of KIF5A or KIF5B.

(A) Demonstration of GFP-FMRP granule quantification using kymograph tracing. Different types of movements were traced manually and displayed in different colors. (Stat: stationary; Osc: oscillatory; Bi: bidirectional; Antero: anterograde; Retro: retrograde.) Live imaging was conducted at 1 frame per second for 100 seconds. (B) The travel distance, net displacement, maximal run length and maximal velocity were analyzed for each unidirectional and bidirectional granule. 305, 462 and 242 granules

from neurons transfected with control shRNA, KIF5A-shRNA, and KIF5B-shRNA were quantified, respectively. Data are presented in mean + SEM, Kruskal-Wallis, Dunn's multiple comparisons test. (C) The percentage of each type of granule movement were quantified. 1571, 1467 and 918 granules from neurons transfected with control shRNA, KIF5A-shRNA, and KIF5B-shRNA were quantified, respectively. The percentage of motile granules was increased after knockdown of KIF5A or KIF5B, while the motility of unidirectional and bidirectional granules was not affected.

Figure 4. Carboxyl-terminus determines the functional specificity of KIF5A and KIF5B in dendritic spine morphogenesis.

(A) Schematic diagram of the different constructs for pull-down assay (left panel). FMRP and G3BP1 were pulled-down from the SNS by either the truncated KIF5A lacking the 88 amino acids at the carboxyl-terminus, or chimeric KIF5A/B in which the carboxyl-terminus was substituted by that of KIF5B (right panel). (B) Representative images of dissociated rat hippocampal neurons co-transfected with GFP and KIF5B-shRNA with/ without KIF5B, KIF5A or chimeric KIF5A/B containing the carboxyl-terminus of KIF5B (1-938 KIF5A+941-963 KIF5B).

Co-expression of chimeric KIF5A/B rescued the loss of mushroom spines induced by KIF5B-shRNA (32-37 neurons of each group from three independent experiments were quantified; mean + SEM; *** $p < 0.001$, **** $p < 0.0001$; Kruskal-Wallis test).

Figure 5. Mono-methylation of arginine near carboxyl-terminus of KIF5B is required for the formation of mushroom spines.

(A) Amino acid alignment of the carboxyl-termini of KIF5A, KIF5B and KIF5C. Two conserved arginine residues (R941 and R956) in KIF5B across different vertebrates were highlighted by red boxes. (B) Carboxyl-terminal portions of different KIF5s were expressed in 293T cells. After immunoprecipitation with anti-FLAG beads, proteins were immunoblotted by antibody targeting mono-arginine methylation at glycine-rich motifs [MMA (R*GG)]. Transfection with pcDNA3 (vector) served as negative control. Only KIF5B and KIF5C but not KIF5A were arginine-methylated. (C) Methylation of KIF5B in the synaptoneurosome. Proteins were immunoprecipitated with anti-Mono-Methyl-Arginine antibody (MMA) and immunoblotted with KIF5B antibody (upper panel). Reciprocal immunoprecipitation using KIF5B antibody was performed to verify the arginine methylation pattern. (lower panel). (D) Methylation-deficient mutants of KIF5B were constructed by

single or double substitution of the two arginine residues to histidine. Vector and FLAG-tagged KIF5B constructs were transfected into 293T cells. After immunoprecipitation with anti-FLAG beads, proteins were immunoblotted by antibody targeting mono-arginine methylation at glycine-rich motifs [MMA (R*GG)]. Mono-methylation of KIF5B was abolished by substitution of both arginine sites by histidine (R941H/R956H). (E) Reduced amount of FMRP and G3BP1 was pulled down by methylation-deficient (R941/956H) mutant of KIF5B (five independent experiments for FMRP and three independent experiments for G3BP1; mean + SEM; **p < 0.01; ***p < 0.001; Student's *t*-test). (F) Representative images of dissociated rat hippocampal neurons co-transfected with GFP and KIF5B-shRNA together with either RNAi-resistant wild-type or the methylation-deficient (R941/956H) KIF5B construct. Co-expression of wild-type but not the methylation-deficient mutant KIF5B rescued the loss of mushroom spines induced by the KIF5B-shRNA (35-38 neurons of each group from three independent experiments were quantified; mean + SEM; **p < 0.01, *** p < 0.001, **** p < 0.0001; Kruskal-Wallis test). (G) Representative traces of mEPSCs of KIF5B-shRNA co-expressed with RNAi-resistant wild-type or the methylation-deficient (R941/956H) KIF5B construct were shown. Co-expression of wild-type KIF5B, but not methylation-deficient KIF5B, reversed the reduction of mEPSC frequency caused by KIF5B knock-down (13-14 neurons from five

independent experiments were quantified for each experimental condition; mean + SEM; **p < 0.01; Kruskal-Wallis test).

Figure 6. Targeting of *Kif5b* gene in *CaMKII-Cre/Kif5b*$^{fl/fl}$ mice and validation of the conditional knockout mice.

(A) Scheme of KIF5B knockout strategy (left panel). The blue rectangles (E1, E2, E3, E4, and E5) annotated exon 1, exon 2, exon 3, exon 4, and exon 5 of the *Kif5b* gene, respectively. The white rectangle with black bars on each side (each bar representing a flippase recognition target site) represented the 1.7-kb frt-NeoR-frt cassette. The red rectangles represent the LoxP sites (drawing not to scale). The green arrowheads indicated the designated annealing positions of genotyping PCR primers. Genotyping analysis of PCR product from mice DNA with different genotypes of the *Kif5b* gene (right panel). Cre primers were used to detect Cre recombinase gene. Primers P1 and P3 were used to identify *Kif5b*$^{fl/+}$ and *Kif5b*$^{fl/fl}$ genotypes. Primers P1 and P2 were used to identify *Kif5b* conditional knockout, *Kif5b*$^{-/-}$ genotype. (B) Western blot analysis probed with anti-KIF5A, anti-KIF5B, anti-KIF5C and anti-β-actin antibodies. Quantification result in the right panel was presented as the relative fold change compared to wild-type (WT). n = 6 for all groups for the analysis of KIF5B. n = 3 for

the analysis of other protein targets. Data were presented in mean + SEM. **p < 0.01, One-way ANOVA with post hoc Tukey's HSD. (C) Immunohistochemical staining of sagittal brain sections showed a significant reduction of cells that were both positive for KIF5B and Neurogranin (NRGN) in frontal area on postnatal day (P) 42±1. White traces highlighted NRGN-positive cells. Yellow traces indicated cells that were positive for both NRGN and KIF5B. Yellow and white squares indicate the zoom-in areas of $NRGN^{+}/KIF5B^{+}$ cells and $NRGN^{+}/KIF5B^{-}$ cells, respectively. Scale bar, 50μm and 25μm in magnified inserts. Right panel: quantification of KIF5B knockout in immunohistochemical staining of frontal area. n = 3 for WT. n = 3 for Homo. Data were presented in mean + SEM. **p < 0.01, Student's *t*-test with Welch's correction.

The following figure supplement is available for figure 6:

Figure 6-figure supplement 1. KIF5B conditional knockout mice show normal general appearance and cortical layer architecture.

(A) Representative images of 7-week-old male WT and Homo mice. (B) Representative images of 7-week old WT and Homo mouse brains. Scale bar, 1 cm. (C-D) Immunohistochemical staining of NeuN-positive cells in coronal sections of

WT and Homo mouse brains. The cortex was arbitrarily defined into bin layers parallel to the pia surface. Each bin layer had a thickness of 100 μm and the number of NeuN-positive cells within each layer was counted. Images of the frontal association (C) and the primary somatosensory (D) cortices were analyzed and the quantification result was shown in the lower panel. Bin size, 100 μm. Scale bar, 100 μm. n = 3 for WT and Homo. Data are presented in mean + SEM, multiple t-test with false discovery rate approach (FDR, Benjamin, Krieger, yekutieli), Q=1%

Figure 6-figure supplement 2. KIF5B conditional knockout mice show no change in KIF17 expression.

Western blot analysis and quantification of KIF17 expression in total brain lysates of homozygous KIF5B conditional knockout mice (Hom) compared with control littermates (WT). n = 3 for WT. n = 3 for Homo. Data are presented in mean + SEM. *p < 0.05, Mann-Whitney test.)

Figure 7. KIF5B conditional knockout mice show increase of dendritic spine instability in the frontal association cortex.

(A) Hippocampal and frontal association cortex slices of *Thy1*-YFP;*CaMKIIα*-Cre conditional *Kif5b*$^{fl/fl}$ knockout mice (Homo) and *Thy1*-YFP;*Kif5b* wild-type mice (WT) at postnatal day (P) 44 were fixed. Confocal images of secondary dendrites from apical branches of CA1 hippocampal neurons and prefrontal cortex neurons were captured. 3D reconstruction of individual dendrites was performed for quantification. Representative image of a hippocampal dendrite after 3D reconstruction was shown. (B) The density of dendritic spines in the homozygous KIF5B conditional knockout mice was significantly reduced in CA1 hippocampus as compared to the WT mice (23 dendrites from 2 WT mice and 22 dendrites from 2 homo mice; mean + SEM; *** $p < 0.001$; Mann-Whitney test). (C) No change in spine density was observed for neurons in the frontal association cortex (22 dendrites from 2 WT mice and 21 dendrites from 2 homo mice; mean + SEM; not significant; Mann-Whitney test). (D) Representative traces for mEPSCs on CA1 hippocampal neurons from WT and the homozygous KIF5B conditional knockout mice. The frequency and amplitude of mEPSCs from KIF5B conditional knockout neurons showed a significant reduction compared to WT neurons (10 neurons from 3 mice for each group; mean + SEM; *$p < 0.05$; Student's *t*-test for mEPSC amplitude, Mann-Whitney test for mEPSC frequency). (E) Experimental timeline and the diagram of a coronal section of frontal association cortex (FrA) showing the imaging site (green bar). (F) Representative images of

dendrites of *Thy1*-YFP/WT, *Thy1*-YFP/Hetero and *Thy1*-YFP/Homo at the imaging time point of Day 0, Day 2, and Day 7. Scale bars, 5 μm. Arrows mark spine formation compared to the previous time point. Arrowheads mark spine elimination compared to the previous time point. Red dots mark re-formation of previously eliminated dendritic spines in close proximity. Asterisks mark filopodia. (G-J) Quantification of spine elimination and formation rates from (G) Day 0- Day 2, (H) Day 2- Day 7, (I) total turnover rate and (J) re-formation of eliminated dendritic spines in close proximity on Day 7. n = 6, 947 dendritic spines for WT; n = 6, 906 dendritic spines for Hetero; n = 6, 1078 dendritic spines for Homo. Data were presented in mean + SD. *p < 0.05. **p < 0.01. ***p < 0.001, One-way ANOVA for G-J, except formation in G, day 2-7 turnover rate in I used Kruskal-Wallis test.

The following figure supplement is available for figure 7:

Figure 7-figure supplement 1. KIF5B conditional knockout mice show no significant difference in survival rate of newly formed dendritic spines.

Survival rate of newly formed dendritic spines. The number of dendritic spines newly formed on Day 2 that persisted to Day 7 was counted as stable new spines. The

stability percentage was the number of such spines divided by the total number of dendritic spines that were formed on Day 2. n = 6 for WT, Hetero, and Homo. Data are presented in mean + SEM, Kruskal-Wallis test.

Figure 8. KIF5B conditional knockout mice show deficits in synaptic plasticity, learning and memory.

(A) Schematic diagram shows the set-up of three-chamber social interaction test and the quantification of social memory index in the right panel. n = 10 for WT. n = 11 for Hetero and Homo. Data were presented in mean + SEM. *p < 0.05. (B) Schematic diagram shows the set-up of novel object recognition test and the quantification of discrimination index during recall phase in the right panel. n = 11 for WT. n = 12 for Hetero. n = 12 for Homo. Data were presented in mean + SEM. *p < 0.05. (C) Schematic diagram shows the set-up of fear conditioning and the quantification of freezing time before and during the recall tone was played in the right panel. n = 12 for WT. n = 11 for Hetero. n = 11 for Homo. Data were presented in mean + SEM. *p < 0.05, **p < 0.01, ****p < 0.0001, n.s.: not significant, Two Way ANOVA with post hoc Tukey's multiple comparison test. (D) Schematic diagram shows the set-up of Barnes maze. Quantification of primary latency during recall on 5 days after training.

n = 11 for WT. n = 13 for Homo. Data were presented in mean + SEM. *p <0.05, Mann-Whitney test. (E) Hippocampal LTP was reduced in KIF5B homozygous conditional knockout mice as shown by the reduced field EPSP amplitude (5 mice, 18 slices) compared with wild-type (6 mice, 22 slices).***p < 0.001, mean + SEM, Student's *t*-test. (F) Input/output and (G) pair-pulse ratio curves from hippocampal slices of WT (3 mice, 11 slices) and KIF5B homozygous conditional knockout mice (4 mice, 21 slices). No significant difference between WT and Homo, two-way ANOVA.

The following figure supplements are available for figure 8:

Figure 8-figure supplement 1. KIF5B conditional knockout mice showed no significant abnormalities in anxiety-related behavior tests.

(A) Schematic diagram shows the experimental set-up of open field test and the quantification of time spent in center area and the total distance travelled. n = 11 for WT. n = 12 for Hetero and Homo. Data are presented in mean + SEM, One-way ANOVA and Kruskal-Wallis test. (B) Schematic diagram shows the experimental set-up of elevated plus maze and the quantification of the time spent in open arm. n = 11 for WT. n = 12 for Hetero and Homo. Data are presented in mean + SEM, Kruskal-Wallis test. (C) Schematic diagram shows the experimental set-up of marble

burying test and the quantification of marble burying. n = 7 for WT. n = 5 for Hetero. n = 9 for Homo. Data are presented in mean + SEM, One-way ANOVA. (D) Schematic diagram shows the experimental set-up of rotarod and the quantification of performance of mice in seven days of rotarod training. Performance is represented in the highest speed (rate per minute, r.p.m.) the mice achieved before they fell from the rotarod. n = 5 for WT. n = 2 for Hetero. n = 7 for Homo. Data are presented in mean + SEM, Two-way ANOVA.

Figure 8-figure supplement 2. Sociability, fear acquisition, and primary error of Barnes maze in KIF5B conditional knockout mice.

(A) Quantification of animal behavior in stage 1 of social interaction test. The left panel is the quantification of the total interaction time of mice with either object in stage 1 of the three-chamber social interaction test. n = 10 for WT. n = 11 for Hetero and Homo. Data are presented in mean + SEM, One-way ANOVA. The middle panel is the quantification of interaction time of mice with either the inanimate object or the social object (mouse 1) during stage 1 of three-chamber social interaction test. ****p <0.0001. Two-way ANOVA. The right panel shows the quantification of sociability index, which is the ratio of the difference between the interaction time of the social

object and the inanimate object to the total interaction time of stage 1. n = 10 for WT. n = 11 for Hetero and Homo. Data are presented in mean + SEM. **p <0.01. One-way ANOVA with post hoc Tukey's HSD. (B) Quantification of animal behavior in stage 2 of social interaction test. The left panel is the quantification of the total interaction time of mice with either object in stage 2 of the three-chamber social interaction test. n = 10 for WT. n = 11 for Hetero and Homo. Data are presented in mean + SEM, Kruskal-Wallis test. The right panel is the quantification of interaction time of mice with either the novel social object (mouse 2) or the familiar social object (mouse 1) during stage 2 of three-chamber social interaction test. n = 10 for WT. n = 11 for Hetero and Homo. Data are presented in mean + SEM. **p < 0.01. ****p < 0.0001, Two-way ANOVA with post hoc Tukey's HSD. (C) Quantification of freezing time during acquisition stage of fear conditioning. The percentage of freezing of every 25 seconds interval are quantified and plotted along the time of fear conditioning. The appearance of conditioned stimulus (tone) and unconditioned stimulus (foot shock) is indicated. n = 12 for WT. n = 11 for Hetero. n=11 for Homo. Data are presented in mean + SEM, Two-way ANOVA with post hoc Tukey's HSD. #p < 0.05, comparison between WT and Hetero; **p < 0.01, comparison between WT and Homo. (D) Left panel showing heat map showing the percentage of time the representative mouse of each genotype spent on the maze during acquisition phase. Black circles indicate

non-target holes and white circles accompanied with asterisks indicate the target escape holes. WT mouse explored more non-target holes with higher number of primary error in the initial few trials, while Homo mouse stayed in the non-target hole with lower number of primary error during the acquisition phase. Middle panel showing quantification of primary error during acquisition phase and quantification of primary error on day 5 during recall in the right panel. (n= 11 for WT, n = 13 for Homo) Data are presented in mean + SEM. *$p < 0.05$, Two-way ANOVA with post hoc Tukey's multiple comparison test.

Figure 1

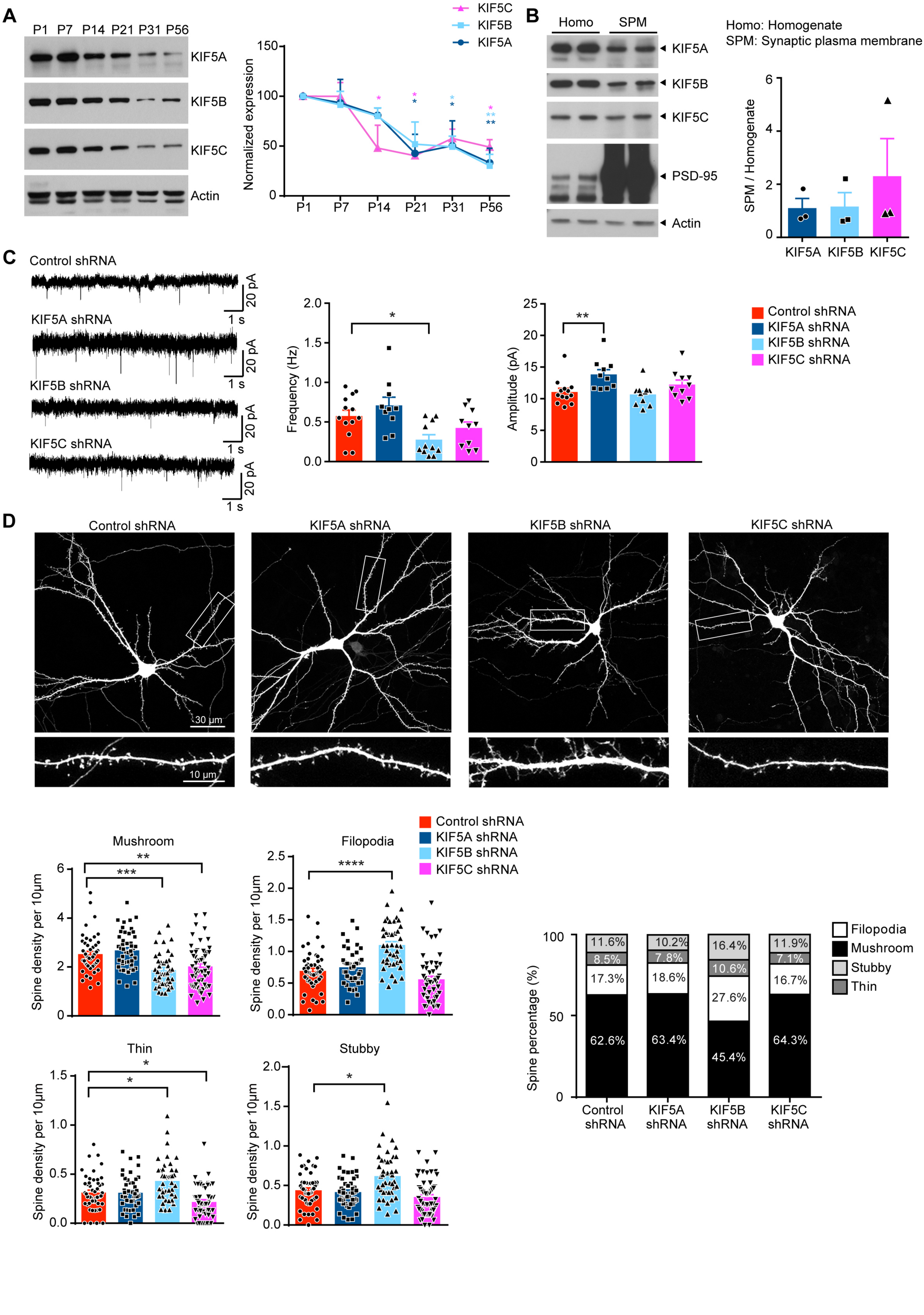
A
P1 P7 P14 P21 P31 P56
KIF5A
KIF5B
KIF5C
Actin
KIF5C
KIF5B
KIF5A
Normalized expression
150
100
50
0
P1 P7 P14 P21 P31 P56
B
Homo SPM
KIF5A
KIF5B
KIF5C
PSD-95
Actin
Homo: Homogenate
SPM: Synaptic plasma membrane
SPM / Homogenate
6
4
2
0
KIF5A KIF5B KIF5C
C
Control shRNA
KIF5A shRNA
KIF5B shRNA
KIF5C shRNA
20 pA
1 s
Frequency (Hz)
2.0
1.5
1.0
0.5
0.0
Amplitude (pA)
25
20
15
10
5
0
Control shRNA
KIF5A shRNA
KIF5B shRNA
KIF5C shRNA
D
Control shRNA
KIF5A shRNA
KIF5B shRNA
KIF5C shRNA
30 μm
10 μm
Mushroom
Filopodia
Thin
Stubby
Spine density per 10μm
Control shRNA
KIF5A shRNA
KIF5B shRNA
KIF5C shRNA
Spine percentage (%)
100
50
0
11.6%
8.5%
17.3%
62.6%
10.2%
7.8%
18.6%
63.4%
16.4%
10.6%
27.6%
45.4%
11.9%
7.1%
16.7%
64.3%
Filopodia
Mushroom
Stubby
Thin
Control shRNA
KIF5A shRNA
KIF5B shRNA
KIF5C shRNA

Figure 2

A

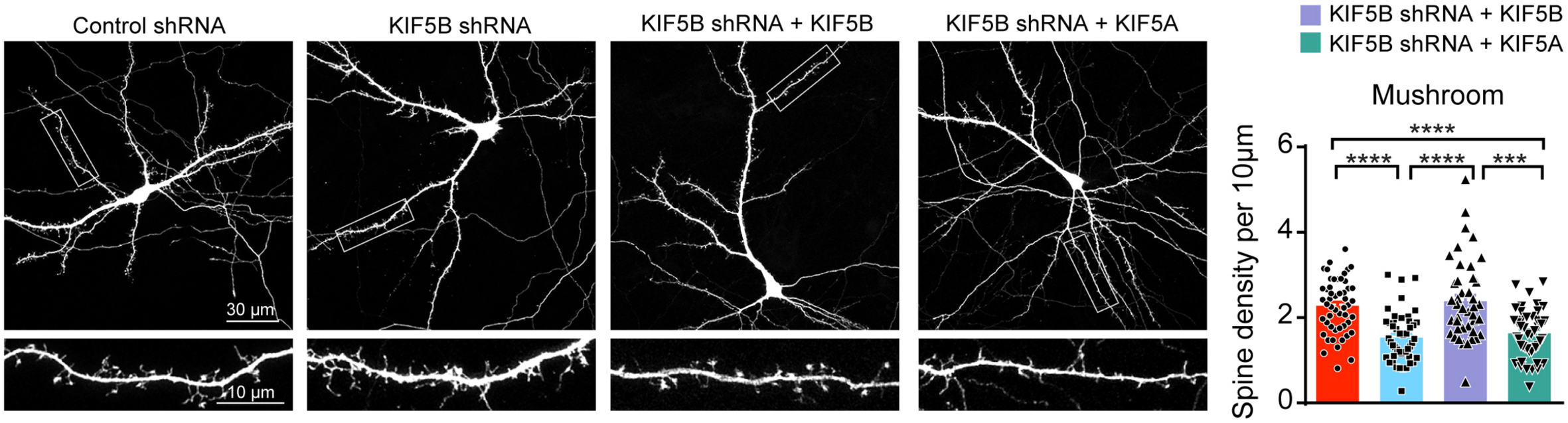
Control shRNA
KIF5B shRNA
KIF5B shRNA + KIF5B
KIF5B shRNA + KIF5A
30 μm
10 μm
Control shRNA
KIF5B shRNA
KIF5B shRNA + KIF5B
KIF5B shRNA + KIF5A
Mushroom
Spine density per 10μm
0
2
4
6
****
****
****
***

B

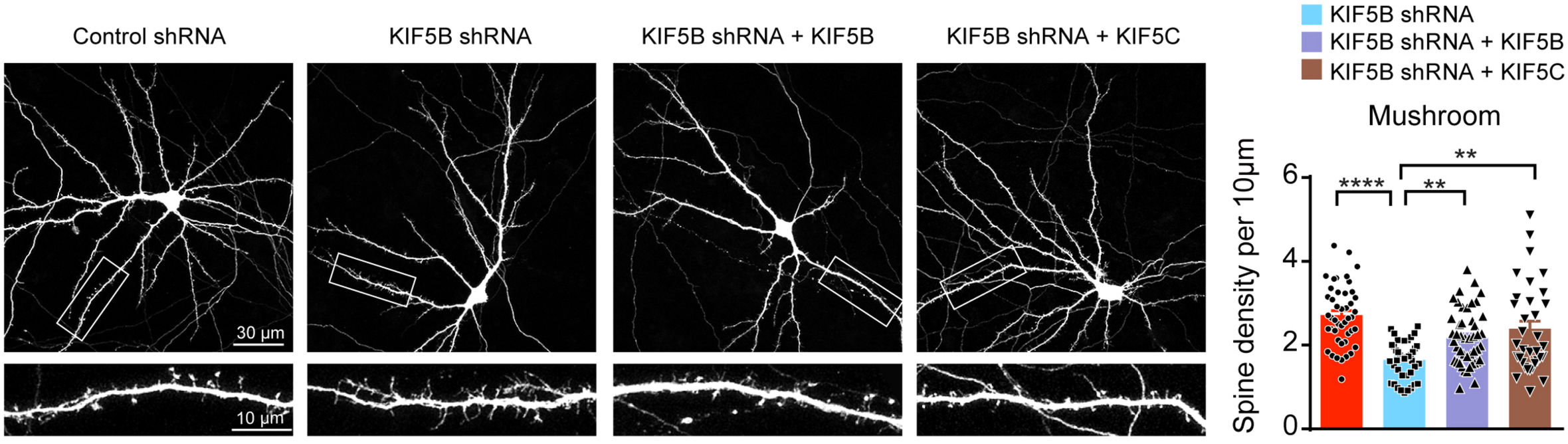
Control shRNA
KIF5B shRNA
KIF5B shRNA + KIF5B
KIF5B shRNA + KIF5C
30 μm
10 μm
Control shRNA
KIF5B shRNA
KIF5B shRNA + KIF5B
KIF5B shRNA + KIF5C
Mushroom
Spine density per 10μm
0
2
4
6
****
**
**

Figure 3

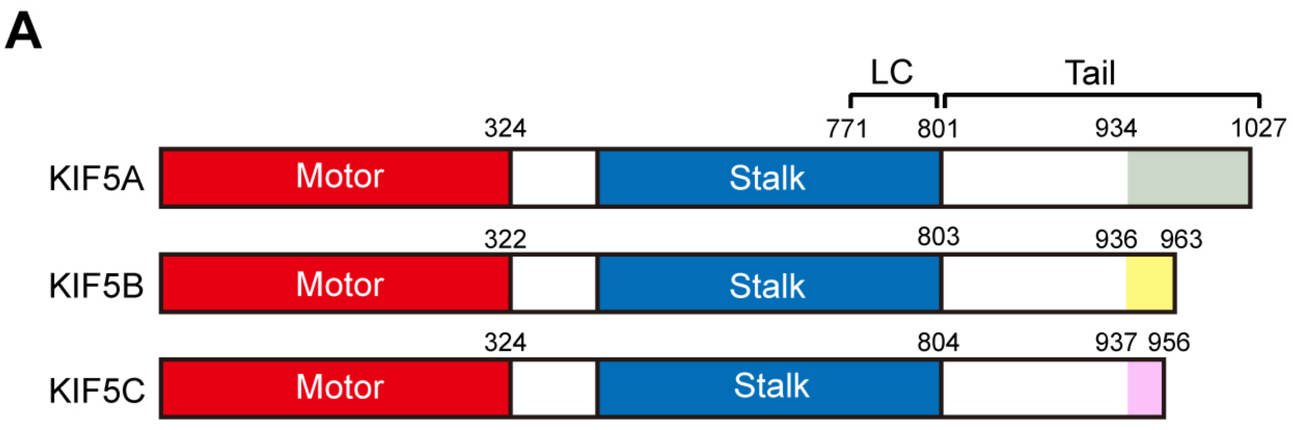
A
LC
Tail
324
771
801
934
1027
KIF5A
Motor
Stalk
322
803
936
963
KIF5B
Motor
Stalk
324
804
937
956
KIF5C
Motor
Stalk

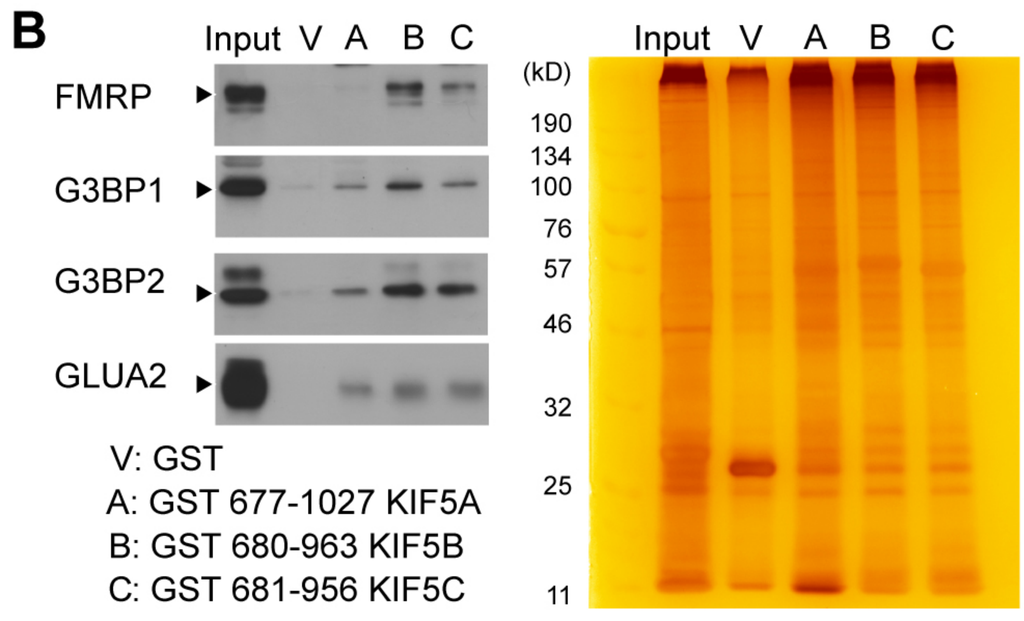
B
Input V A B C
FMRP
G3BP1
G3BP2
GLUA2
V: GST
A: GST 677-1027 KIF5A
B: GST 680-963 KIF5B
C: GST 681-956 KIF5C
Input V A B C
(kD)
190
134
100
76
57
46
32
25
11

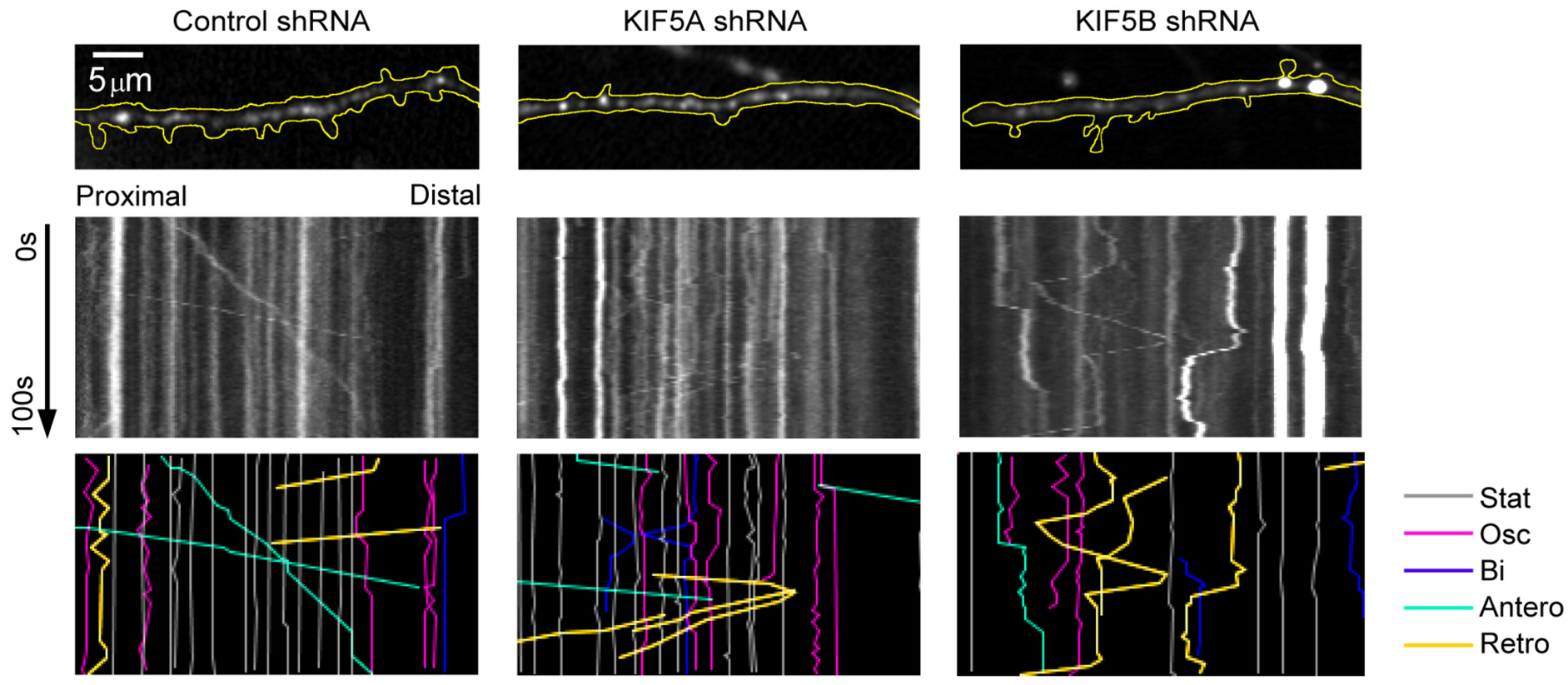
C
Control shRNA
KIF5A shRNA
KIF5B shRNA
5μm
Proximal
Distal
0s
100s
Stat
Osc
Bi
Antero
Retro
Control shRNA
KIF5A shRNA
KIF5B shRNA

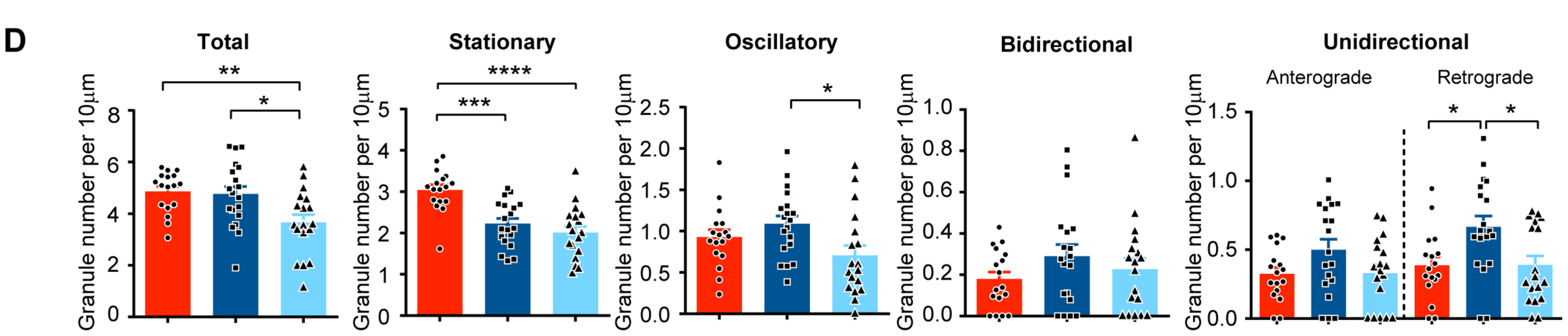
D
Total
Stationary
Oscillatory
Bidirectional
Unidirectional
Anterograde
Retrograde
Granule number per 10μm
**
*
****
***
*
*
*

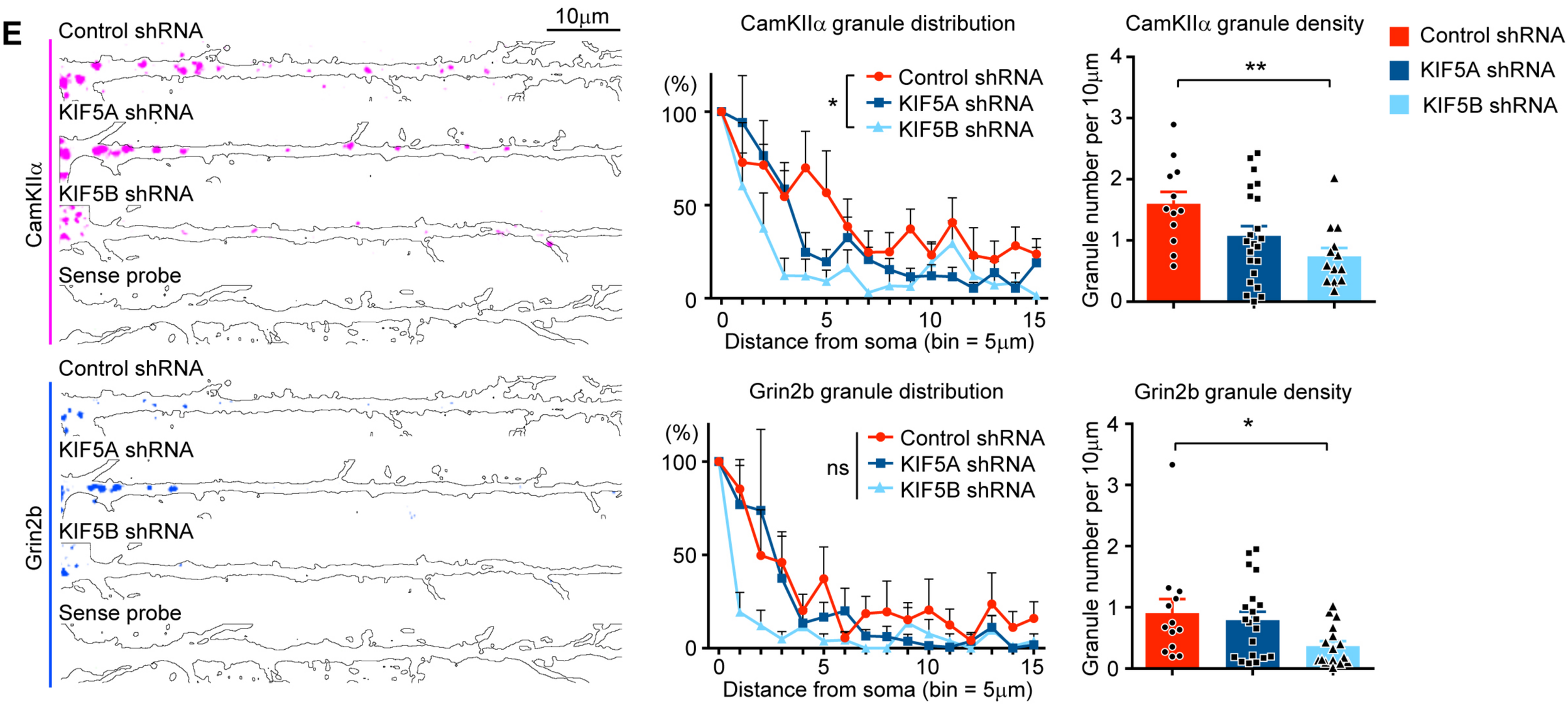
E
Control shRNA
KIF5A shRNA
KIF5B shRNA
Sense probe
CamKIIα
10μm
CamKIIα granule distribution
CamKIIα granule density
Grin2b granule distribution
Grin2b granule density
(%)
Distance from soma (bin = 5μm)
Granule number per 10μm
ns
Control shRNA
KIF5A shRNA
KIF5B shRNA

Figure 4

A

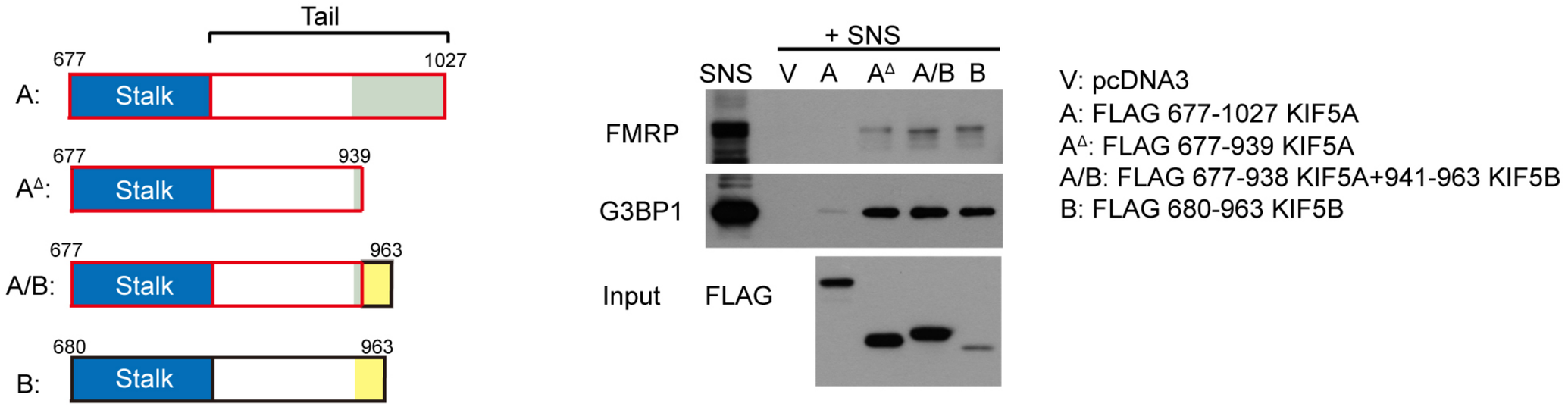
Tail
677
1027
A:
Stalk
677
939
A$^{\Delta}$:
Stalk
677
963
A/B:
Stalk
680
963
B:
Stalk
+ SNS
SNS V A A$^{\Delta}$ A/B B
FMRP
G3BP1
Input FLAG
V: pcDNA3
A: FLAG 677-1027 KIF5A
A$^{\Delta}$: FLAG 677-939 KIF5A
A/B: FLAG 677-938 KIF5A+941-963 KIF5B
B: FLAG 680-963 KIF5B

B

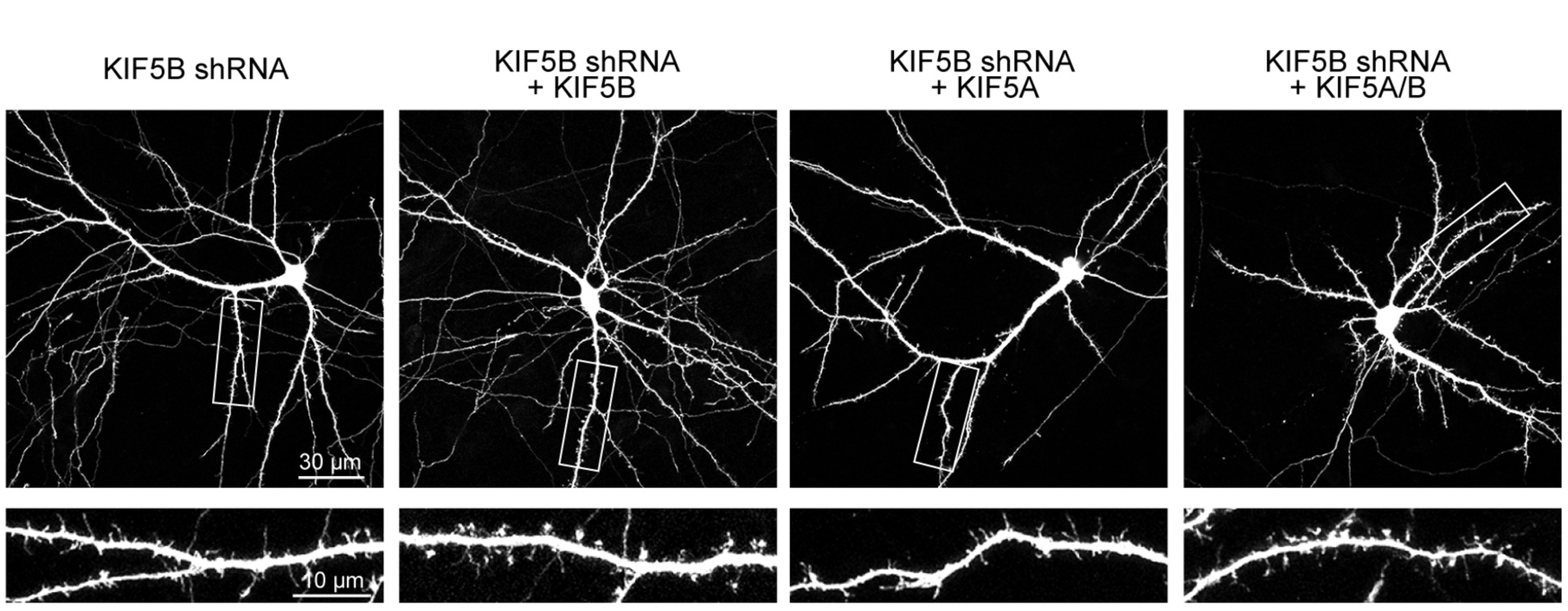
KIF5B shRNA
KIF5B shRNA + KIF5B
KIF5B shRNA + KIF5A
KIF5B shRNA + KIF5A/B
30 μm
10 μm

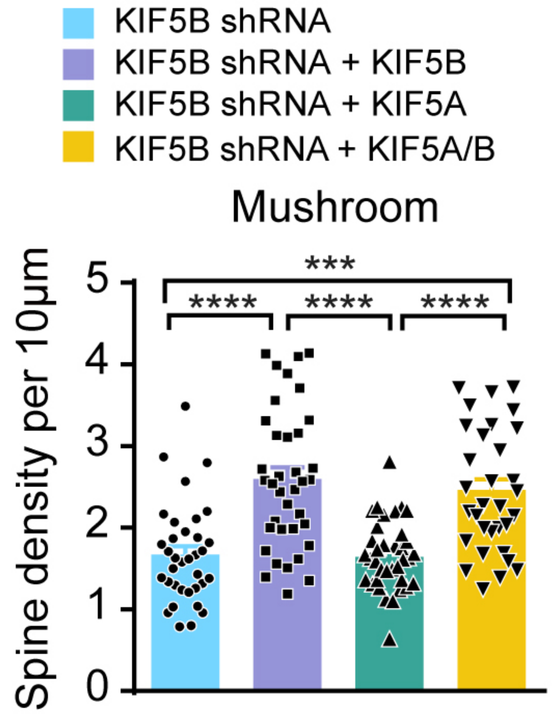
KIF5B shRNA
KIF5B shRNA + KIF5B
KIF5B shRNA + KIF5A
KIF5B shRNA + KIF5A/B
Mushroom
Spine density per 10μm
0
1
2
3
4
5
***
****
****
****

Figure 5

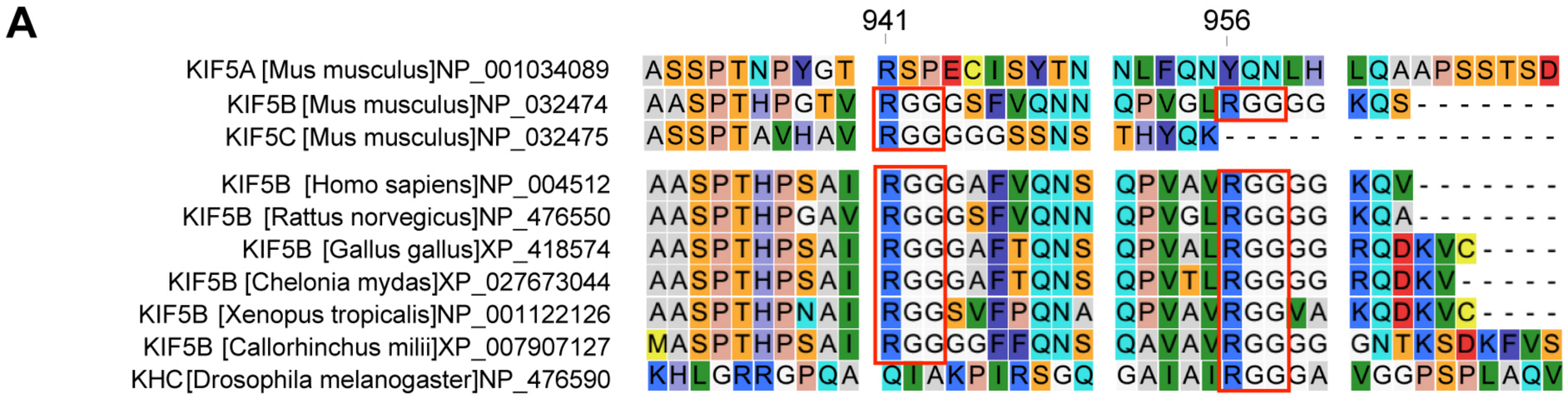
A
941
956
KIF5A [Mus musculus]NP_001034089
KIF5B [Mus musculus]NP_032474
KIF5C [Mus musculus]NP_032475
KIF5B [Homo sapiens]NP_004512
KIF5B [Rattus norvegicus]NP_476550
KIF5B [Gallus gallus]XP_418574
KIF5B [Chelonia mydas]XP_027673044
KIF5B [Xenopus tropicalis]NP_001122126
KIF5B [Callorhinchus milii]XP_007907127
KHC [Drosophila melanogaster]NP_476590

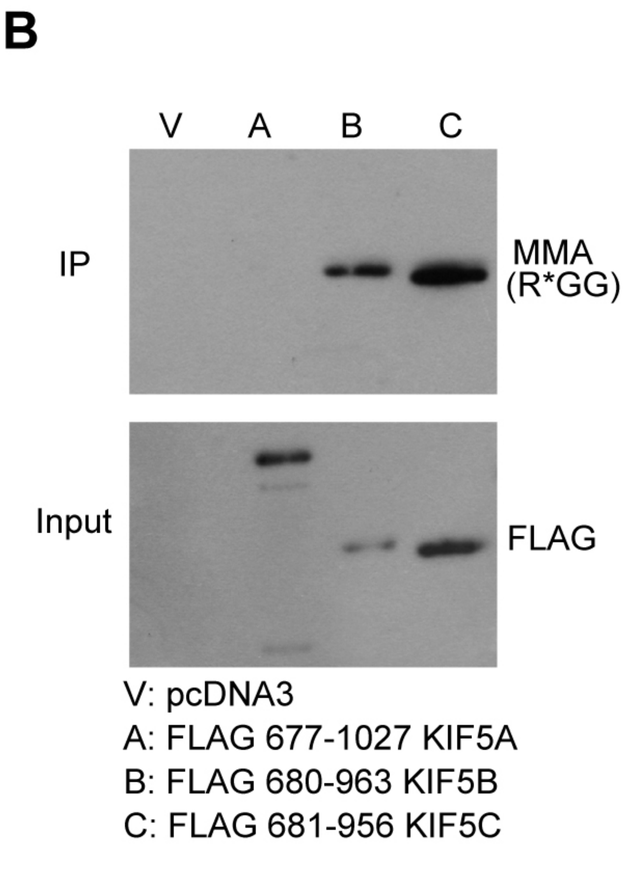
B
V A B C
IP
MMA (R*GG)
Input
FLAG
V: pcDNA3
A: FLAG 677-1027 KIF5A
B: FLAG 680-963 KIF5B
C: FLAG 681-956 KIF5C

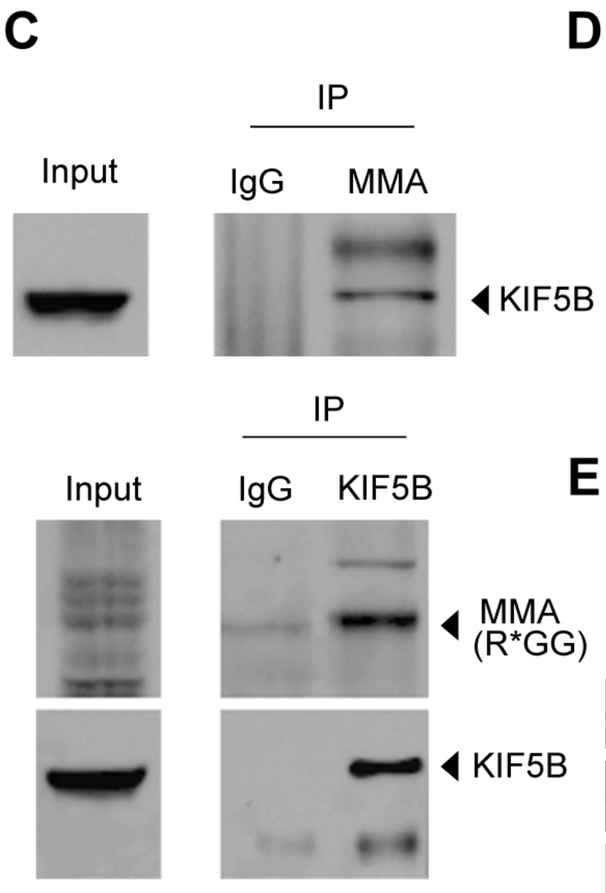
C
IP
Input
IgG
MMA
KIF5B
IP
Input
IgG
KIF5B
MMA (R*GG)
KIF5B

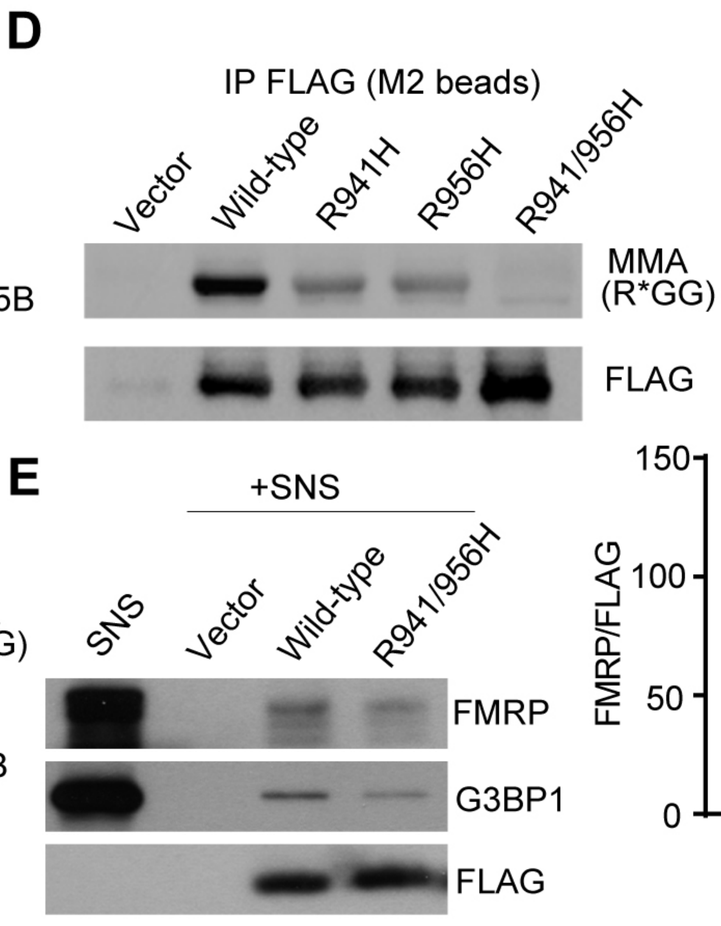
D
IP FLAG (M2 beads)
Vector
Wild-type
R941H
R956H
R941/956H
MMA (R*GG)
FLAG
E
+SNS
SNS
Vector
Wild-type
R941/956H
FMRP
G3BP1
FLAG

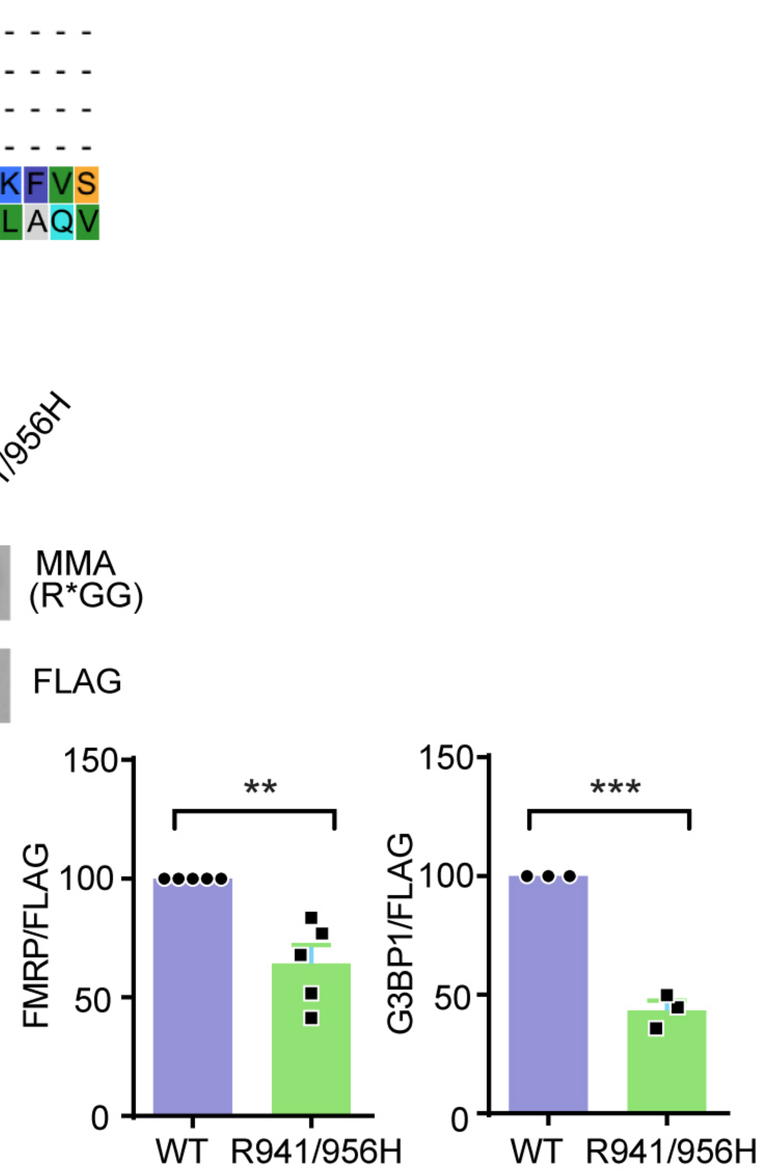
FMRP/FLAG
150
100
50
0
**
WT
R941/956H
G3BP1/FLAG
150
100
50
0
***
WT
R941/956H

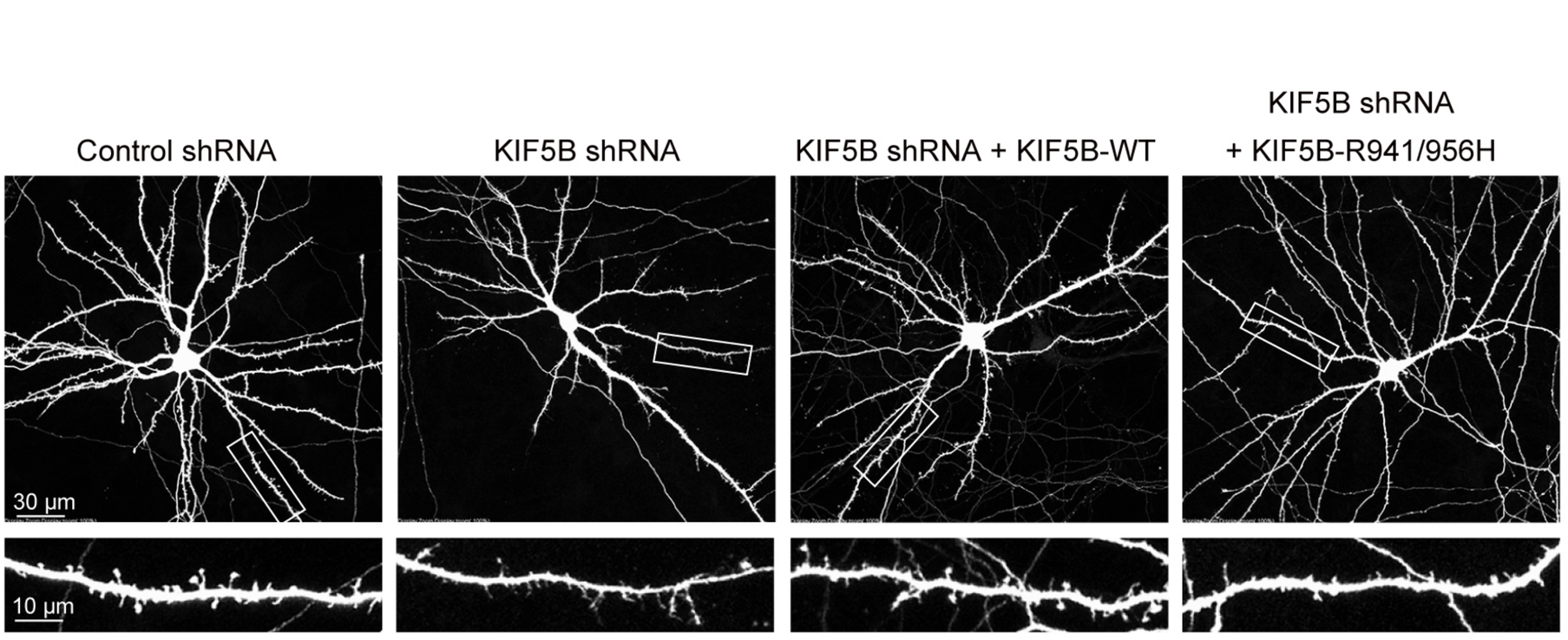
F
Control shRNA
KIF5B shRNA
KIF5B shRNA + KIF5B-WT
KIF5B shRNA + KIF5B-R941/956H
30 μm
10 μm

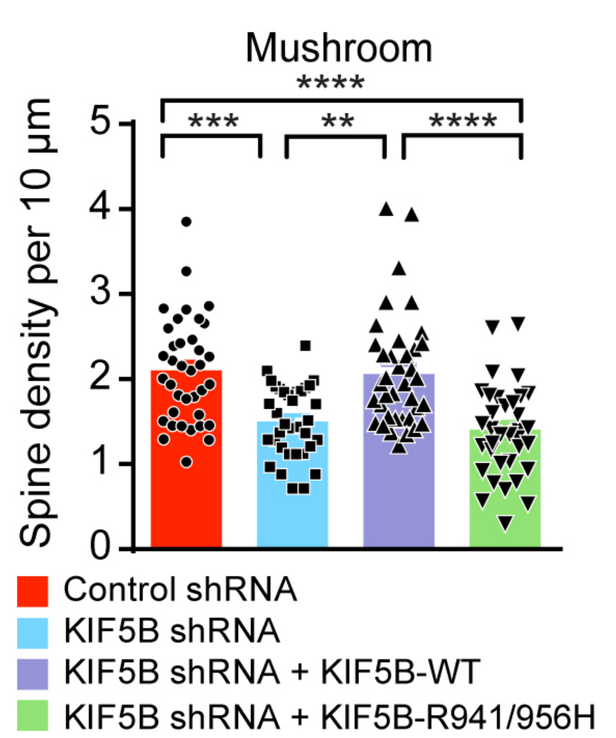
Mushroom
****
***
**
****
Spine density per 10 μm
5
4
3
2
1
0
Control shRNA
KIF5B shRNA
KIF5B shRNA + KIF5B-WT
KIF5B shRNA + KIF5B-R941/956H

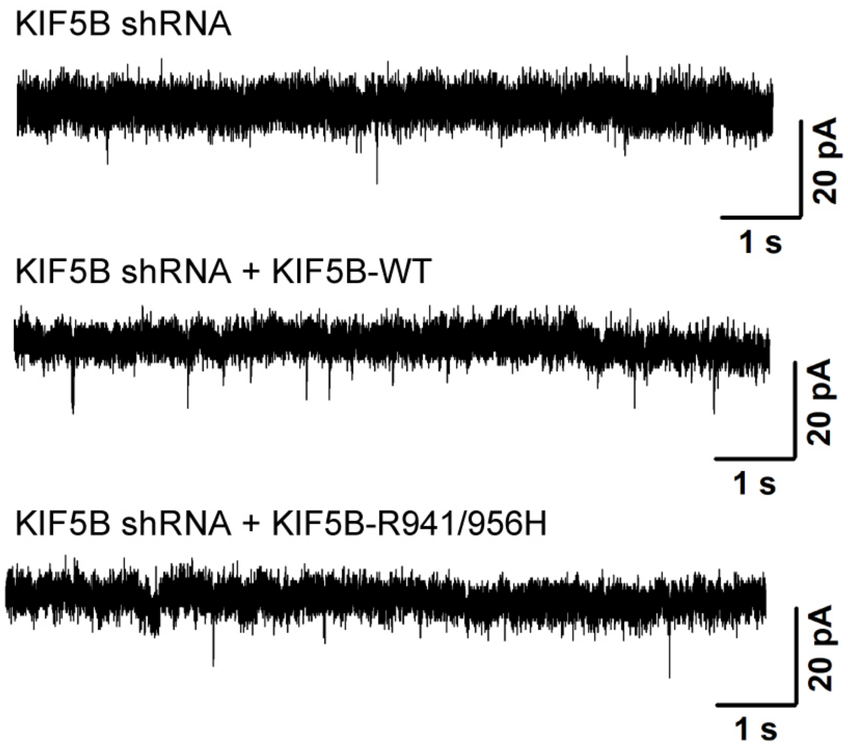
G
KIF5B shRNA
20 pA
1 s
KIF5B shRNA + KIF5B-WT
20 pA
1 s
KIF5B shRNA + KIF5B-R941/956H
20 pA
1 s

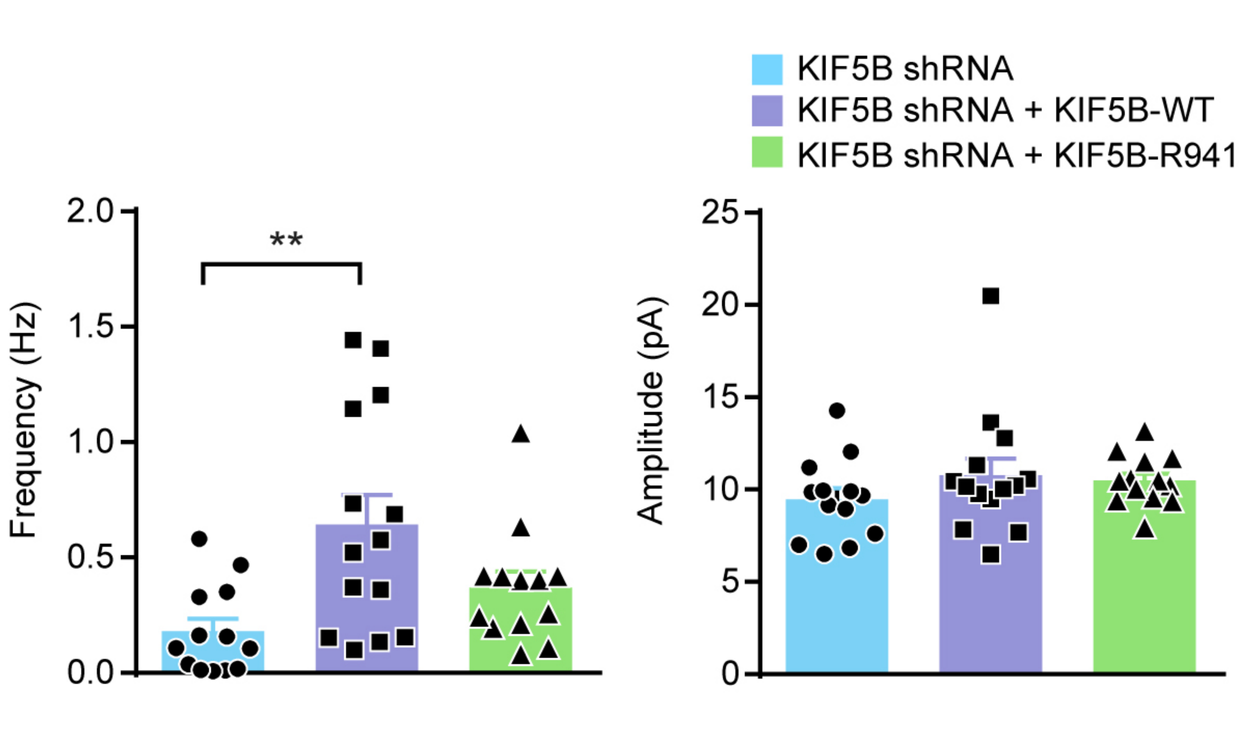
KIF5B shRNA
KIF5B shRNA + KIF5B-WT
KIF5B shRNA + KIF5B-R941/956H
Frequency (Hz)
2.0
1.5
1.0
0.5
0.0
**
Amplitude (pA)
25
20
15
10
5
0

Figure 6

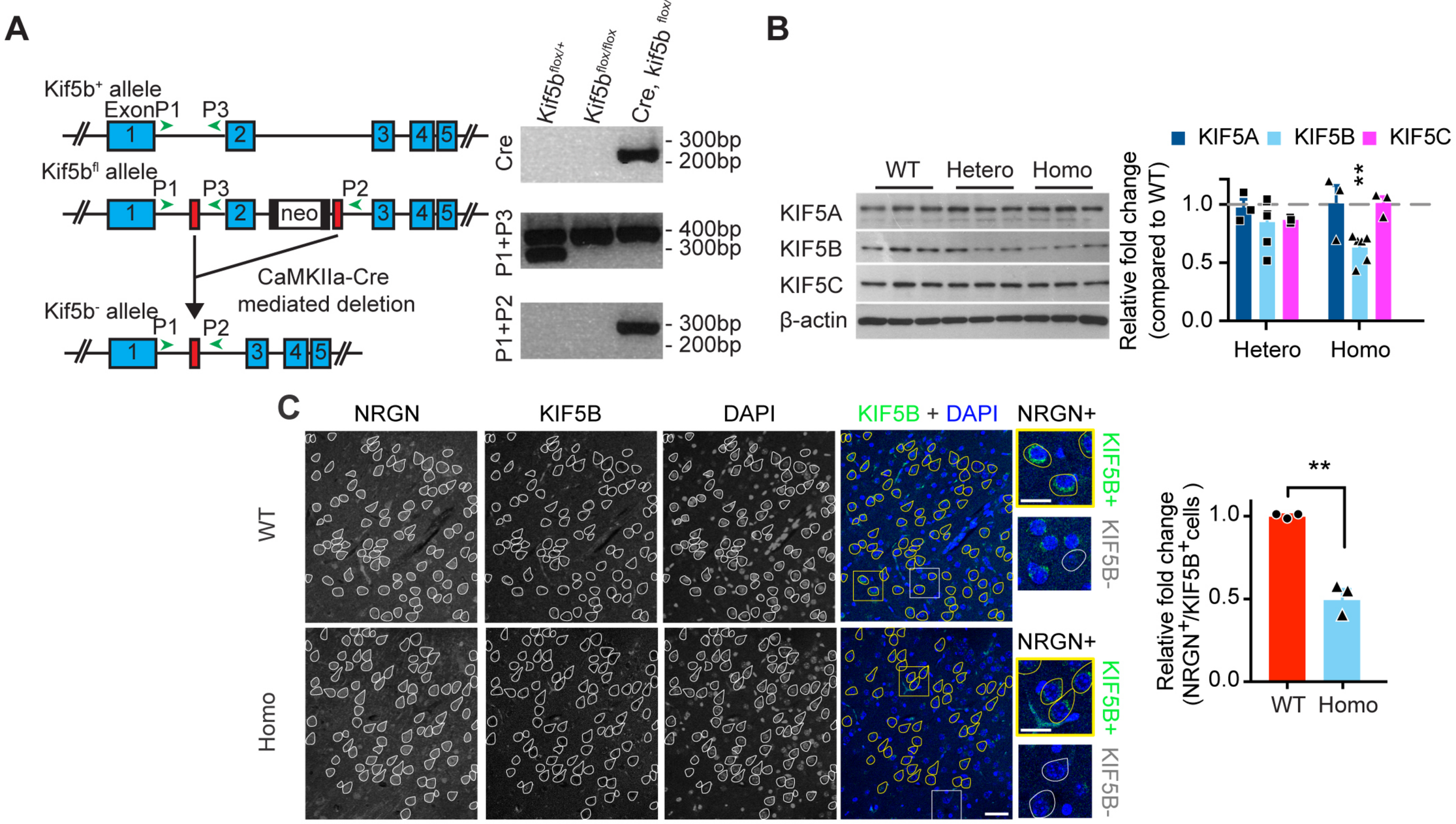
A
Kif5b+ allele
Exon
P1
P3
1
2
3
4
5
Kif5bfl allele
P1
P3
P2
neo
CaMKIIa-Cre
mediated deletion
Kif5b- allele
Kif5b flox/+
Kif5b flox/flox
Cre, kif5b flox/flox
Cre
P1+P3
P1+P2
300bp
200bp
400bp
300bp
B
WT
Hetero
Homo
KIF5A
KIF5B
KIF5C
β-actin
KIF5A
KIF5B
KIF5C
Relative fold change
(compared to WT)
1.0
0.5
0.0
**
Hetero
Homo
C
NRGN
KIF5B
DAPI
KIF5B + DAPI
NRGN+
KIF5B+
KIF5B-
WT
Homo
Relative fold change
(NRGN+/KIF5B+cells)
**
WT
Homo

Figure 7

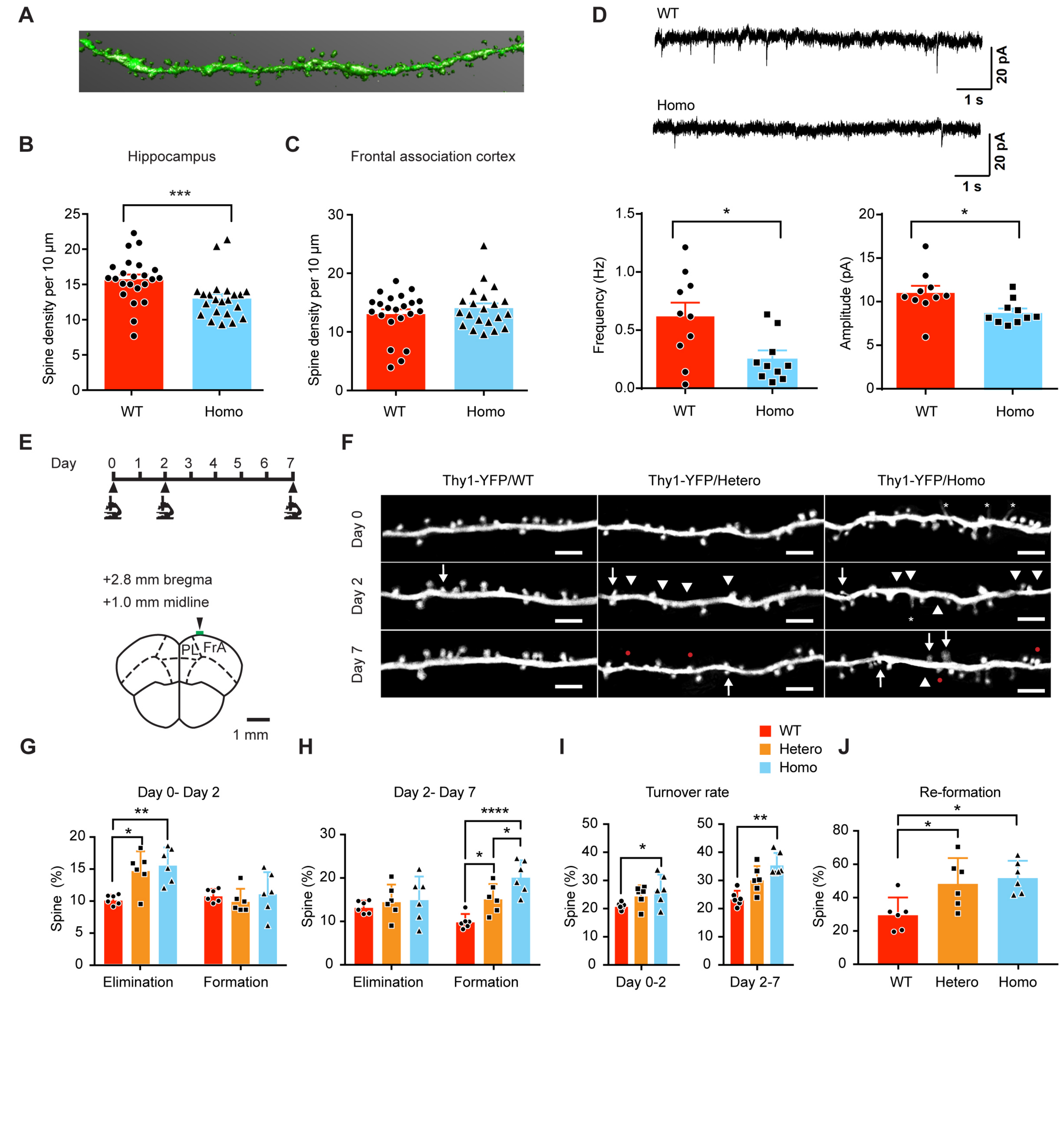
A
B
Hippocampus
***
Spine density per 10 µm
25
20
15
10
5
0
WT
Homo
C
Frontal association cortex
Spine density per 10 µm
30
20
10
0
WT
Homo
D
WT
20 pA
1 s
Homo
20 pA
1 s
*
Frequency (Hz)
1.5
1.0
0.5
0.0
WT
Homo
*
Amplitude (pA)
20
15
10
5
0
WT
Homo
E
Day
0 1 2 3 4 5 6 7
+2.8 mm bregma
+1.0 mm midline
PL
FrA
1 mm
F
Thy1-YFP/WT
Thy1-YFP/Hetero
Thy1-YFP/Homo
Day 0
Day 2
Day 7
G
Day 0- Day 2
**
*
Spine (%)
20
15
10
5
0
Elimination
Formation
H
Day 2- Day 7
****
*
*
Spine (%)
30
20
10
0
Elimination
Formation
I
WT
Hetero
Homo
Turnover rate
*
Spine (%)
50
40
30
20
10
0
Day 0-2
**
50
40
30
20
10
0
Day 2-7
J
Re-formation
*
*
Spine (%)
80
60
40
20
0
WT
Hetero
Homo

Figure 8

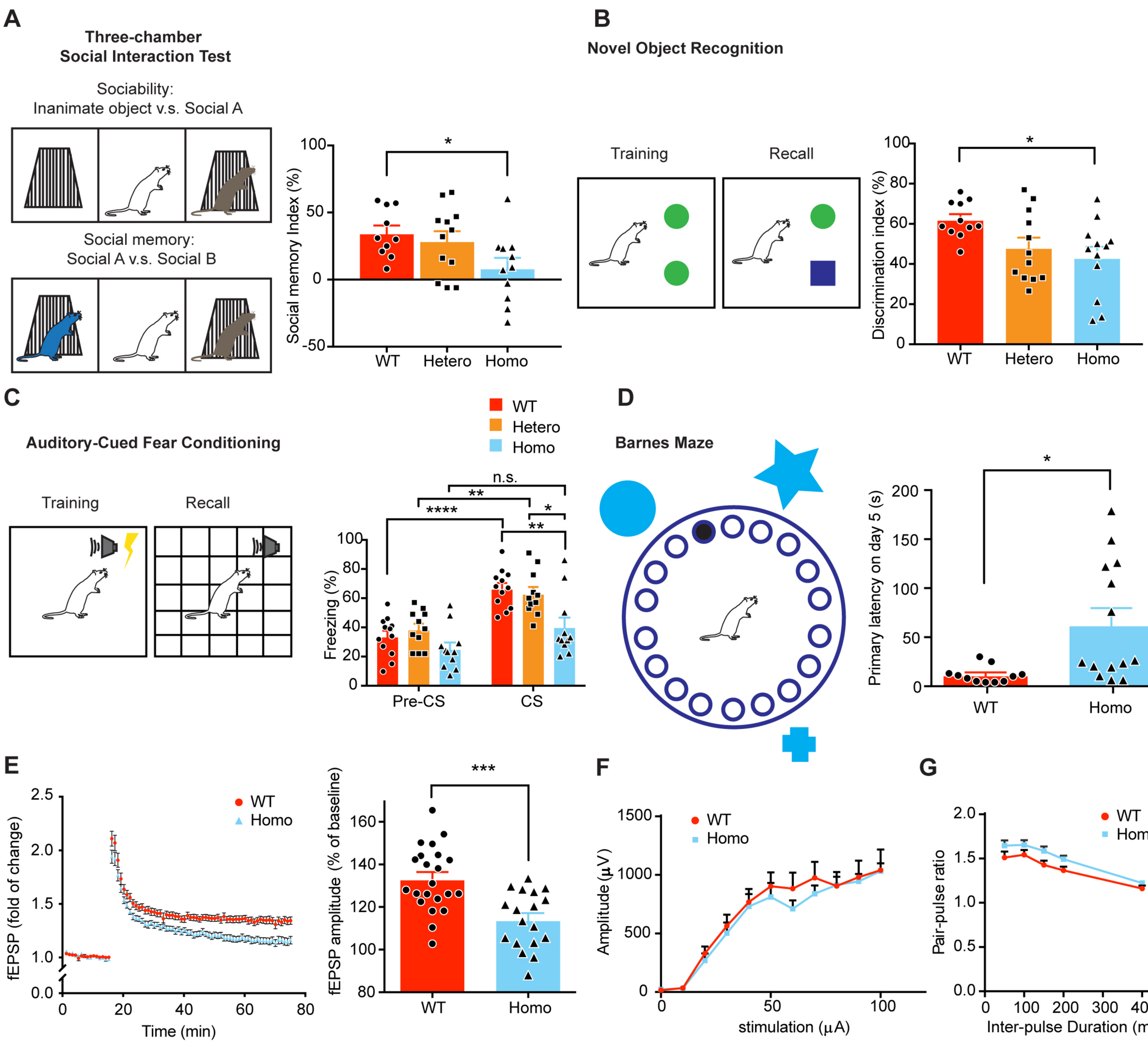
A
Three-chamber
Social Interaction Test
Sociability:
Inanimate object v.s. Social A
Social memory:
Social A v.s. Social B
Social memory Index (%)
100
50
0
-50
*
WT
Hetero
Homo
B
Novel Object Recognition
Training
Recall
Discrimination index (%)
100
80
60
40
20
0
*
WT
Hetero
Homo
C
Auditory-Cued Fear Conditioning
Training
Recall
WT
Hetero
Homo
Freezing (%)
100
80
60
40
20
0
n.s.
**
****
*
**
Pre-CS
CS
D
Barnes Maze
Primary latency on day 5 (s)
200
150
100
50
0
*
WT
Homo
E
fEPSP (fold of change)
2.5
2.0
1.5
1.0
0.0
WT
Homo
0
20
40
60
80
Time (min)
fEPSP amplitude (% of baseline)
160
140
120
100
80
***
WT
Homo
F
Amplitude (μV)
1500
1000
500
0
WT
Homo
0
50
100
stimulation (μA)
Pair-pulse ratio
2.0
1.5
1.0
0.5
0.0
WT
Homo
0
100
200
300
400
Inter-pulse Duration (ms)
G

A

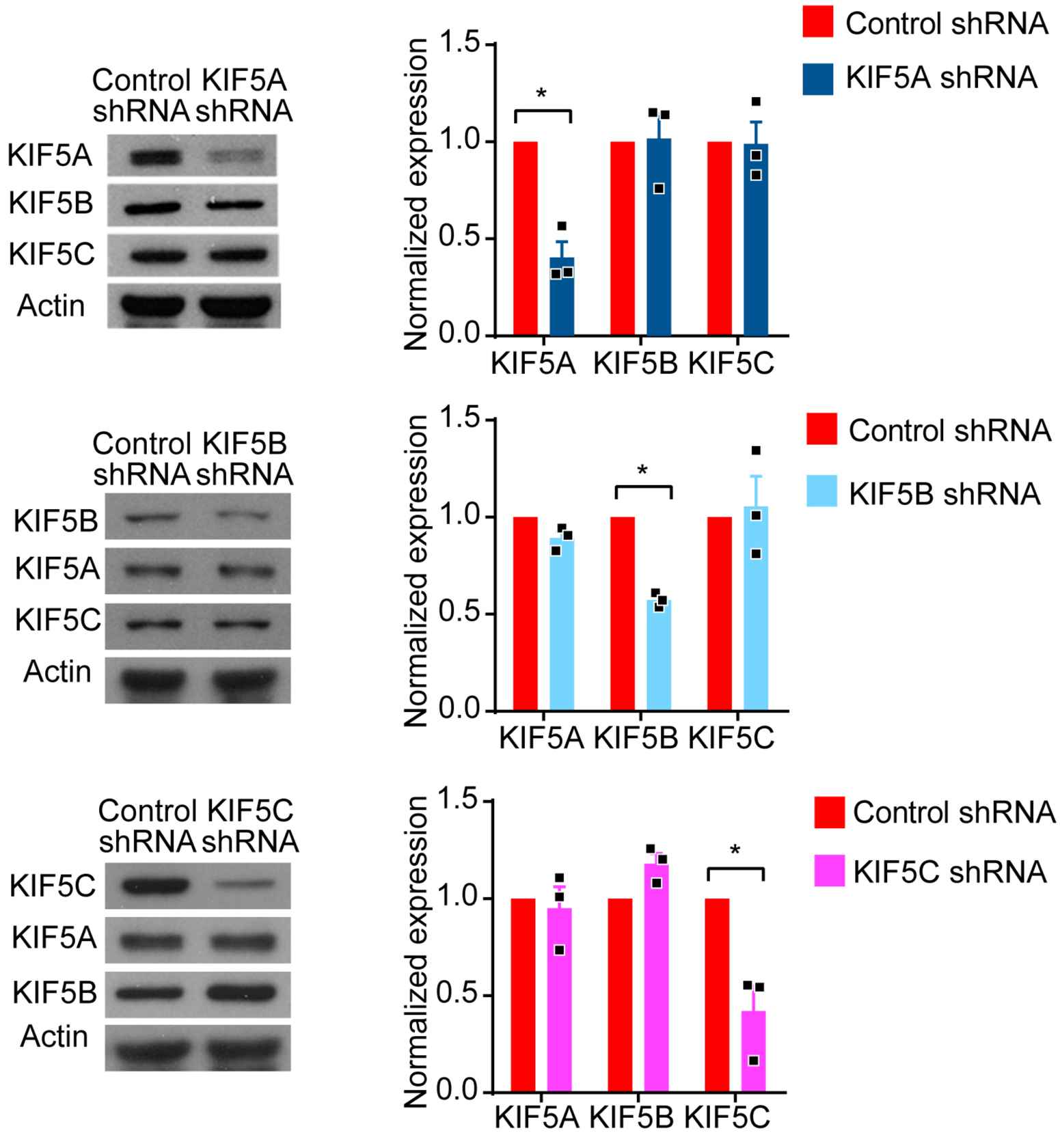

B

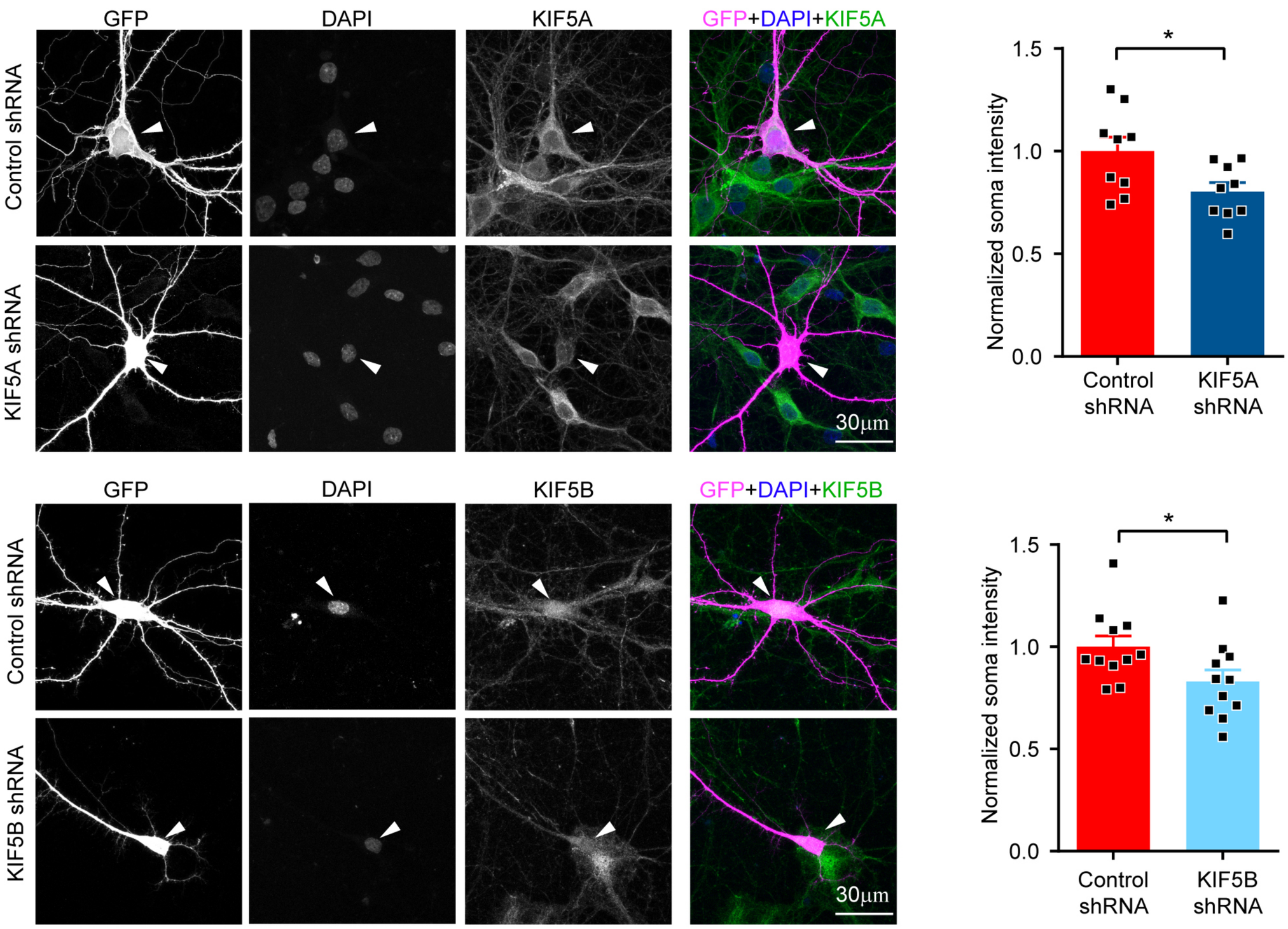

Figure 1-figure supplement 1. Validation of the knockdown efficiency and specificity of different shRNAs targeting each of the KIF5.

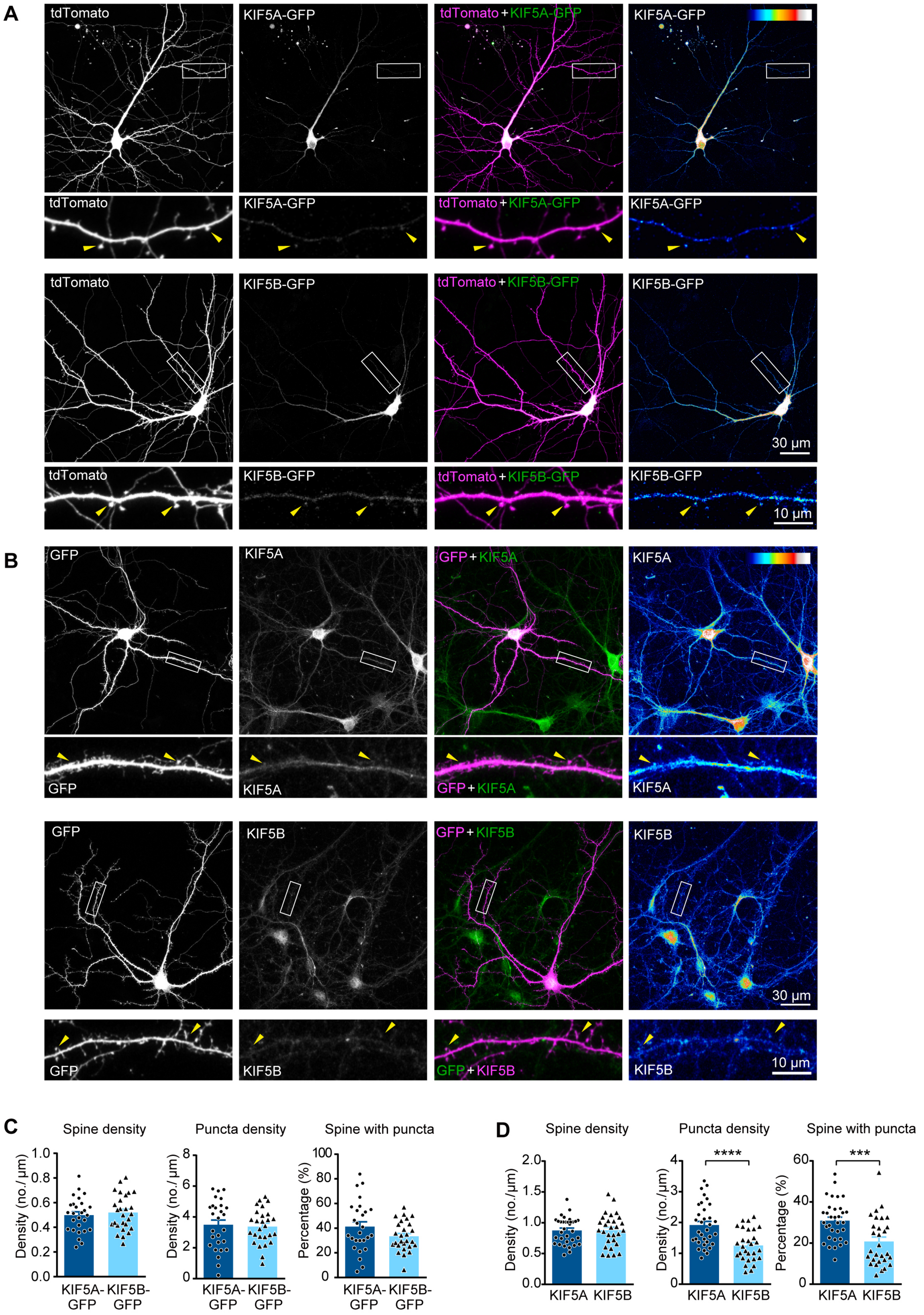

Figure 2-figure supplement 1. Localization of KIF5A and KIF5B in hippocampal neurons by GFP tagging or endogenous immunostaining.

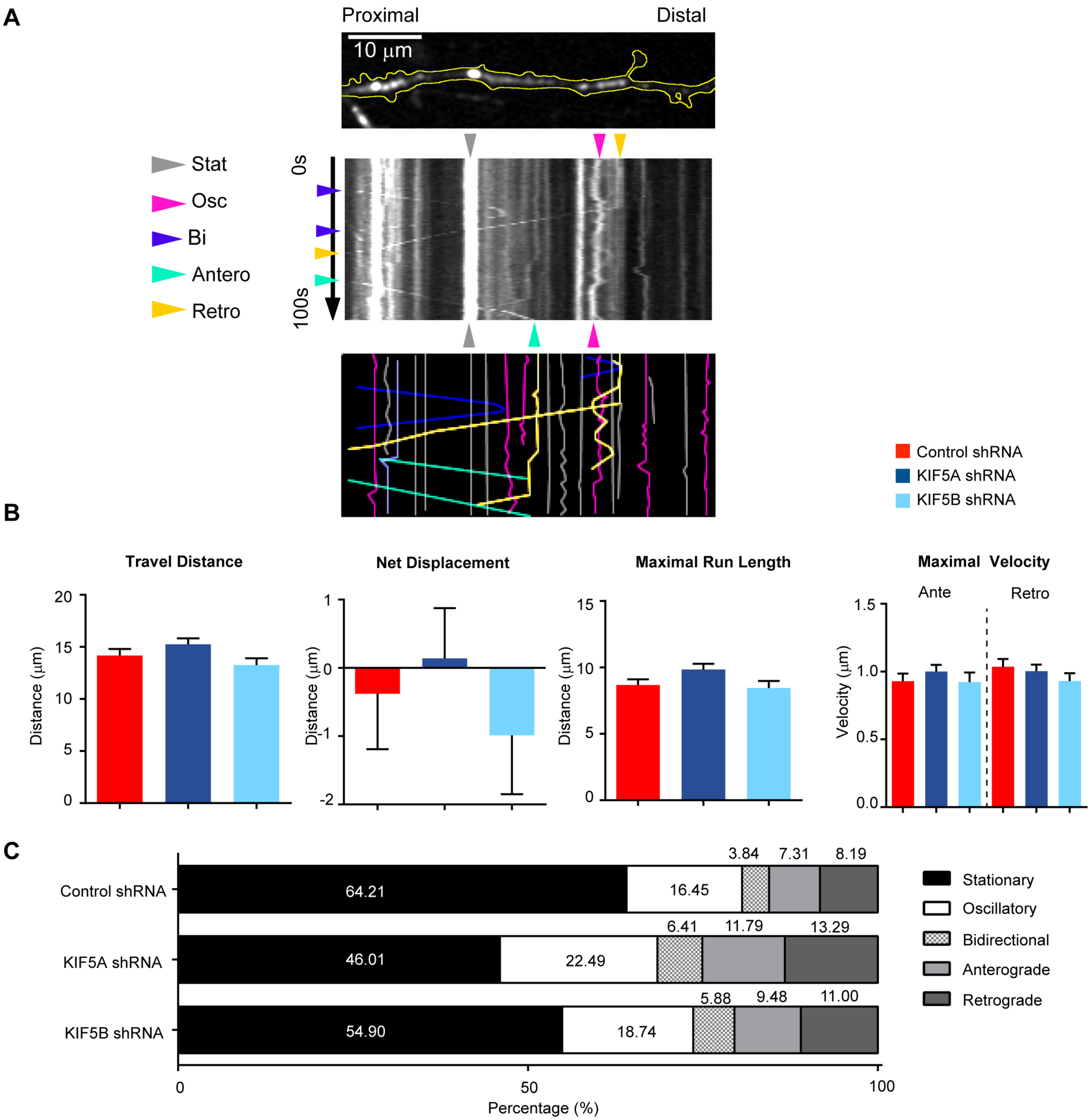

Figure 3-figure supplement 1. Quantification of GFP-FMRP granule motility and percentage of movements types after knockdown of KIF5A or KIF5B.

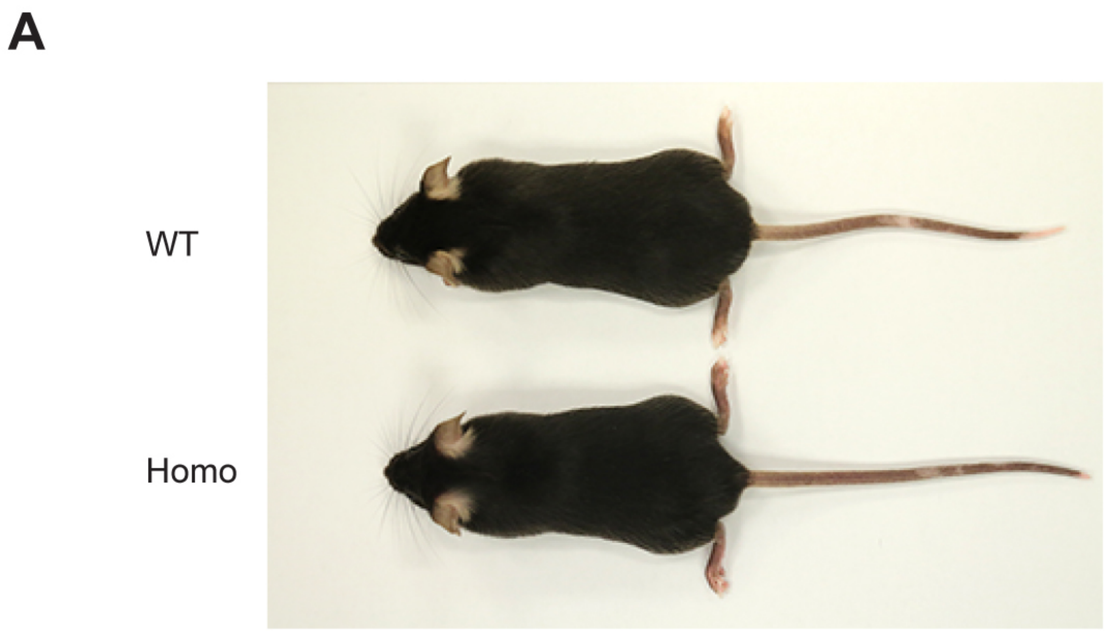

Figure 6-figure supplement 1. KIF5B conditional knockout mice showed normal general appearance and cortical layer architecture

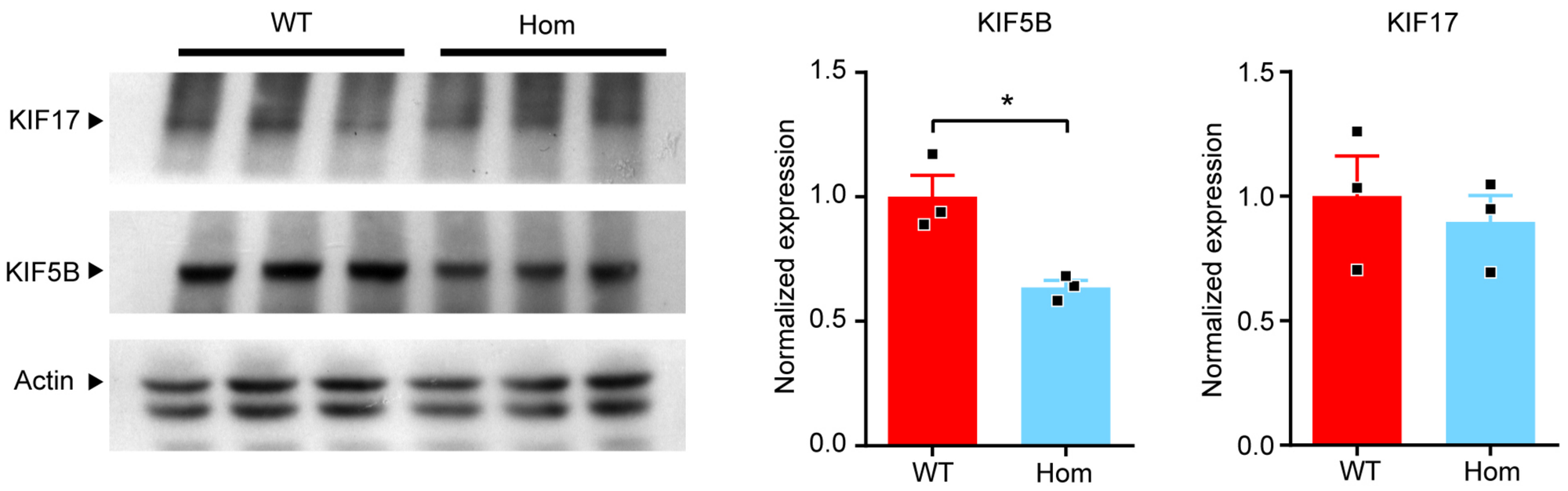

Figure 6-figure supplement 2. KIF5B conditional knockout mice showed no change in KIF17 expression.

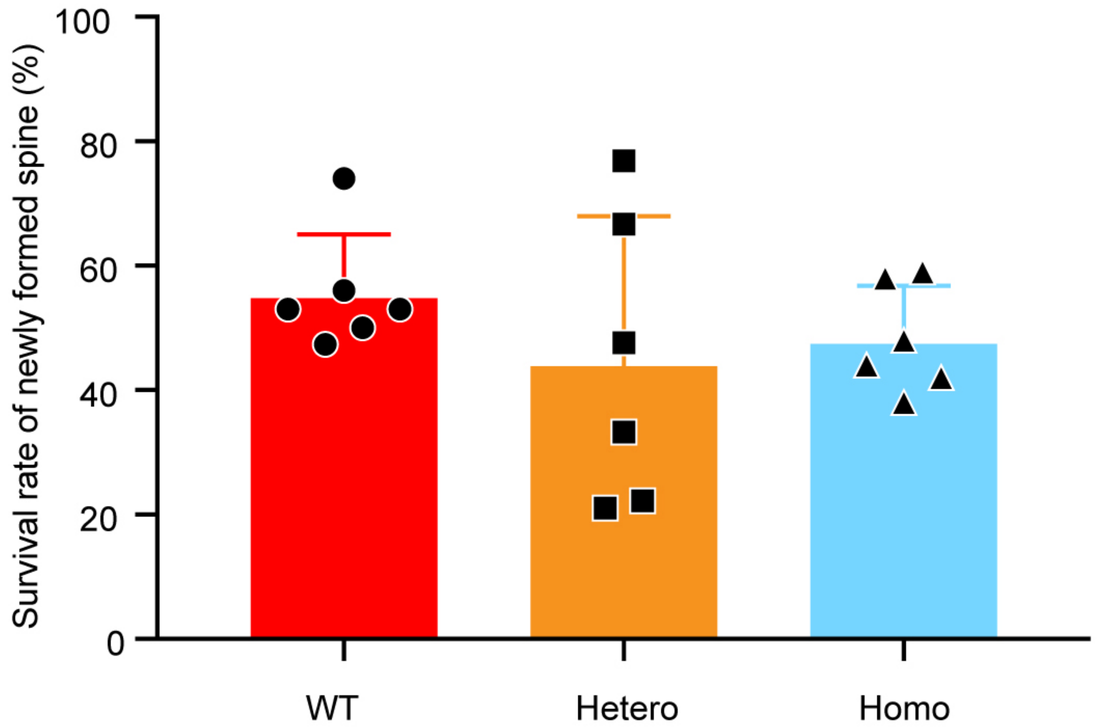

Figure 7-figure supplement 1. KIF5B conditional knockout mice show no significant difference in survival rate of newly formed dendritic spines.

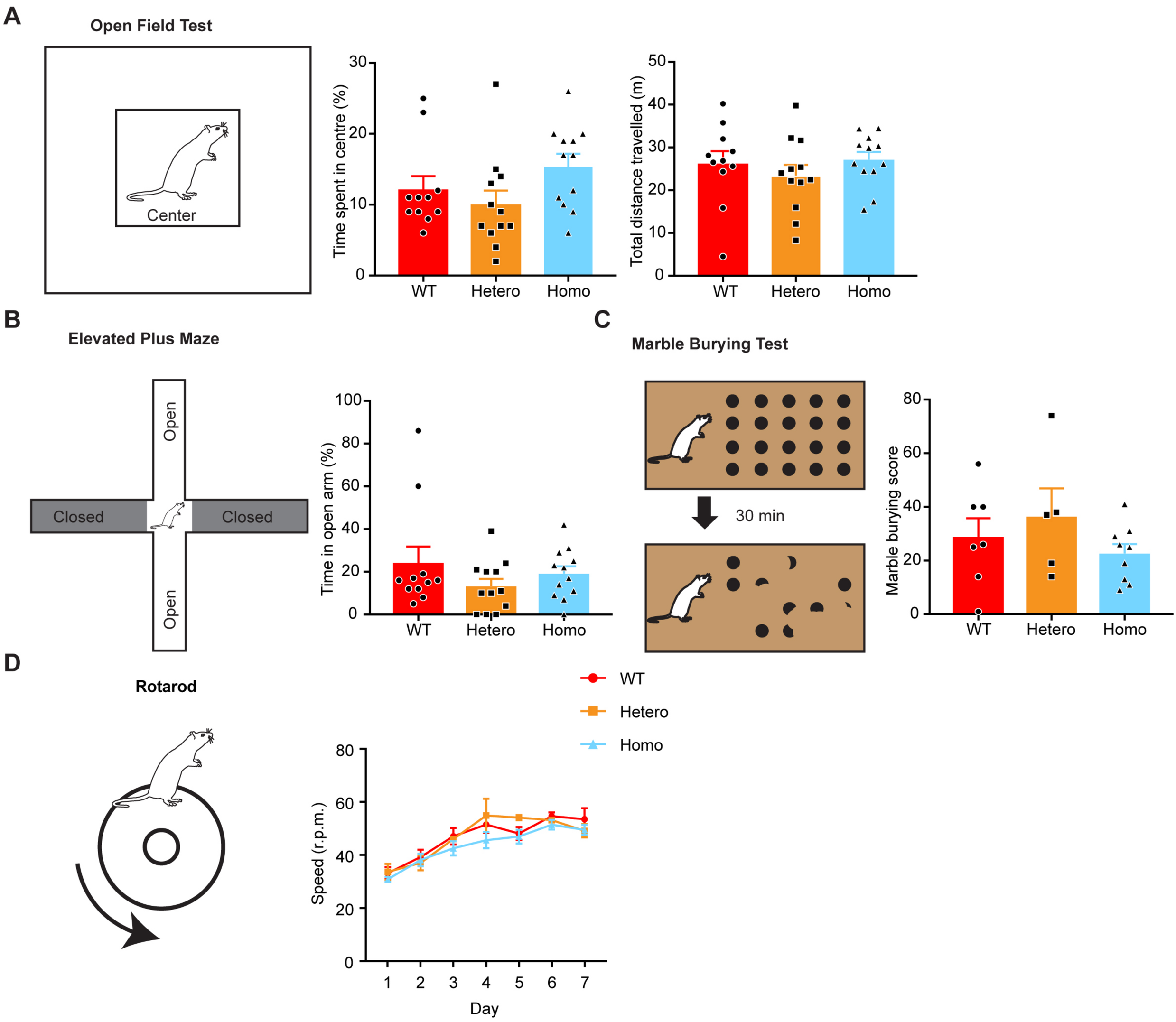

Figure 8-figure supplement 1. KIF5B conditional knockout mice showed no significant abnormalities in anxiety-related behavior tests.

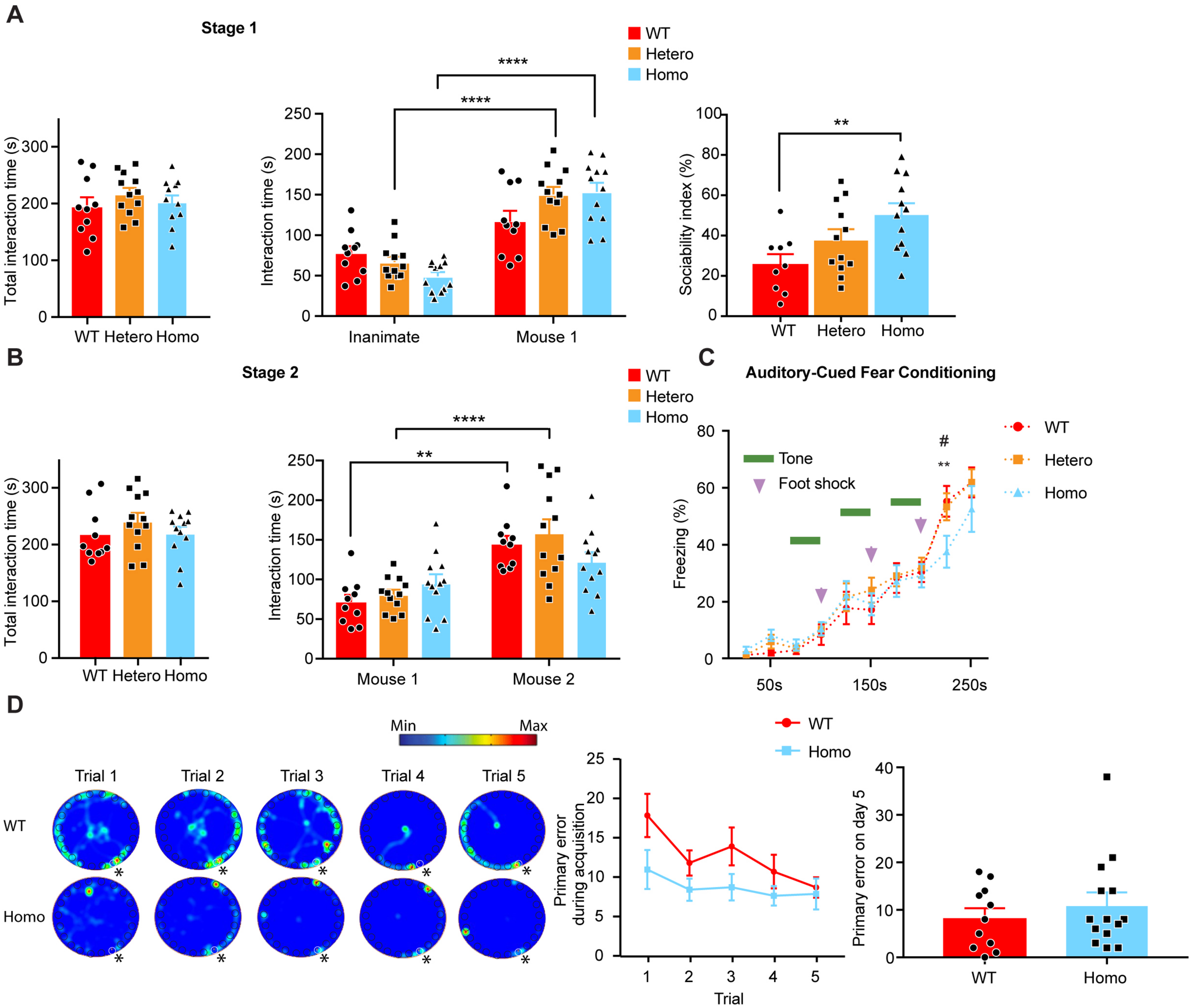

Figure 8-figure supplement 2. Sociability, fear acquisition, and primary error of Barnes maze in KIF5B conditional knockout mice.